

**THE UNIVERSITY OF CALGARY**

**Multicomponent Seismic Data Interpretation**

**by**

**Susan L.M. Miller**

**A THESIS  
SUBMITTED TO THE FACULTY OF GRADUATE STUDIES  
IN PARTIAL FULFILMENT OF THE REQUIREMENTS FOR THE  
DEGREE OF MASTER OF SCIENCE**

**DEPARTMENT OF GEOLOGY AND GEOPHYSICS**

**CALGARY, ALBERTA**

**DECEMBER 1996**

**© Susan L.M. Miller 1996**



National Library  
of Canada

Acquisitions and  
Bibliographic Services

395 Wellington Street  
Ottawa ON K1A 0N4  
Canada

Bibliothèque nationale  
du Canada

Acquisitions et  
services bibliographiques

395, rue Wellington  
Ottawa ON K1A 0N4  
Canada

*Your file Votre référence*

*Our file Notre référence*

**The author has granted a non-exclusive licence allowing the National Library of Canada to reproduce, loan, distribute or sell copies of his/her thesis by any means and in any form or format, making this thesis available to interested persons.**

**The author retains ownership of the copyright in his/her thesis. Neither the thesis nor substantial extracts from it may be printed or otherwise reproduced with the author's permission.**

**L'auteur a accordé une licence non exclusive permettant à la Bibliothèque nationale du Canada de reproduire, prêter, distribuer ou vendre des copies de sa thèse de quelque manière et sous quelque forme que ce soit pour mettre des exemplaires de cette thèse à la disposition des personnes intéressées.**

**L'auteur conserve la propriété du droit d'auteur qui protège sa thèse. Ni la thèse ni des extraits substantiels de celle-ci ne doivent être imprimés ou autrement reproduits sans son autorisation.**

0-612-20841-9

## Abstract

A procedure is developed for the coupled interpretation of multicomponent (*P-P* and *P-S*) seismic data, and is illustrated using two 3C-2D seismic datasets from Alberta, Canada. In both cases, numerical modelling studies were used to assist the interpretation. The principal objective of the Lousana survey was to differentiate reservoir dolomite from tight anhydrite within the Nisku Formation using seismic methods.  $V_p/V_s$  analysis of two intervals which contained the target mapped a decrease in  $V_p/V_s$  coincident with productive wells. The second survey, from the Blackfoot Field, targeted incised-valley sandstones in the Lower Cretaceous. The exploration goals were to seismically delineate the edges of an incised valley and to distinguish between sandstone and shale valley-fill sediments. The valley edges were defined by *P-P* and *P-S* seismic character changes. Within the incised valley, a decrease in  $V_p/V_s$  was interpreted to indicate sandstone sediments, while increasing  $V_p/V_s$  toward the northwest indicated increasing shaliness within the incised valley.

## **Acknowledgements**

Many people helped with the work presented in this thesis. I would like to thank my supervisor, Don Lawton, for his guidance, support, and good humour throughout the course of this work. The Lousana work was made possible by the generous donation of the seismic data by Unocal Canada Ltd. Andrea Bell, formerly of Norcen, provided background on the geology of the area. Dr. Mark Harrison processed the Lousana data and provided helpful insights. Dr. Robert Stewart and Mr. Ken Szata also contributed ideas and advice regarding the work on the Lousana Field. Many people at PanCanadian freely shared their knowledge about the geology and geophysics of the Blackfoot Field: Andre Politylo, Ian Shook, Bill Goodway, Dave Cooper, and Garth Syhlonyk. Many thanks to Dr. Gary Margrave and Ms. Evsen Aydemir for their assistance with the Blackfoot study and also for lots of laughs along the way. Kudos to Henry Bland and Darren Foltinek, who could always figure out a way to make the software and hardware work, and were also great companions. Thanks to all of the CREWES people, who enriched my university experience and provided great memories (and some really funny stories). Thanks also to the Sponsors of the CREWES Project for financial support and technical advice.

I am very grateful to my family for their unflagging support. My parents instilled in me the belief that I could accomplish whatever I set out to do, and provided emotional and financial support when it was needed. Finally, and most importantly, I would like to thank my son, Rhys, who never once complained about being alone or supperless on the many late nights and working weekends. Instead he offered cheerful support and encouragement, which made my task a great deal easier.

## Table of Contents

Approval page .....	ii
Abstract .....	iii
Acknowledgements .....	iv
Table of Contents .....	v
List of Tables .....	vi
List of Figures .....	vii
Glossary .....	ix
<b>Chapter 1 – Introduction</b> .....	<b>1</b>
1.1 Background .....	1
1.2 Thesis objectives, structure, and datasets used .....	4
1.3 Software and hardware used .....	5
<b>Chapter 2 – Lousana Case History</b> .....	<b>6</b>
2.1 Geology and Survey Objectives .....	6
2.2 Seismic survey acquisition and processing .....	10
2.2.1 Seismic survey acquisition .....	11
2.2.2 Seismic data processing .....	12
2.3 Seismic Interpretation .....	20
2.3.1 Correlation of <i>P-P</i> and <i>P-S</i> seismic sections .....	20
2.3.2 <i>V<sub>p</sub>/V<sub>s</sub></i> extraction at the well location .....	24
2.3.3 Horizon interpretation .....	26
2.4 Numerical seismic modelling .....	31
2.4.1 Forward <i>P-P</i> and <i>P-S</i> Modelling .....	31
2.4.2 Models with multiples and local conversions .....	38
2.4.2.1. <i>P-P</i> models with multiples and local conversions .....	38
2.4.2.2 Comparison of models from 16-19 and 12-20 wells .....	41
2.4.2.3 <i>P-S</i> models with multiples .....	42
2.5 Discussion .....	44
<b>Chapter 3 – Blackfoot Case History</b> .....	<b>46</b>
3.1 Geology of the Blackfoot Field .....	46
3.2 Objectives .....	48
3.3 Seismic data acquisition .....	49
3.4 Data processing .....	51
3.5 Correlation of <i>P-P</i> and <i>P-S</i> seismic data .....	57
3.6 Numerical seismic modelling .....	60
3.6.1 Seismic cross-section models .....	61
3.6.2 <i>V<sub>p</sub>/V<sub>s</sub></i> analysis of the seismic model .....	64
3.7 Seismic interpretation .....	65
3.7.1 <i>P-P</i> and <i>P-S</i> seismic data interpretation .....	66
3.7.2 <i>V<sub>p</sub>/V<sub>s</sub></i> analysis of the seismic data .....	70
3.8 Well log analysis .....	71
3.9 Channel interpretation and discussion .....	73
<b>Chapter 4 – Discussion and Conclusions</b> .....	<b>75</b>
4.1 Discussion .....	75
4.2 Conclusions .....	76
4.2.1 Lousana Field .....	77
4.2.2 Blackfoot Field .....	78
<b>References</b> .....	<b>79</b>

## **List of Tables**

<b>Table 2.1</b>	<b>Field acquisition and recording parameters for the Lousana survey.....</b>	<b>11</b>
<b>Table 2.2</b>	<b>Rock property values used for numerical models.....</b>	<b>32</b>
<b>Table 3.1</b>	<b>Field acquisition and recording parameters for the Blackfoot survey .....</b>	<b>50</b>

## List of Figures

FIG. 1.1	Location map showing the Lousana Field and Blackfoot.....	5
FIG. 2.1	Simplified stratigraphic nomenclature for Lousana.....	7
FIG. 2.2	Shotpoint map of the Lousana survey.....	8
FIG. 2.3	Cross-section A-A' using sonic logs.....	10
FIG. 2.4	(a) Vertical-component shot record and (b) radial-component shot record.....	12
FIG. 2.5	Processing flow for the vertical-component ( <i>P-P</i> ) seismic data.....	13
FIG. 2.6	Migrated <i>P-P</i> stacked section for Line EKW-001.....	14
FIG. 2.7	Migrated <i>P-P</i> stacked section for Line EKW-002.....	15
FIG. 2.8	Processing flow for the radial-component ( <i>P-S</i> ) seismic data.....	17
FIG. 2.9	Migrated <i>P-S</i> stacked section for Line EKW-001.....	18
FIG. 2.10	Migrated <i>P-S</i> stacked section for Line EKW-002.....	19
FIG. 2.11	Comparison of (a) EKW-001 and (b) EKW-002 for the vertical component.....	20
FIG. 2.12	Comparison of (a) EKW-001 and (b) EKW-002 for the radial component.....	21
FIG. 2.13	Correlation of <i>P-P</i> synthetic seismogram with the <i>P-P</i> seismic data.....	22
FIG. 2.14	Correlation of <i>P-S</i> synthetic seismogram with the <i>P-S</i> seismic data.....	24
FIG. 2.15	<i>P-S</i> offset synthetic stacks generated from constant $V_p/V_s$ values.....	25
FIG. 2.16	<i>P-S</i> synthetic stacks from the 16-19 and 12-20 with interval $V_p/V_s$ .....	26
FIG. 2.17	Interpretation of <i>P-P</i> and <i>P-S</i> seismic for portion of Line EKW-002.....	27
FIG. 2.18	$V_p/V_s$ values on Line EKW-002 for two intervals.....	28
FIG. 2.19	$V_p/V_s$ values for two intervals which bracket the Nisku reservoir.....	29
FIG. 2.20	$V_p/V_s$ values along Line EKW-001.....	30
FIG. 2.21	Well log curves used to model <i>P-P</i> and <i>P-S</i> response of basin.....	32
FIG. 2.22	Well log curves used to model <i>P-P</i> and <i>P-S</i> response of the buildup.....	33
FIG. 2.23	<i>P-P</i> model results.....	34
FIG. 2.24	<i>P-S</i> model results.....	35
FIG. 2.25	Plot of $V_p/V_s$ measured across intervals on the model data.....	36
FIG. 2.26	<i>P-P</i> offset models for (a) primaries only (b) primaries and multiples (c) primaries and conversions (d) primaries, multiples, and conversions.....	39
FIG. 2.27	The <i>P-P</i> offset synthetic stack with all intrabed multiples and conversions.....	41
FIG. 2.28	(a) The 16-19 stacked synthetic seismogram (b) The 12-20 stacked synthetic seismogram.....	42
FIG. 2.29	(a) The <i>P-S</i> seismic data is tied to (b) the <i>P-S</i> offset synthetic stack, with primaries only.....	43
FIG. 2.30	(a) The <i>P-S</i> seismic data is tied to (b) the <i>P-S</i> offset synthetic stack, with primaries and all intrabed multiples.....	43
FIG. 3.1	Stratigraphic sequence near the zone of interest.....	47
FIG. 3.2	Location map of 3C-2D seismic line 950278.....	49
FIG. 3.3	Examples of (a) vertical- and (b) radial-component shot records.....	51
FIG. 3.4	Processing flow for vertical-component seismic data.....	52
FIG. 3.5	<i>P-P</i> migrated stacked seismic section of line 950278.....	53
FIG. 3.6	Processing flow for radial-component seismic data.....	55
FIG. 3.7	<i>P-S</i> migrated stacked seismic section of line 950278.....	56
FIG. 3.8	Blow-up of the migrated <i>P-P</i> section in the zone of interest.....	58
FIG. 3.9	Blow-up of the migrated <i>P-S</i> section in the zone of interest.....	59
FIG. 3.10	Correlation of (a) <i>P-P</i> and (b) <i>P-S</i> offset synthetic seismograms.....	59
FIG. 3.11	Comparison of (a) <i>P-P</i> and (b) <i>P-S</i> seismic sections.....	60
FIG. 3.12	Well log sections using (a) <i>P</i> - sonic logs and (b) <i>S</i> -sonic logs.....	62
FIG. 3.13	<i>P-P</i> synthetic seismogram section.....	63
FIG. 3.14	<i>P-S</i> synthetic seismogram section.....	64
FIG. 3.15	$V_p/V_s$ values from the cross-section model.....	65

FIG. 3.16 Interpretation of the <i>P-P</i> seismic data.....	67
FIG. 3.17 Interpretation of the <i>P-S</i> seismic data.....	69
FIG. 3.18 <i>P-P</i> and <i>P-S</i> isochrons for the Viking to Shunda interval.....	70
FIG. 3.19 $V_p/V_s$ values calculated for the Viking to Shunda interval.....	71
FIG. 3.20 $V_p/V_s$ versus gamma values in the Glauconitic Formation.....	72
FIG. 3.21 $V_s$ versus $V_p$ in the Glauconitic Formation.....	73



## Glossary of Scientific Terms

**3-C seismic:** A seismic survey which uses a conventional energy source and is recorded on 3-C geophones.

**3-C Geophone:** Seismic recording device with three orthogonal (or trigonal Galperin) coils which respond to ground motion in three orthogonal directions.

**3C-2D seismic survey:** Two-dimensional seismic survey recorded on 3-C geophones.

**Bandpass filter:** A filter which allows the passage of certain frequency components and attenuates others.

**Dipole sonic log:** Sonic logging tool which uses a dipole source to deform the borehole and subsequently records *P*- and *S*- wave transit times.

**Groundroll:** Surface wave which propagates by retrograde elliptical particle motion. Characterized by high amplitude, low frequency, and low velocity.

**Isochron:** The time interval between two interpreted seismic horizons.

**Mode:** Refers to type of wave propagation, e.g. compressional mode or shear mode.

**Multicomponent seismic:** Seismic data acquired with more than one source and/or receiver mode; in this thesis, refers to a conventional source and 3-C recording.

***P* wave:** Pressure, compressional, or longitudinal elastic body wave; direction of propagation is parallel to particle motion.

***P-P* seismic:** Seismic waves travelling down as *P* waves, reflecting from an interface, and travelling up as *P* waves. In this thesis, waves recorded on the vertical component of the geophone are assumed to be largely *P-P* mode.

***P-S* seismic:** Seismic waves travelling down as *P* waves, reflecting and converting at an interface, and travelling up as *S* waves. In this thesis, waves recorded on the radial component of the geophone are assumed to be largely *P-S* mode.

**Radial component:** Horizontal geophone coil which responds to horizontal ground motion in line with the source-receiver azimuth.

**SP:** Shot point, i.e. station number for seismic source location.

**Statics:** Time-shift correction applied to seismic data to compensate for the velocity effect of near-surface stratigraphy by adjusting the traces to a common datum.

**S wave:** Shear elastic body wave; direction of propagation is perpendicular to particle motion.

**Synthetic seismogram:** An artificial seismic record made by, in the zero-offset case, convolving a wavelet with a reflectivity series. In the offset case, a layered model is ray-traced using a chosen geometry and an artificial shot gather is computed, which can also be stacked.

**Transverse component:** Horizontal geophone coil which responds to horizontal ground motion orthogonal to the source-receiver azimuth.

**Vertical component:** Vertical geophone coil which responds to vertical ground motion.

**$V_p$ :** *P*-wave velocity

**$V_p/V_s$ :** Ratio of *P*-wave velocity to *S*-wave velocity

**$V_s$ :** *S*-wave velocity

## Chapter 1 – Introduction

### 1.1 Background

Coupled *P-P* and *P-S* seismic analysis increases confidence in interpretation, provides additional measurements for imaging the subsurface, and gives rock property estimates. Supplementary *P-S* data from 3-component (3-C) seismic recordings is obtained for a relatively small additional cost, as conventional sources and receiver geometries are employed.

Compressional (*P*) waves impinging on an interface at non-normal incidence are partitioned into transmitted and reflected *P* and shear (*S*) waves. Significant energy is converted to *S* waves which, in the absence of azimuthal anisotropy, will be recorded primarily on the radial (inline horizontal) component of the receiver. Due to the difference in travel path, wavelength, and reflectivity, *P-S* seismic sections may exhibit geologically significant changes in amplitude or character of events which are not apparent on conventional *P-P* sections. Horizons may be better imaged on one or the other of the sections because of different multiple paths and wavelet interference effects such as tuning. It is helpful to have another seismic section to work with in areas where the data quality is poor or the interpretation is unclear.

Through the analysis of multicomponent seismic data, important rock properties such as  $V_p/V_s$  (or similarly, Poisson's ratio) can be extracted. This elastic parameter can improve predictions about mineralogy, porosity, and reservoir fluid type (e.g. Pickett, 1963; Tatham, 1982; Rafavich et al., 1984; Miller and Stewart, 1990). Compressional seismic velocity alone is not a good lithology indicator because of the overlap in  $V_p$  for various rock types. The additional information provided by  $V_s$  can reduce the ambiguity involved in interpretation. Pickett (1963) demonstrated the potential of  $V_p/V_s$  as a lithology indicator through his laboratory research. Using core measurements he determined  $V_p/V_s$  values of 1.9 for limestone, 1.8 for dolomite, 1.7 for calcareous sandstone, and 1.6 for clean sandstone. Subsequent research has generally confirmed these values and has also indicated that  $V_p/V_s$  in mixed lithologies varies linearly between the  $V_p/V_s$  values of the end members (Nations, 1974; Kithas, 1976; Eastwood and Castagna, 1983; Rafavich et al., 1984; Wilkens et al., 1984; Castagna et al., 1985).

Goldberg and Gant (1988) studied full-waveform sonic log data in a limestone/shale sequence and found  $V_p/V_s$  effective at identifying limestone/shale boundaries, but ineffective at identifying fracturing in the limestone. They concluded that  $S$ -wave amplitude attenuation is more useful for detecting fractures.  $S$ -wave amplitude was also attenuated in the shale zones, and thus could also be used for lithology identification in this case. Multicomponent data have been used successfully to differentiate tight limestone from porous reservoir dolomite in the Scipio Trend in Michigan. Pardus et al. (1990) mapped the variation in  $V_p/V_s$  across the interval of interest on  $P$ - and  $S$ -wave seismic data and related it to the ratio of limestone to dolomite. Limestone tends to a  $V_p/V_s$  value of 1.9, dolomite of 1.8.

Seismic velocities are affected by numerous geologic factors including rock matrix mineralogy, porosity, pore geometry, pore fluid, bulk density, effective stress, depth of burial, type and degree of cementation, and degree and orientation of fracturing (McCormack et al., 1985). The complex interaction of these and other factors complicates the task of inverting seismic velocities to obtain petrophysical information. In order to understand how rock properties influence velocity, researchers have employed a variety of approaches such as core analysis, seismic and well log interpretation, and numerical modelling (e.g., Kuster and Toksöz, 1974; Gregory, 1977; Eastwood and Castagna, 1983; McCormack et al., 1984).

Various approaches have been taken to analyze the effect of porosity on velocity. These include the time average equation (Wyllie et al., 1956), the empirical equation by Pickett (1963), and the transit time to porosity transform of Raymer et al. (1980). Domenico (1984) used Pickett's (1963) data to demonstrate that  $V_s$  in sandstones is 2 to 5 times more sensitive to variations in porosity than  $V_p$  in sandstones or  $V_s$  in limestones.  $V_p$  in limestone was found to be the least sensitive porosity indicator.

The model of Kuster and Toksöz (1974) indicates that pore aspect ratio has a strong influence on how  $V_p$  and  $V_s$  respond to porosity (Toksöz et al., 1976).  $V_p/V_s$  appears to be independent of pore geometry unless the aspect ratio is low; less than about 0.01 to 0.05 (Minear, 1982; Tatham, 1982; Eastwood and Castagna, 1983). Robertson (1987) used the Kuster-Toksöz (1974) model to interpret carbonate porosity from seismic data and correlated an increase in  $V_p/V_s$  with an increase in porosity due to elongate pores. According to Robertson's (1987) models,  $V_p/V_s$  will rise as porosity increases in brine-saturated limestone, dolomite, and sandstone if the pores have low aspect ratios. If the pores tend toward high aspect ratios,  $V_p/V_s$  will decrease slightly for carbonates and

increase slightly for sandstones. If carbonates are gas saturated,  $V_p/V_s$  will drop sharply as porosity increases if pores are flat and drops slightly if pores are rounder. For gas-saturated sandstone,  $V_p/V_s$  decreases with increasing porosity if pores are flat, but remains fairly constant for rounder pores. Eastwood and Castagna (1983) examined full-waveform sonic logs and observed constant  $V_p/V_s$  with increasing porosity in an Appalachian limestone and increasing  $V_p/V_s$  with increasing porosity in the Frio Formation sandstones and shales.

Clay content is a significant factor in the study of velocity-porosity relationships in clastic silicate rocks. A number of workers have included a clay term in empirical linear regression equations developed from core analysis data (Tosaya and Nur, 1982; Castagna et al., 1985; Han et al., 1986; King et al., 1988; Eberhart-Phillips et al., 1989). When both porosity and clay effects were studied, porosity was shown to be the dominant effect by a factor of about 3 or 4 (Tosaya and Nur, 1982; Han et al., 1986; King et al., 1988).

Minear (1982) examined the importance of clay on velocities using the Kuster - Toksöz model. Results suggested that clay dispersed in pore spaces has a negligible effect on velocity, however laminated shale and shale in the rock matrix have a similar and significant effect in reducing velocities. Since clay tends to lower the shear modulus of the rock matrix,  $V_s$  decreases more than  $V_p$ , resulting in an overall increase in  $V_p/V_s$ . Tosaya and Nur (1982) concluded that neither clay mineralogy nor location of clay grains were significant factors in the  $P$ -wave response to clay content .

Because  $V_s$  is thought to be more sensitive than  $V_p$  both to porosity (Domenico, 1984) and to clay content (Minear, 1982), an increase in either should result in an increase in  $V_p/V_s$ . This result has been observed in core studies of clastic silicates (Han et al., 1986; King et al., 1988), seismic surveys over carbonates and sand/shale sequences (McCormack et al., 1984; Anno, 1985; Garrotta et al., 1985; Robertson, 1987) and well logging studies of clastic silicates (Castagna et al., 1985). The increase in  $V_p/V_s$  with shaliness has been used in seismic field studies to outline sandstone channels encased in shales (McCormack et al., 1984; Garrotta et al., 1985). Garrotta et al. (1985) used  $V_p/V_s$  analysis of a 3-C survey to predict sand/shale ratios in a Viking channel in the Winfield Oil Field in Alberta. A decrease in  $V_p/V_s$  correlated with an increase in sand channel thickness as determined from well log data. McCormack et al. (1984) used  $V_p/V_s$  analysis to identify sandstones encased in shales in the Morrow Formation in the Empire Abo Field of New Mexico. They observed a decrease in  $V_p/V_s$  moving along the line from a dry hole to

a productive well. The effects of porosity, gas saturation, and sand/shale ratios were modelled; the best fit to the data was a model of increasing sandstone content.

$V_p/V_s$  is sensitive to gas in most clastics and will often show a marked decrease in its presence (Kithas, 1976; Gregory, 1977; Tatham, 1982; Eastwood et al., 1983; Ensley, 1984; Ensley, 1985; McCormack et al., 1985). The  $V_p/V_s$  response of carbonate rocks to gas is variable; a discrepancy which may be attributable to pore geometry.  $V_p/V_s$  reduction has been observed in carbonates with elongate pores (Anno, 1985; Robertson, 1987) and absent in carbonates with rounder pores (Georgi et al., 1989). Anno (1985) reported a good correlation between  $V_p/V_s$  lows and gas production in the Paleozoic carbonates of the Hunton Group of the Anadarko Basin.

## **1.2 Thesis objectives, structure, and datasets used**

A procedure is developed for the coupled interpretation of  $P$ - $P$  and  $P$ - $S$  seismic data, and is illustrated using 3C-2D seismic data from two oil fields in Alberta, Canada. The first case study, described in Chapter 2, is from the Lousana Field in central Alberta, where the target is a late Devonian carbonate buildup encased in an anhydrite basin. The principal objective of the seismic survey was to detect lateral changes from porous reservoir dolomite to tight basinal anhydrite. The second example, described in Chapter 3, is the Blackfoot Field in southeastern Alberta. The targets are Glauconitic incised-valley sandstones and one of the goals of the study was to use seismic analysis to distinguish between regional and incised-valley facies. Having delineated the incised valley, the objective was then to differentiate sandstone fill from shale fill using the multicomponent seismic data. For each case history, there is a brief description of acquisition and processing parameters, with the majority of the discussion devoted to modelling and interpretation results.

Two 3-component (3-C) data sets from Alberta are examined in this thesis. These data sets provided two different play types for the application of multicomponent seismic techniques. The Lousana survey targets a carbonate reservoir encased in evaporites, whereas the Blackfoot Field is a siliclastic incised-valley fill play. The field locations are shown in Figure 1.1.

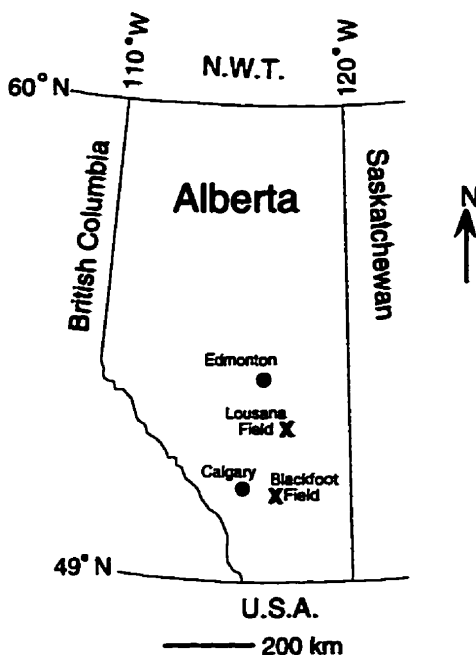


FIG. 1.1 Location map showing the Lousana Field and Blackfoot Field.

### 1.3 Software and hardware used

The Lousana data were processed by Dr. Mark Harrison using the ProMAX processing system and converted-wave code developed by the CREWES Project. Offset synthetic seismograms were created using the Synth algorithm developed by Lawton and Howell (1992). Modelling of multiples for Lousana was done in Hampson-Russell's AVO program, using code developed by Dr. Clint Frazier (pers.comm., 1994). Wavelet extractions were done with Strata, an inversion package from Hampson-Russell Software Services Ltd. Interpretation of both datasets was done with Photon's SeisX application. Cross-section modelling for Blackfoot was done using CREWES code developed by Margrave and Foltinek (1995). All of the computer applications listed above were run on Sun Sparc workstations. The Lousana cross section, zero-offset synthetic seismograms and well-log editing was done using GMA's LogM package running on an IBM PS/2. Crossplots and graphs were made with Igor Pro on the MacIntosh computer. This thesis was written on a MacIntosh computer using MS Word for text and Deneba Canvas and Adobe Photoshop to create some of the figures.

## **Chapter 2 – Lousana Case History**

### **2.1 Geology and Survey Objectives**

A simplified chart of the stratigraphy of the study area is shown in Figure 2.1 (Kohrs and Norman, 1988). The Nisku Formation is in the Winterburn Group, which is of Late Devonian (Frasnian) age (Geological Staff, Imperial Oil, 1950). The Winterburn Group is composed of a lower transgressive phase and an upper regressive phase of platform deposition. It conformably overlies the shales and carbonates of the Woodbend Group. Immediately underlying the Nisku is the Ireton Formation, a calcareous shale approximately 150 m thick in this area (Geological Staff, Imperial Oil, 1950). The Cooking Lake Formation forms a carbonate platform at the base of the Woodbend Group, upon which the Leduc reef complexes developed and provided topographic highs for the later growth of Nisku carbonate platforms (Switzer et al., 1994).

The Lousana field is located west of the Fenn-Big Valley and Stettler Oil Fields in Township 36, Range 21, West of the 4th Meridian (Figure 2.2). The target is a Nisku dolomite buildup which is at a depth of about 1750 m below surface and is separated from the main Nisku carbonate shelf to the east by an anhydrite basin, which forms lateral and vertical seals to the reservoir. The contours in Figure 2.2 show the approximate edges of the carbonate shelf and buildup, and the 10 m porosity contour within the buildup, as determined from well control (A. Bell, pers. comm., 1993). For many of the wells, the log suite was limited and the log quality poor, thus the contours are only approximate.

The Nisku Formation consists of a lower open-marine carbonate unit and an upper evaporitic unit deposited in an environment of reduced circulation (Switzer et al., 1994). Stoakes (1992) describes the initial deposition of the carbonate interval as having occurred during a relative rise in sea level as the carbonates shelves backstepped away from the central Alberta basin. The antecedent topography of the Bashaw Leduc reef complexes served as sites for stromatoporoid-rich platform carbonate growth, which was concentrated in shallow waters. Deposition in deep-water areas was restricted to a thin condensed unit, pinnacle reefs and small carbonate outliers. These deep-water regions are referred to by Dixon et al. (1991) as "the moat".



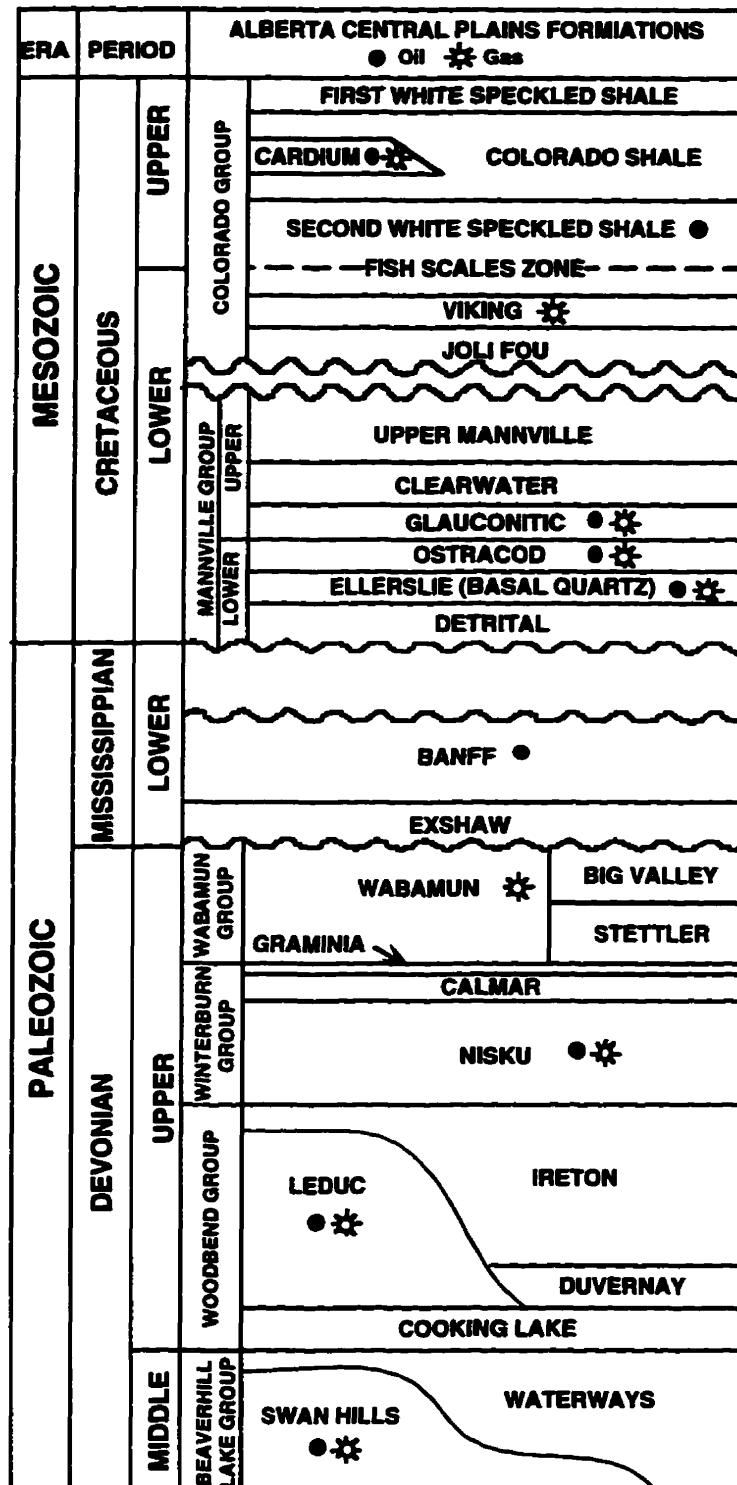


FIG. 2.1 Simplified stratigraphic nomenclature of Devonian, Mississippian, and Cretaceous successions in central plains of Alberta (after Kohrs and Norman, 1988).

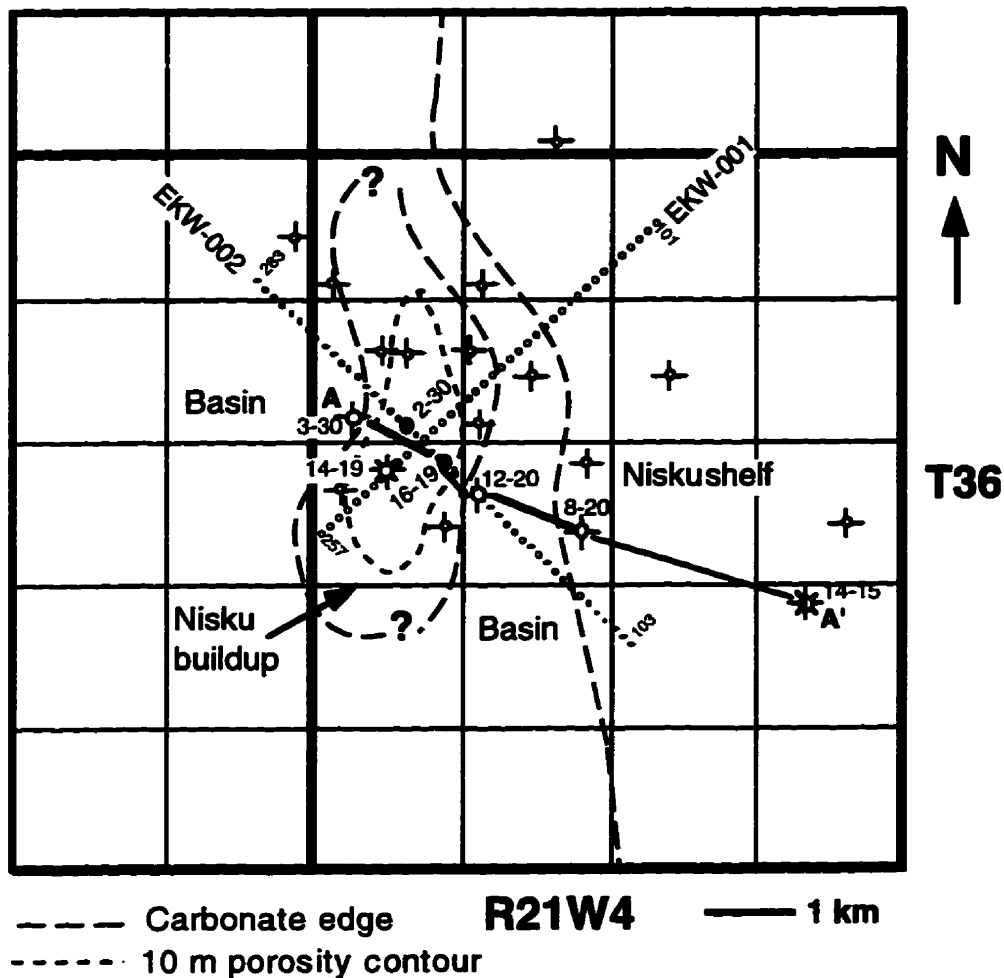


FIG. 2.2 Shotpoint map of the Lousana survey showing seismic Lines EKW-001 and EKW-002, cross-section A-A', and Nisku well control. Carbonate edge and 10 m porosity contours are based on well control and are approximate only.

The nearby Fenn-Big Valley, and Stettler Fields are structural traps formed by the porous dolomitized Nisku shelf carbonates draping over Leduc reefs (Rennie et al., 1989). There is no underlying Leduc at Lousana, which is west of the Leduc edge, and the stratigraphic trap is a biohermal buildup of dolomite, perhaps one of the carbonate outliers described by Stoakes (1992).

During a later, regressive phase of deposition, sea water circulation was restricted by the growth of the shelf margin in the northwest, the current location of the West Pembina Field (Stoakes, 1992). Progressive evaporation resulted in the hypersaline deposits of the upper evaporitic unit in the Nisku. Brining upward cycles of dolomudstones and laminated and bedded anhydrites onlap-filled the lows between isolated reefs and platforms and capped the succession. These hypersaline deposits of the upper

phase of the Nisku infilled the basin between the shelf and the dolomitic buildup at Lousana, and sealed the trap. During this hypersaline phase, sea level was at a relative stillstand (Stoakes, 1992). The carbonate platforms, with varying levels of evaporitic and terrigenous components, commenced progradation seawards into the basin. Basin infilling was completed by the deposition of the fine silts and shales of the overlying Calmar Formation (Andrichuk and Wonfor, 1954).

The Calmar Formation is generally about 3 m thick and marks the top of the Winterburn Group at Lousana. It is unconformably overlain by the Wabamun Group, which is made up primarily of carbonate rocks interbedded with salt horizons. The Wabamun unconformity surface is at the top of the Devonian succession and is overlain by the Banff and Exshaw Formations of Mississippian age (Kohrs and Norman, 1988). The Mississippian unconformity marks a significant and abrupt transition from the predominantly carbonate Paleozoic strata to the predominantly siliclastic deposits of the overlying Cretaceous section. Triassic and Jurassic sequences are absent in the study area.

The Nisku Formation is 50 to 60 m thick at Lousana with up to 25 m of porosity in producing wells. The primary hydrocarbon is oil, although gas is sometimes present. The two oil wells in the field, 16-19-36-21W4 and 2-30-36-21W4 (Figure 2.2), have about 25 m of porosity and 10 m of pay. The 16-19 well went into production in 1960 and has produced about 90,000 m<sup>3</sup> of oil to date. The 2-30 well has produced over 58,000 m<sup>3</sup> of oil since it went into production in 1962. There is one Nisku gas well in the field, 14-19-36-21W4, which was put into production in 1994 and has produced 730,000 m<sup>3</sup> of gas. The porosity is primarily vuggy, ranging to intergranular, and averages about 10% in the producing wells. Dry holes in the field are either tight or wet carbonate, or massive anhydrite at the Nisku level. There is also gas production from the Viking and other Lower Cretaceous formations in this area.

A geological cross-section (A-A', shown in Figure 2.2), is approximately parallel to line EKW-002, and is constructed from sonic logs from each of the Nisku shelf, basin, and reef environments (Figure 2.3). This study focuses primarily on two wells: the 16-19-36-21W4 oil well, and 12-20-36-21W4 well, which penetrated tight anhydrite at the Nisku level; both wells are on line EKW-002. Another oil well, 2-30-36-21W4, is also on line EKW-002, but it does not have a sonic log. There is one well on line EKW-001, 14-19-36-21W4, which has 17 m of porous dolomite within the Nisku Formation.

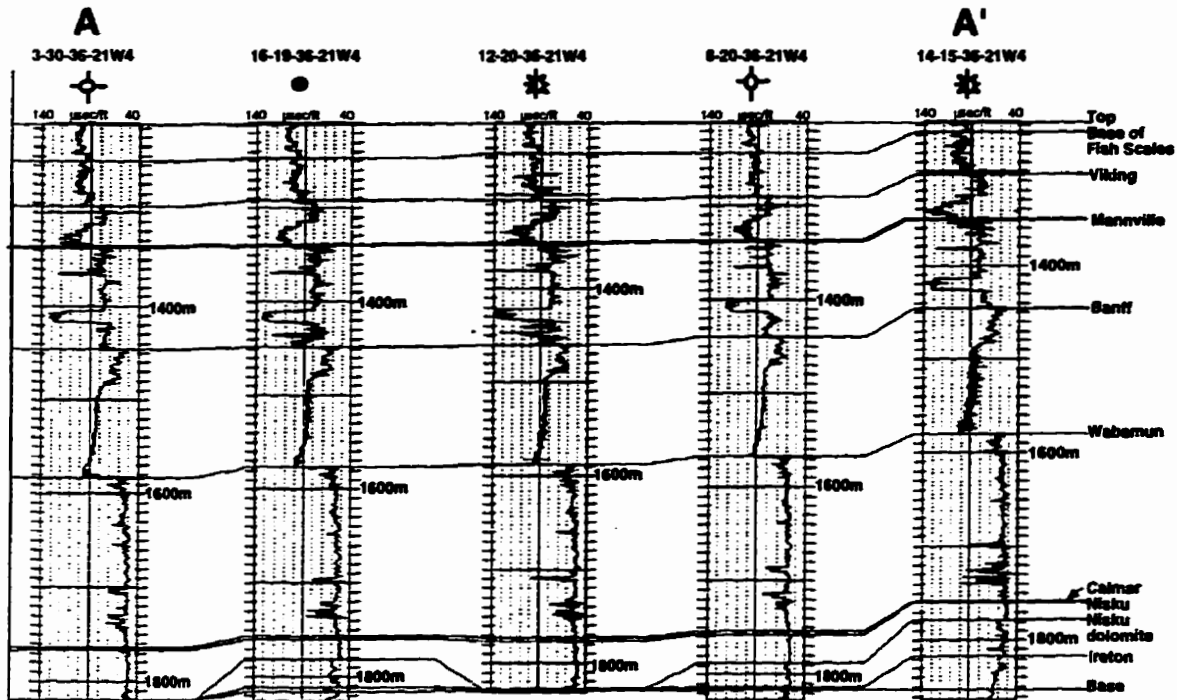


FIG. 2.3 Cross-section A-A' using sonic logs from wells from the basinal (3-30, 12-20), porous dolomite buildup (16-19), and carbonate shelf (14-15, 8-20) environments. 14-15 and 12-20 are suspended gas wells, with gas occurring in the Viking Formation.

The objective of this survey was to determine if multicomponent seismic data analysis can discriminate between the productive porous dolomites of the reefal environment and the tight anhydrite in the basin.

## 2.2 Seismic survey acquisition and processing

The main emphasis of this work is the interpretation and modelling of the Lousana multicomponent data set. The field design, acquisition, and processing were not part of the work undertaken for this thesis and therefore are not described in great detail. The seismic data were acquired in 1987 by Unocal Canada Ltd., and subsequently donated to the CREWES Project at the University of Calgary. The data were reprocessed by Dr. Mark Harrison, as described in Miller et al. (1994), using the ProMAX processing package and converted-wave processing code developed in CREWES. Well data, including log digits, tickets, production data, and tops, were obtained from the Digitech data base.

### 2.2.1 Seismic survey acquisition

The seismic survey over the Lousana field is located in Township 36, Range 21, West of the 4th Meridian, in central Alberta, Canada. There are two orthogonal 3-C lines: line EKW-001 is 5 km long and trends NE to SW and line EKW-002 is 6 km long and is oriented SE to NW (Figure 2.1). The field acquisition parameters are summarized in Table 2.1. The energy source was dynamite, with a single shot of 2 kg at 18 m for line EKW-001 and a 4-hole pattern of 0.5 kg at 5 m for line EKW-002. An array of six three-component geophones was used at each receiver station. The geophones were positioned with one horizontal component (H1) in a north-south orientation, and the other (H2) in an east-west direction. The data were recorded on two 240-trace Sercel SN-348 recording systems; one to record the vertical and one of the horizontal components, and the other to record the second horizontal component. Data were typically collected from 110 receivers for each shot using a split-spread layout for a nominal fold of 27.

Table 2.1 Field acquisition and recording parameters for the Lousana survey.

Energy source	dynamite
Source pattern, EKW-001	single hole, 2 kg at 18 m
Source pattern, EKW-002	4 holes, 0.5 kg charges at 5 m
Amplifier type	2 - Sercel SN348
Number of channels	2 x 240
Sample rate	2 ms
Recording filter	out-240 Hz, Notch out
Geophones	OYO 3-C, 10 Hz
Geophones per group	6 spread over 33 m
Number of groups recorded	110
Group interval	33 m
Normal source interval	66 m
Nominal fold	27
Spread	split

The data were acquired with the horizontal components of the geophones oriented at  $\pm 45^\circ$  to the line direction resulting in comparable levels of *S*-wave energy on the H1 and H2 components. A  $45^\circ$  geometric rotation transformed the records into radial and transverse components. The angle of rotation was confirmed by an energy maximization analysis. For both lines, the rotation angle that maximized the energy on the output radial component was found to be  $45 \pm 2$  degrees, with considerable record-to-record variance (Miller et al., 1994).

Examples of vertical- and (post-rotation) radial-component source gathers are shown in Figure 2.4, with time-variant gain and trace scaling applied. The records have

good signal strength, and are of similar quality. The radial-component record has been plotted at 2/3 the scale of the vertical-component record to facilitate visual correlation of events. The high amplitude reflection at about 1200 ms (*P-P*) and 1800 ms (*P-S*) on the far offset traces marks the transition from Mesozoic (Cretaceous) siliclastic rocks to Paleozoic carbonate rocks at the Mississippian unconformity. After the 45° rotation, there was little signal evident on the transverse component, thus all *P-S* processing involved only the radial component.

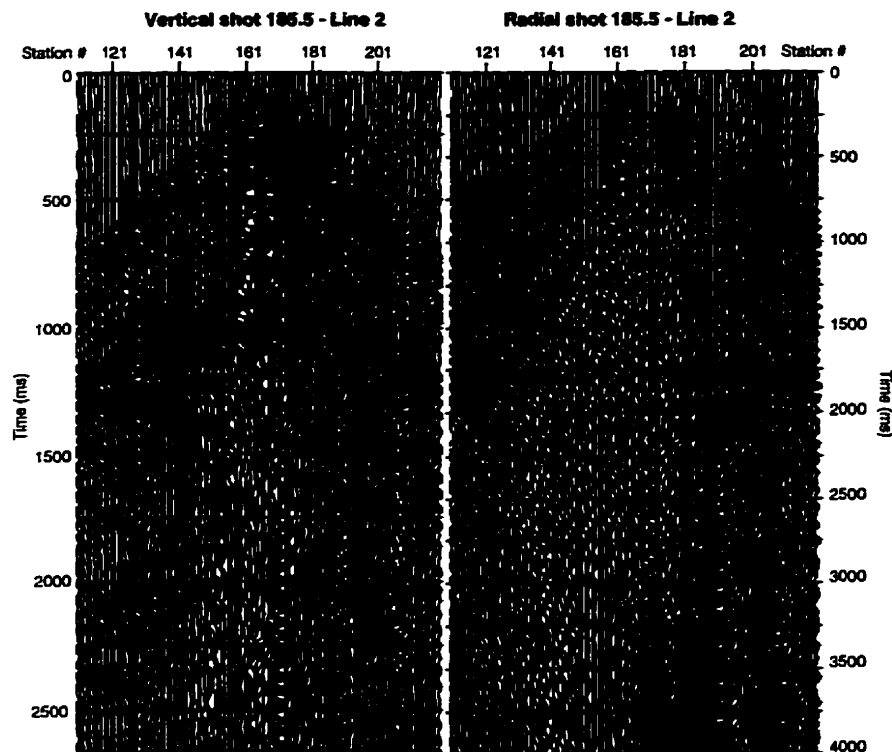


FIG. 2.4 (a) Vertical-component shot record and (b) radial-component shot record from line EKW-002, shotpoint 185.5.

### 2.2.2 Seismic data processing

The vertical component data were processed by Dr. Mark Harrison (pers.comm., 1994) using a standard flow as outlined in Figure 2.5 (Miller et al., 1994). The final migrated *P-P* sections used for the interpretation are shown in Figures 2.6 and 2.7.

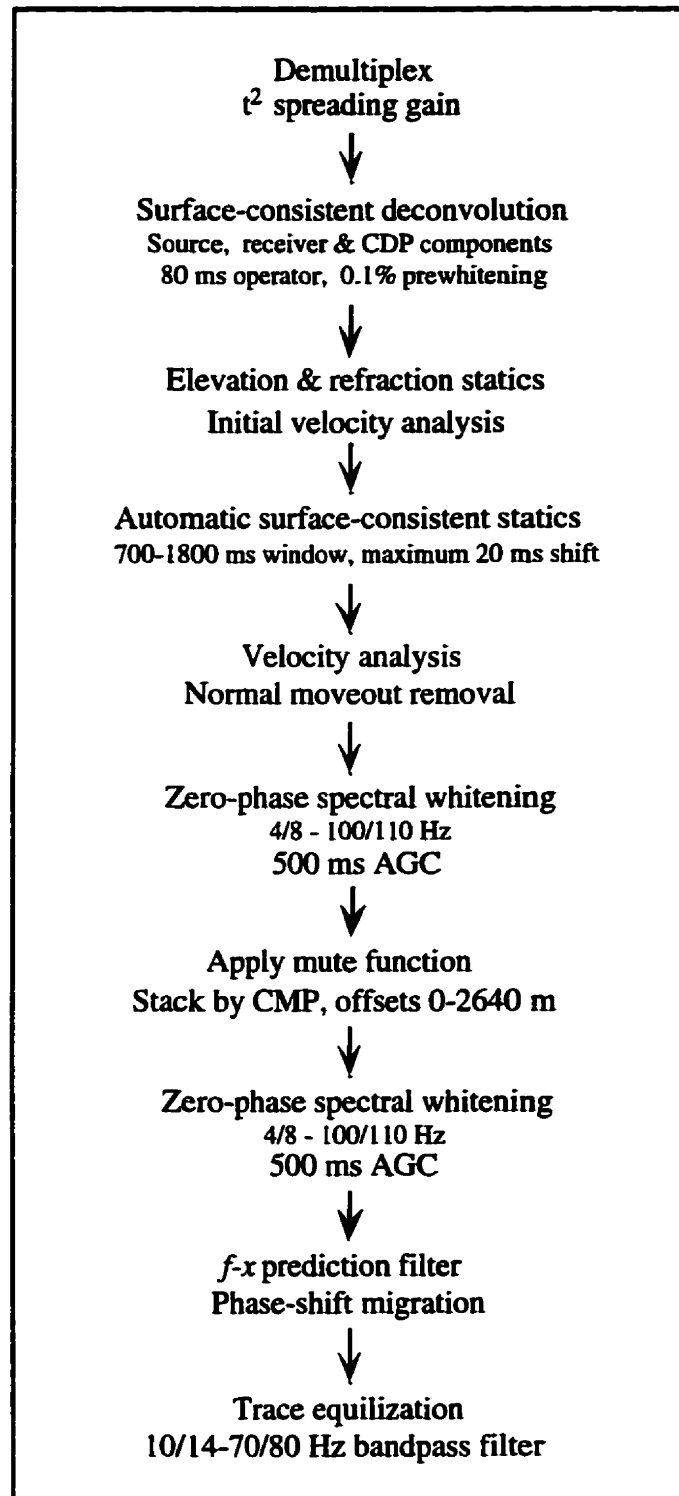
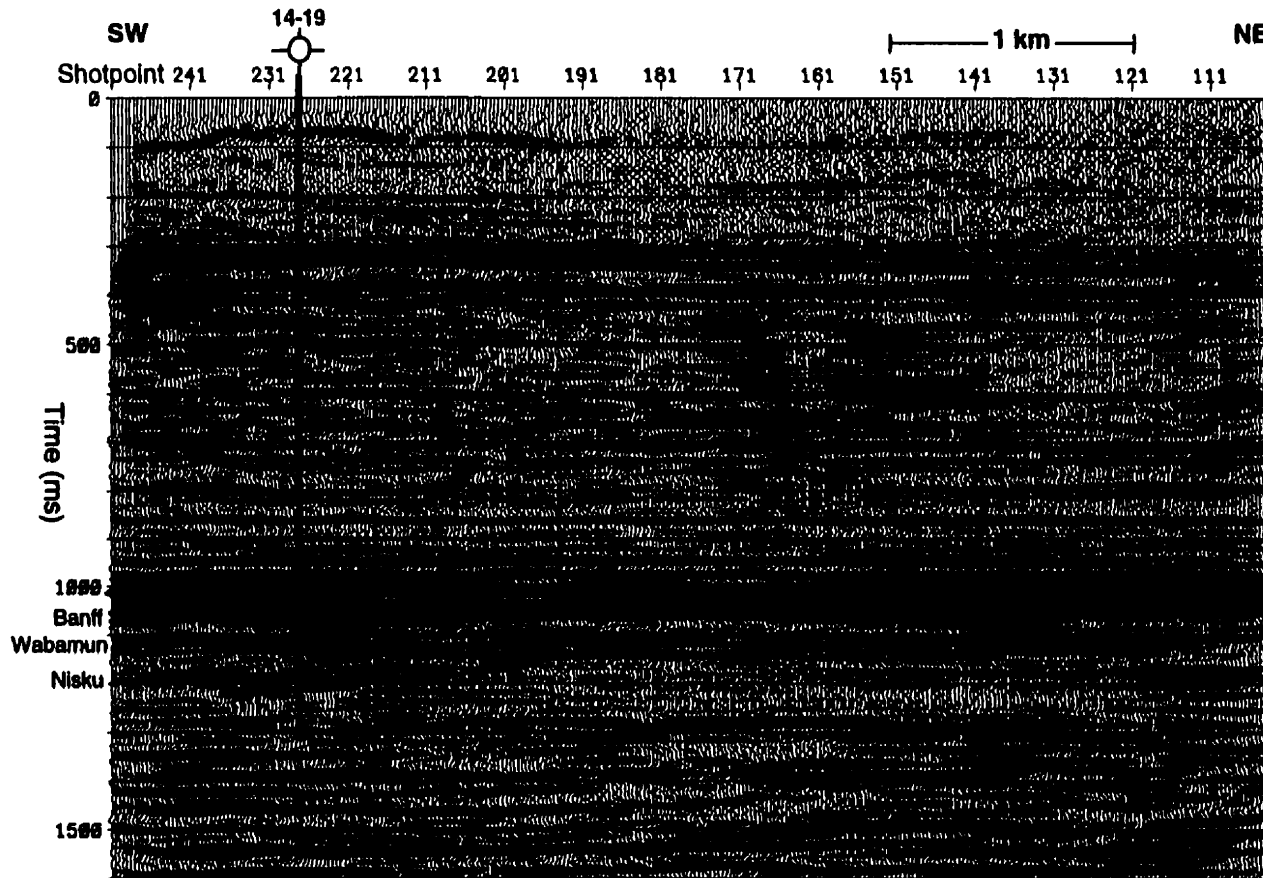


FIG. 2.5 Processing flow for the vertical-component ( $P-P$ ) seismic data.



**FIG. 2.6** Migrated *P-P* stacked section for Line EKW-001 showing location of the well which intersects the line. The zone of interest is the Nisku Fm at about 1200 ms.



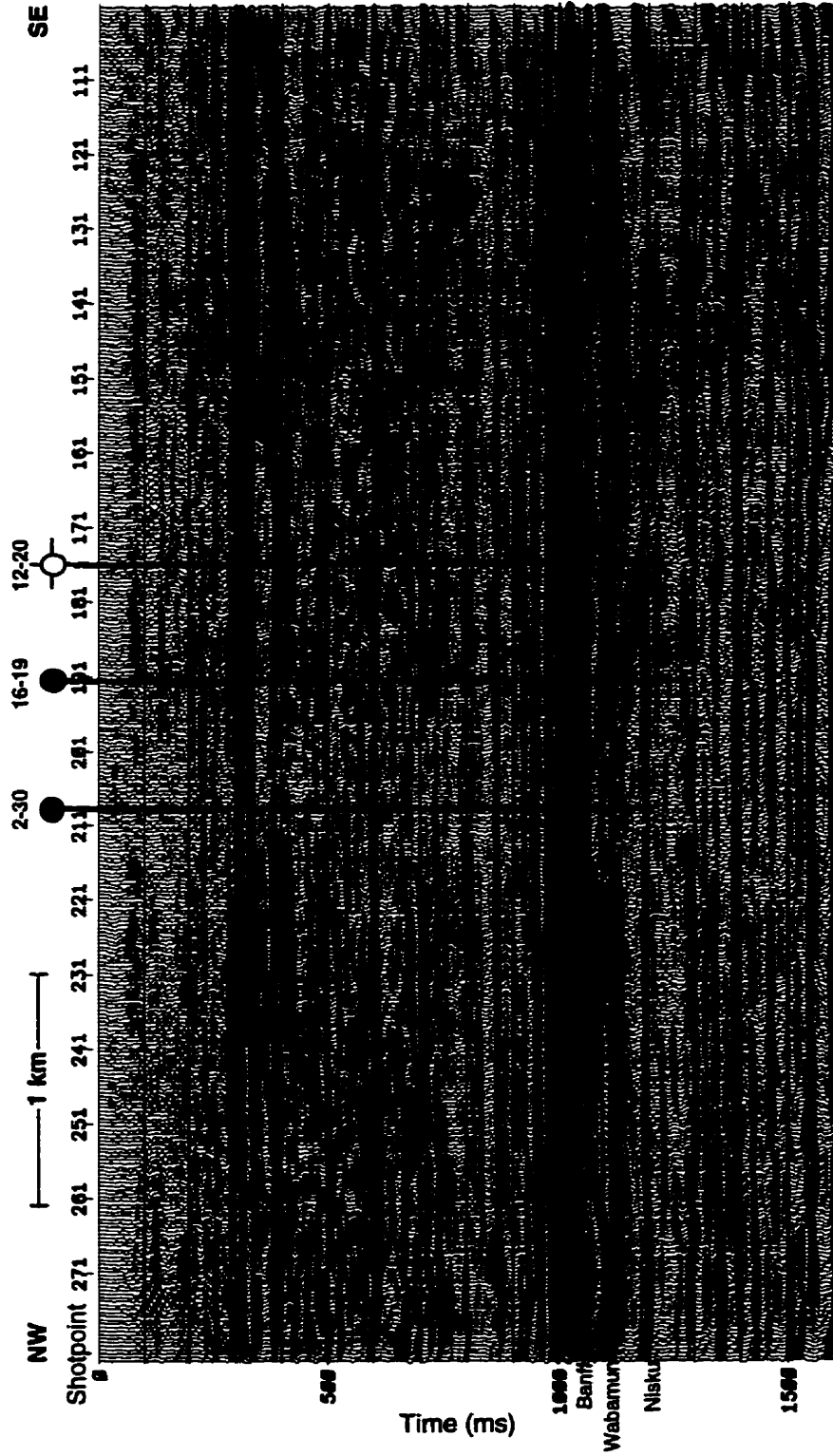


FIG. 2.7 Migrated *P-P* stacked section for Line EKW-002 showing locations of the wells which intersect the line. The zone of interest is the Nisku Fm at about 1200 ms.

The radial (*P-S*) component data were processed by the same contractor using the sequence shown in Figure 2.8 (Miller et al., 1994). The flow was based on converted-wave processing methods documented in part by Eaton et al. (1990), Harrison (1992), and Harrison and Stewart (1993). Residual receiver statics, picked by hand from common-receiver stack sections, were in the range of  $\pm 50$  ms. After conventional hyperbolic NMO correction, a shot-mode *f-k* filter was applied to reduce low-velocity linear noise. NMO was then restored and a second pass of surface-consistent deconvolution was applied to better whiten the data after removal of the linear noise.

The *P-S* data were initially stacked using asymptotic conversion-point binning and an approximate  $V_p/V_s$  value. The stack of line EKW-001 was then used to derive interval  $V_p/V_s$  values by correlating events with a series of *P-S* synthetic records (Lawton and Howell, 1992). These synthetic gathers used the *P*-wave sonic log from well 16-19-36-21W4 and constant  $V_p/V_s$  values ranging from 1.8 to 2.2. For each interval, the  $V_p/V_s$  value which gave the closest tie to the stacked section was used to rebin the data using depth-variant common-conversion point binning (Eaton et al., 1990). Poststack processing included zero-phase deconvolution, *f-x* prediction filtering, and phase-shift migration using modified migration velocities (Harrison and Stewart, 1993). The resulting migrated stack sections are shown in Figures 2.9 and 2.10 for lines EKW-001 and EKW-002, respectively.

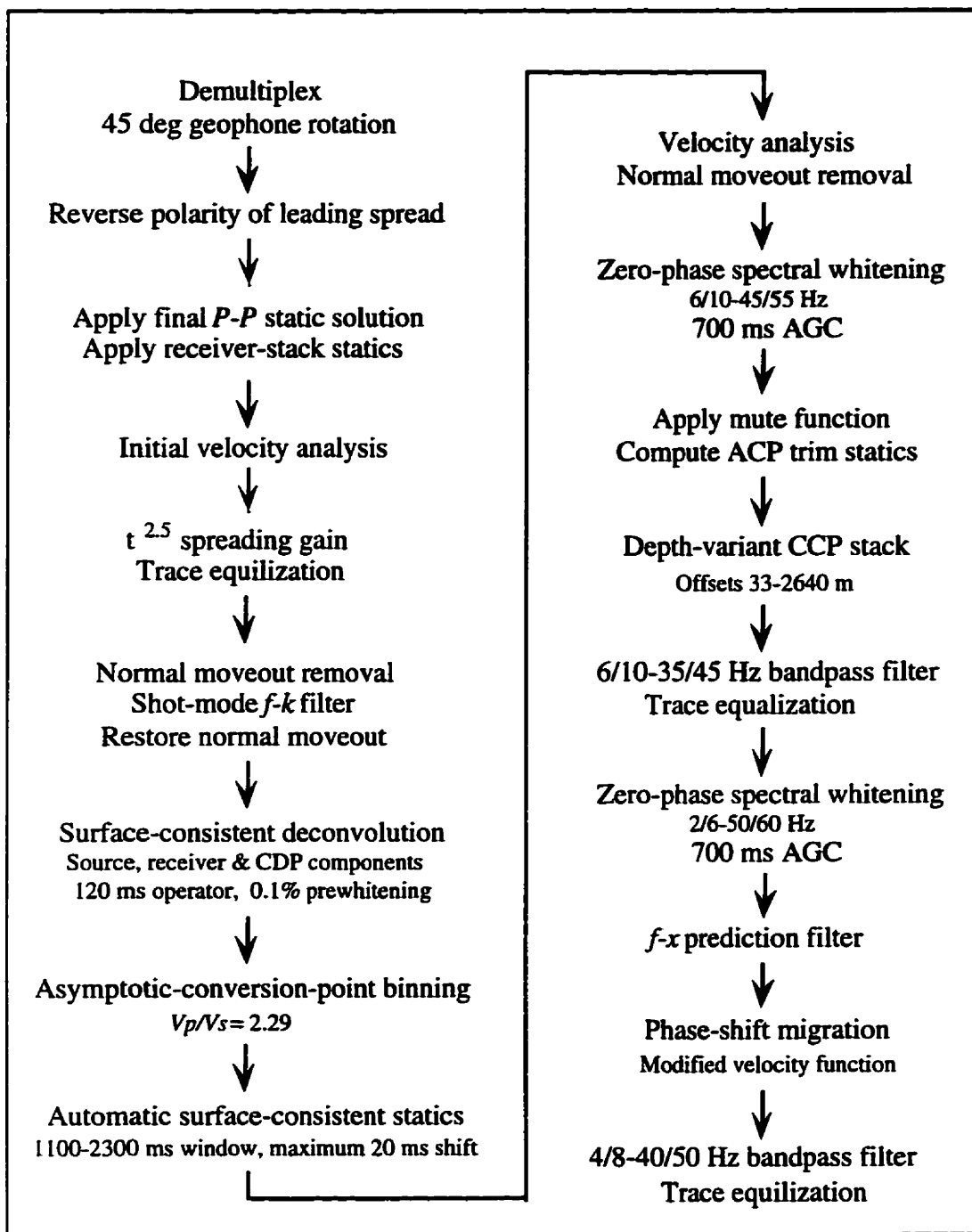
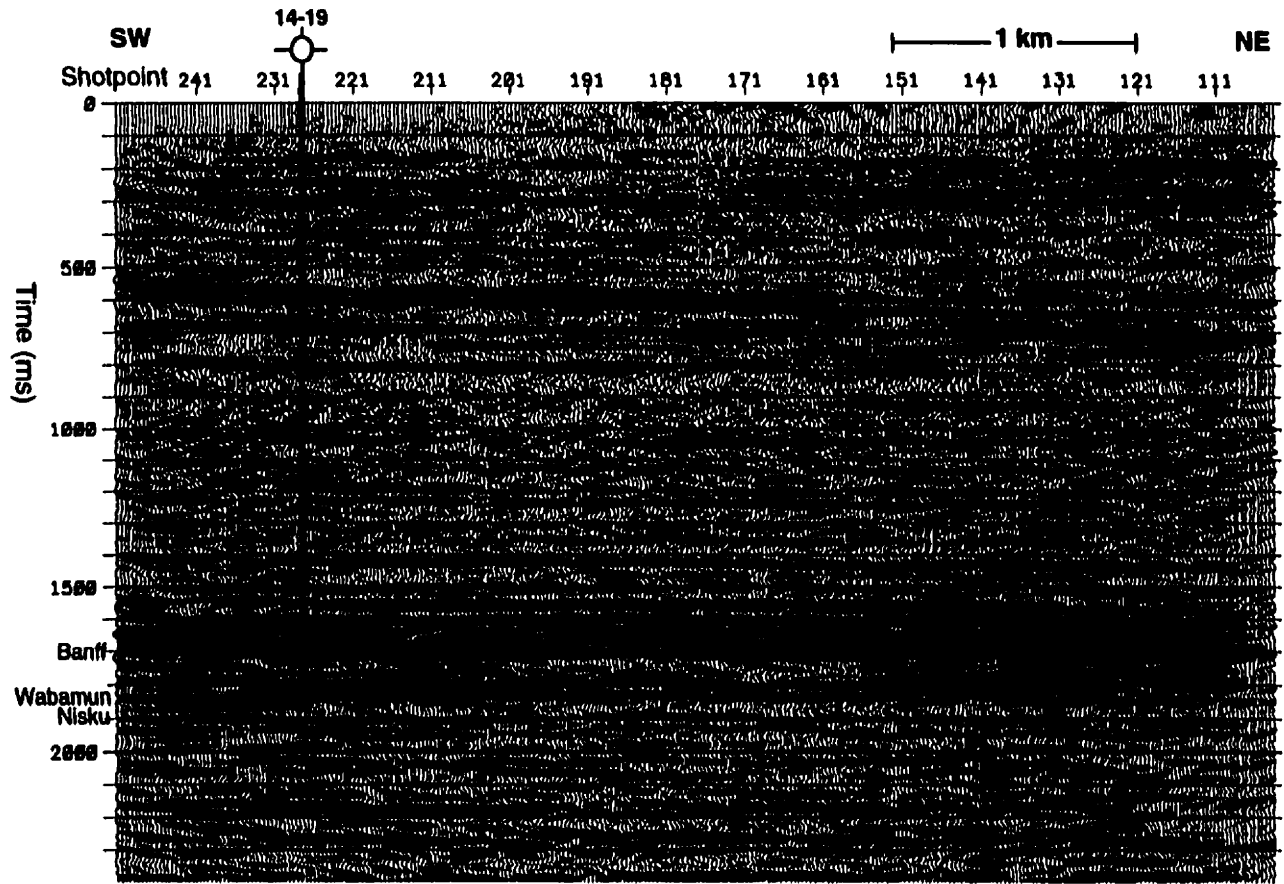


FIG. 2.8 Processing flow for the radial-component ( $P$ - $S$ ) seismic data.



**FIG. 2.9** Migrated *P-S* stacked section for Line EKW-001 showing location of the well which intersects the line. The zone of interest is the Nisku Fm at about 1900 ms.

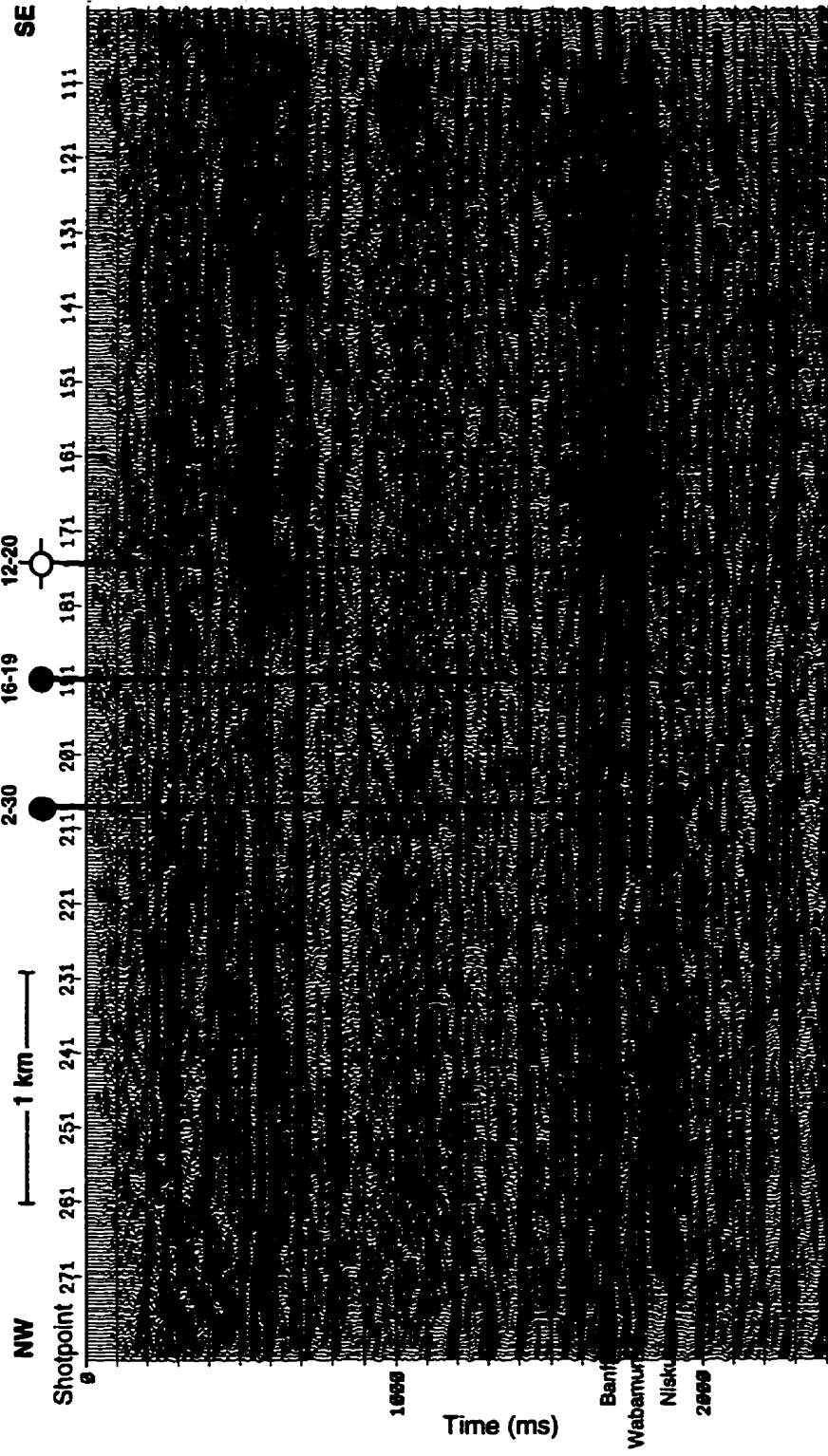


FIG. 2.10 Migrated P-S stacked section for Line EKW-002, showing locations of the wells which intersect the line. The zone of interest is the Nisku Fm at about 1900 ms.

## 2.3 Seismic Interpretation

The seismic interpretation consisted of three steps. First, the  $P$ - $P$  and  $P$ - $S$  seismic sections were correlated to enable coupled  $P$ - $P$  and  $P$ - $S$  seismic analysis. This was followed by two methods of determining  $V_p/V_s$ : the first used synthetic seismograms and the  $P$ - $S$  data only and was applied at the well locations, whereas the second method used corresponding isochron intervals from both the  $P$ - $P$  and  $P$ - $S$  seismic sections.

### 2.3.1 Correlation of $P$ - $P$ and $P$ - $S$ seismic sections

Vertical and radial components were visually examined at the intersection between the two orthogonal lines for evidence of velocity anisotropy. The vertical component sections of lines EKW-001 and EKW-002, spliced together at the line intersection, are shown in Figure 2.11. There is a good tie between events throughout the section.

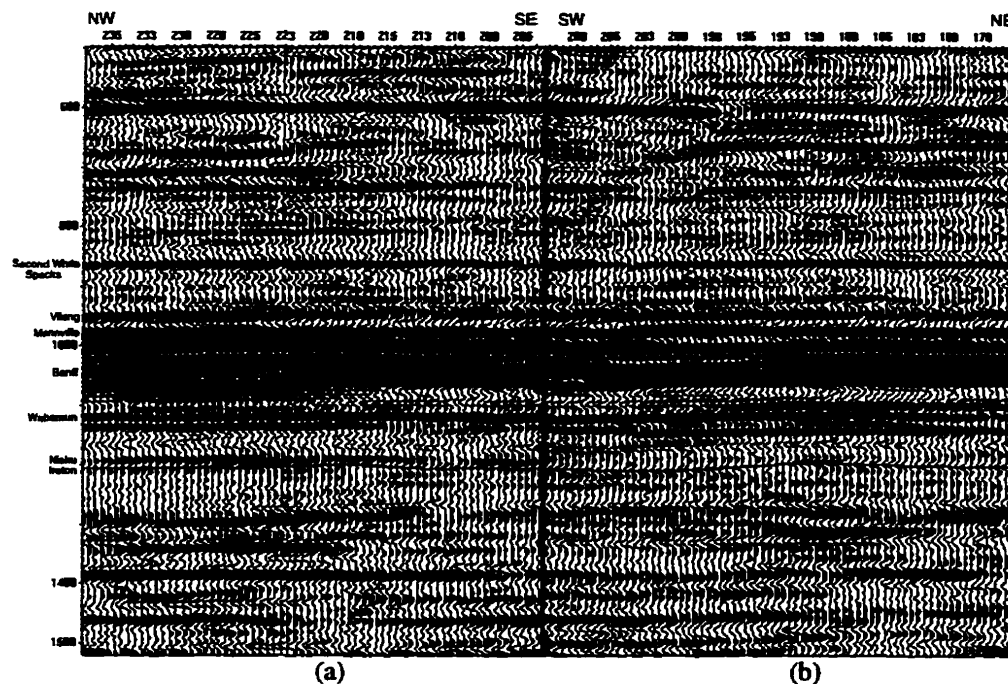


FIG. 2.11 Comparison of (a) Line EKW-001 and (b) EKW-002 for the vertical component.

The radial component of line EKW-001 is parallel to the regional larger principal stress direction, which is orthogonal to line EKW-002 and the lesser principal stress direction (Bell et al., 1994). In the presence of  $S$ -wave velocity anisotropy, mis-ties would be observed between the two sections. As shown in Figure 2.12, the events tie well, thus there does not appear to be significant azimuthal  $S$ -wave anisotropy in the area.

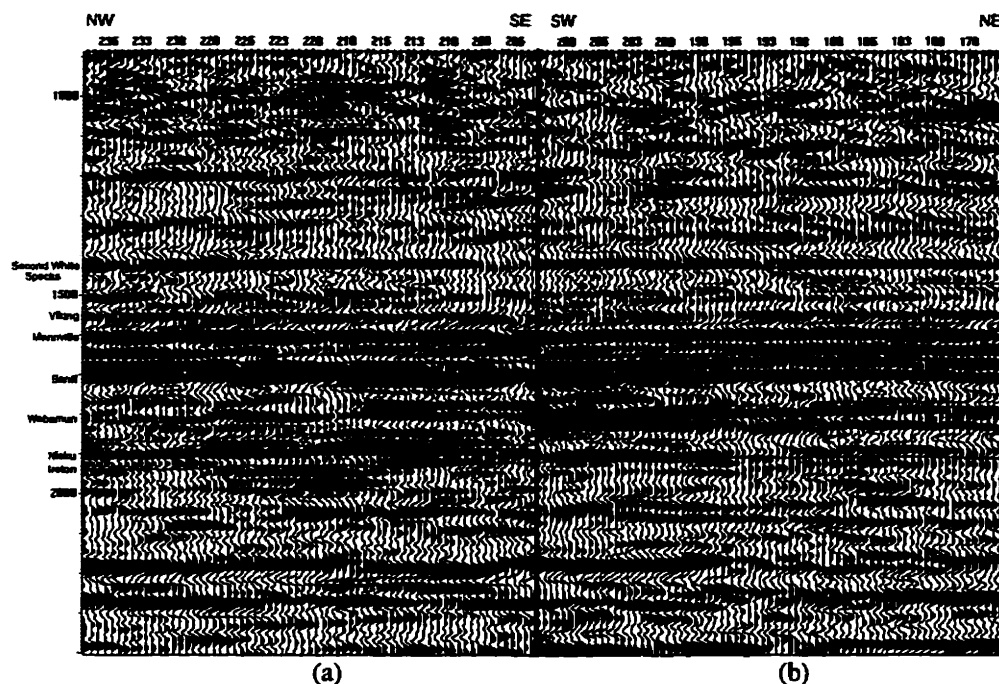


FIG. 2.12 Comparison of (a) Line EKW-001 and (b) EKW-002 for the radial component. The good tie between events indicates that  $S$ -wave anisotropy is not significant in this area.

The first step in the coupled interpretation procedure is the correlation of horizons between the  $P$ - $P$  and  $P$ - $S$  seismic sections. Events were first identified on the  $P$ - $P$  data using the conventional approach of matching a synthetic seismogram to the seismic data. For the  $P$ - $P$  synthetic seismogram, the  $P$ -wave sonic curve used was that from the 16-19-36-21W4 well. There was no density log from this well, so the density log from 8-20-36-21W4 was modified to match the depths of the 16-19 well. Using these input logs, offset synthetic seismograms were generated using a ray-tracing procedure documented by Lawton and Howell (1992). Only primary events are included in this procedure. The source-receiver offsets were from 0 to 1584 m, with a receiver interval of 66 m, compared to the field acquisition geometry with offsets from 16.5 m to 1799 m and a receiver interval of 33 m. The  $P$ - $P$  synthetic data are from the vertical component of the receiver. Ricker wavelets were used, with a peak frequency of 40 Hz, as determined by spectral analysis of the processed seismic data. The wavelet phase can also be adjusted but in this case, zero-

phase wavelets gave the best tie. Normal moveout corrections and mutes were applied prior to stacking the offset traces. The correlation of the  $P$ - $P$  offset synthetic seismogram to the  $P$ - $P$  seismic data is shown in Figure 2.13.

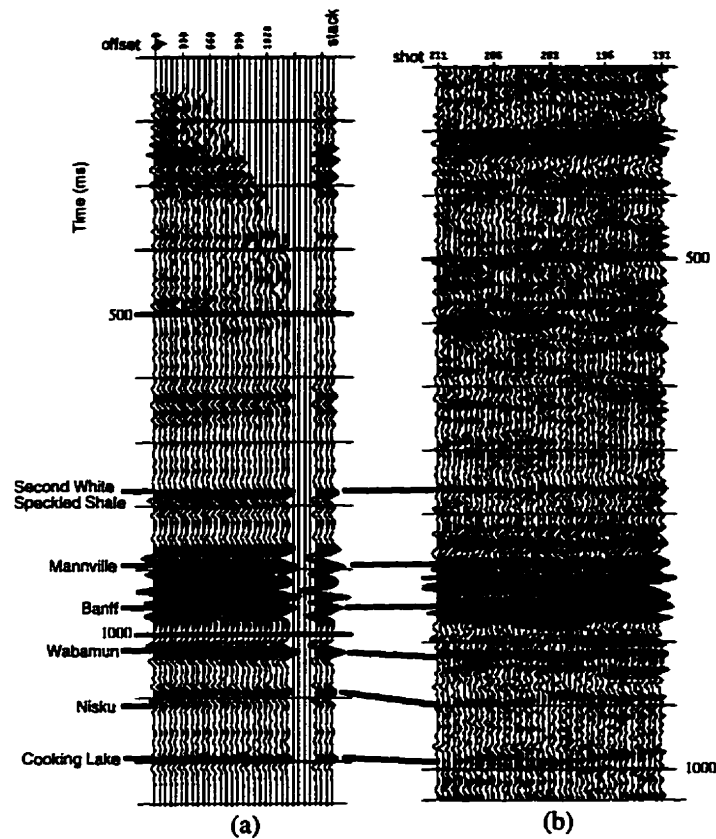


FIG. 2.13 Correlation of (a) the  $P$ - $P$  synthetic seismogram from the 16-19 well with (b) the  $P$ - $P$  seismic data from Line EKW-002 (synthetic seismograms are not shifted to the seismic datum).

The tie is very good for the upper part of the section. Since a checkshot survey was not available, the sonic and density logs were stretched slightly to match the data down to the Banff event. Mis-ties occur below the Banff, but the logs were not adjusted to match these events as the mis-ties are mostly likely due to interference from short path interbed multiples, probably originating in the coal beds of the Mannville Formation. This multiple energy also appears to interfere with the primary reflections deeper in the section. A mis-tie occurs at the Nisku, causing uncertainty in the seismic pick for this horizon. The mis-ties at the Wabamun and Nisku horizons motivated the modelling studies discussed later in this thesis, in which the problem of multiple contamination is addressed.



In an attempt to improve the tie between the synthetic seismogram and the seismic data, wavelets were extracted from the data. These wavelets were also phase rotated in 15° increments from 0° to 180° and tied to the data. The extracted wavelets did not resolve the mis-ties and so were not used for the final analysis.

There are no full-waveform sonic logs available from this area, so the *S*-wave transit time curve was calculated initially using the *P*-wave sonic curve from the 16-19-36-21W4 well and assuming a constant  $V_p/V_s$  of 2.00. An offset synthetic *P-S* seismogram was then generated using from *S*-wave curve and the adjusted density curve from 8-20-36-21W4. Raytracing was performed using offsets from 0 to 1584 mm, with a receiver interval of 66 m. The *P-S* synthetic data are from the horizontal component of the receiver. A Ricker wavelet with a peak frequency of 25 Hz was used, as determined by spectral analysis of the processed *P-S* seismic data. A zero-phase wavelet gave the best tie. Prior to stacking, normal moveout corrections were applied using the non-hyperbolic correction described by Slotboom et al. (1990) as this technique flattened the events better than a conventional NMO correction. The synthetic shot gather was muted to remove NMO stretch prior to stacking.

The correlation between the *P-P* and *P-S* offset synthetic stacks was straightforward as they were both created using the same depth model (Figure 2.14). This correlation procedure, using synthetic offset ray-traced gathers and stacks, is necessary because of the different bandwidths and dominant frequencies between the *P-P* and *P-S* data. Polarity convention used is that a peak on both the *P-P* and the *P-S* data represents an event from an interface with an increase in elastic impedance. Although the *P-S* seismogram has narrower bandwidth, the major events can be identified on the *P-S* seismogram using the tops from the 16-19 well. The *P-S* synthetic seismogram was then used to identify events on the *P-S* seismic section at the well location through visual inspection. Events were identified on the basis of approximate traveltimes, character, and relative amplitudes. Although many of the *P-S* events can be correlated confidently, there is a time-variant mis-tie between the *P-S* synthetic stack and the *P-S* seismic data. This occurs because the seismogram was created using a constant value for  $V_p/V_s$ , whereas in reality,  $V_p/V_s$  varies with depth.

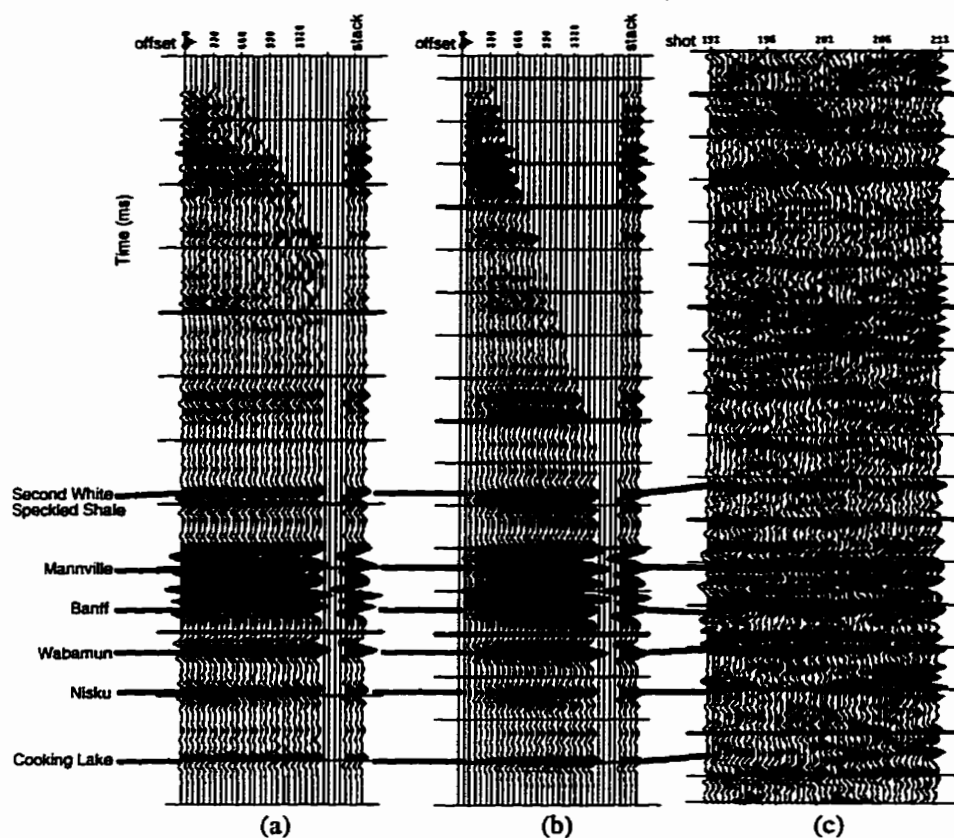


FIG. 2.14 (a) the  $P$ - $P$  synthetic seismogram from the 16-19 well is tied to (b) the  $P$ - $S$  offset synthetic seismogram. The  $P$ - $S$  synthetic seismogram is then correlated to (c) the  $P$ - $S$  data from Line EKW-002. Mis-ties are due to use of a constant  $V_p/V_s$ .

### 2.3.2 $V_p/V_s$ extraction at the well location

The use of a constant  $V_p/V_s$  results in a mis-tie between corresponding events on the  $P$ - $S$  synthetic stack and the  $P$ - $S$  seismic data (Figure 2.13). The change in  $V_p/V_s$  contains geologic information which we wish to extract from the data. To accomplish this, the interval  $V_p/V_s$  was adjusted to stretch or squeeze the synthetic stack in a time-variant manner in order to provide an optimum tie between the synthetic seismogram and the processed data. To show the effect of varying  $V_p/V_s$  and to determine the correct interval  $V_p/V_s$  at the well location, a suite of  $P$ - $S$  offset synthetic stacks was generated using a range of constant  $V_p/V_s$  values from 1.60 to 2.30, in steps of 0.05 (every other step shown in Figure 2.15). Since the interval  $V_p$  was available from the  $P$ -wave sonic log,  $V_p/V_s$  was varied by changing  $V_s$  while keeping  $V_p$  constant within a particular interval. These stacks show how the seismogram is stretched progressively in time as  $V_p/V_s$

increases. Character changes are also evident due to differing interference between adjacent events.

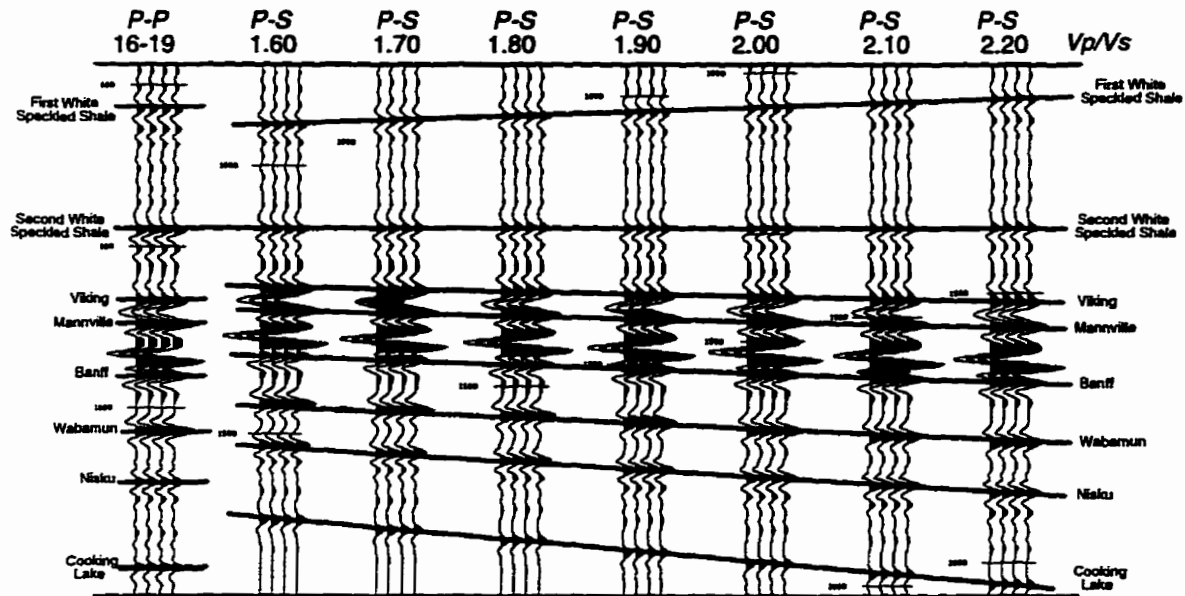


FIG. 2.15 The  $P$ - $P$  offset synthetic stack is compared to a series of  $P$ - $S$  offset synthetic stacks generated from the 16-19  $P$ -wave sonic log and constant  $V_p/V_s$  values ranging from 1.60 to 2.20 in steps of 0.05; every other one is shown here. The stacks are flattened on the Second White Speckled Shale.

For a given interval, the optimum  $V_p/V_s$  was determined from the  $P$ - $S$  synthetic stack which best matched the seismic section, using careful visual inspection. The depth-variant  $V_p/V_s$  values so derived were then used to compute an  $S$ -wave sonic log from the  $P$ -wave sonic log. The final  $P$ - $S$  offset synthetic seismogram was then generated using the  $P$ -wave sonic log, the derived  $S$ -wave interval velocity data, and the density log, resulting in an optimum tie with the  $P$ - $S$  data for those intervals. This procedure was done at both the wells on line EKW-002, with results shown in Figure 2.16. The interval from the Banff to the Ireton includes the target Nisku Formation.  $V_p/V_s$  for this interval is 1.75 at the 16-19 oil well, and 2.10 at the 12-20 basinal well. The transition from porous dolomite to anhydrite within the Nisku Formation most likely contributes to this increase in  $V_p/V_s$ , as discussed later in section 2.4.

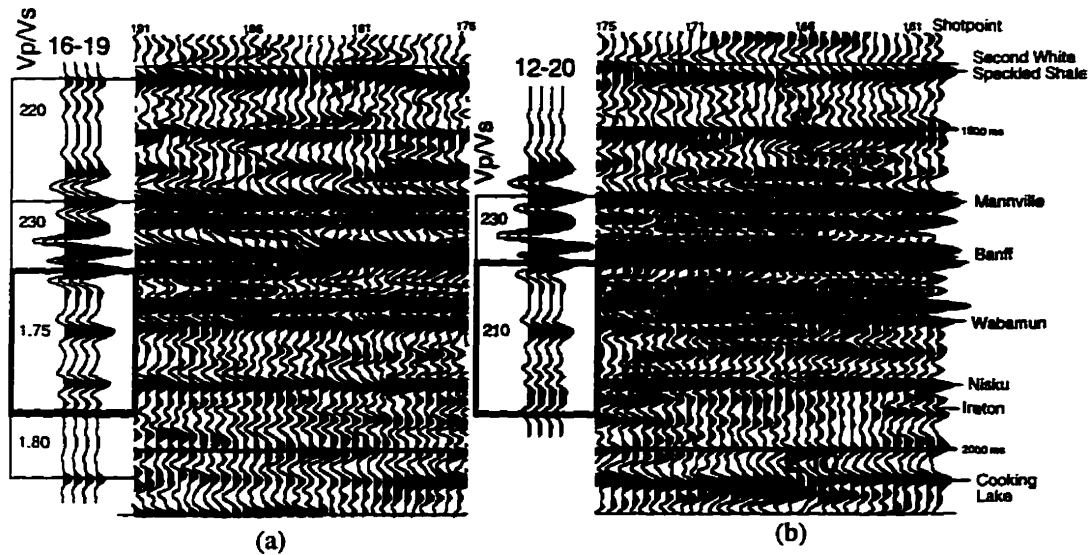


FIG. 2.16 *P-S* synthetic stacks from (a) 16-19 and (b) 12-20 with interval  $V_p/V_s$  which provide the optimum tie to the data.  $V_p/V_s$  for the Banff to Ireton interval (heavily outlined) is 1.75 at 16-19, where the Nisku Formation is porous dolomite and 2.10 at 12-20, where it is tight anhydrite.

### 2.3.3 Horizon interpretation

Once the events of interest were identified and correlated on both the *P-P* and *P-S* sections at the well location, horizons were picked for the remainder of the line on a workstation. Interval  $V_p/V_s$  values between any two picked horizons were calculated. The relationship is (Garotta, 1987):

$$V_p/V_s = (2I_s/I_p) - 1 \quad (1)$$

where  $I_s$  and  $I_p$  are the *P-S* and *P-P* isochrons across the same depth interval, respectively. If the event correlations between the components are accurate, the dimensionless ratio  $V_p/V_s$  will be free of the effects of depth or thickness variations, as these will affect both components equally. Lateral variations in  $V_p/V_s$  may be interpreted as changes in lithology, porosity, pore fluid, and other formation characteristics (Tatham and McCormack, 1991).

Interpretation of the *P-P* and *P-S* sections for the central portion of line EKW-002 is shown in Figure 2.17. The *P-S* data are plotted at 2/3 the scale of the *P-P* data, and a robust correlation has been obtained between the two components.

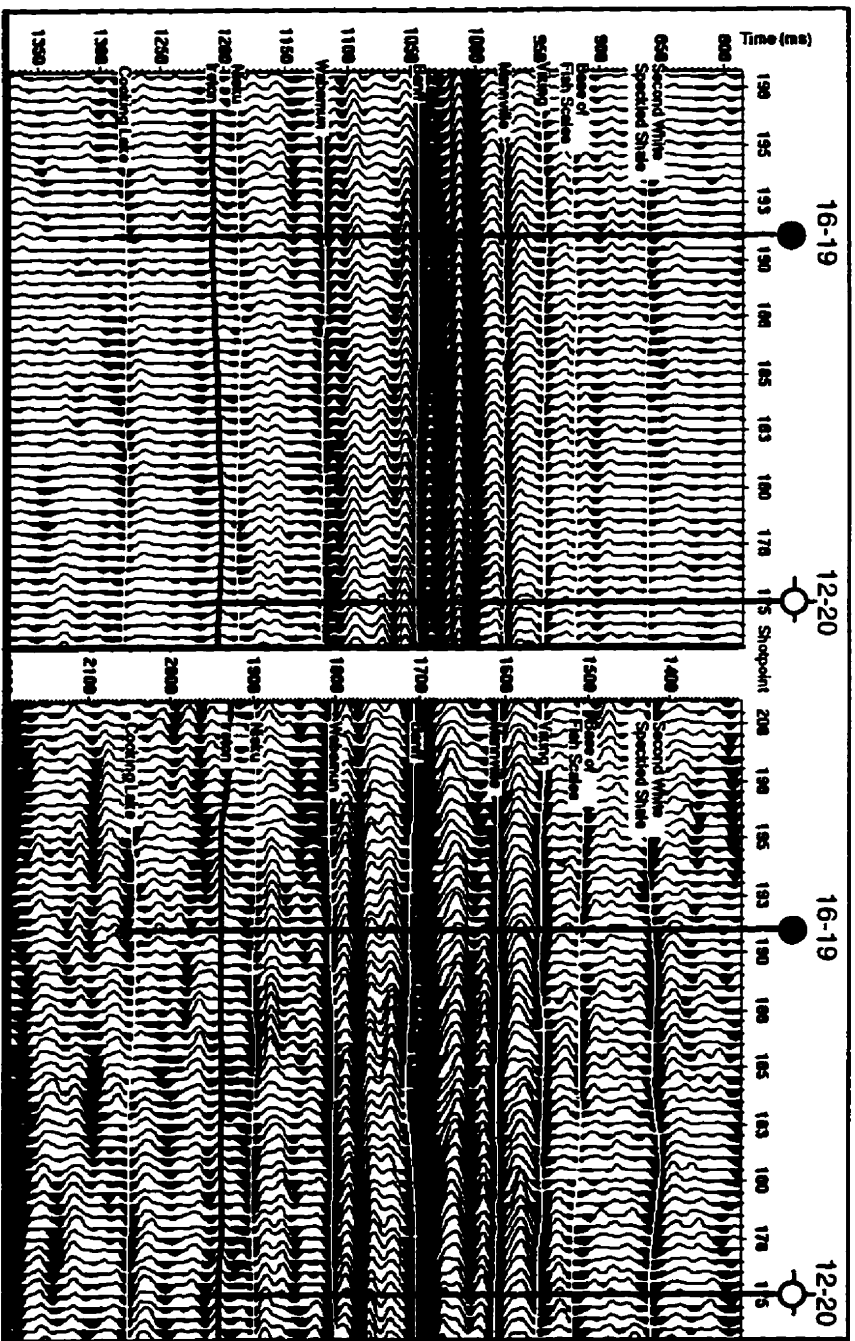


FIG. 2.17. Interpretation of the (a)  $P$ - $P$  data and (b)  $P$ - $S$  data is shown for part of Line EKW-002. The  $P$ - $S$  data are plotted at 2/3 the scale of the  $P$ - $P$  data. Although there is a good correlation between the two components, there are some differences in event character and amplitude.

Figure 2.18 illustrates how gross lithology is identifiable through  $V_p/V_s$  analysis. Along Line EKW-002,  $V_p/V_s$  was calculated for two different intervals. The upper curve is  $V_p/V_s$  for the portion of the Cretaceous section from the Second White Speckled Shale to the top of the Mannville Formation. This is a clastic section dominated by marine shales. High  $V_p/V_s$  values, averaging 2.26, are reasonable due to the high shale content and relatively shallow depth of burial. By contrast,  $V_p/V_s$  within a deeper carbonate section of Paleozoic rocks, from the Banff to the top of the Cooking Lake Formation, averages 1.85. This is within the expected range of 1.7 to 1.9 for competent carbonate rocks (e.g. Pickett, 1963; Rafavich et al., 1984; Wilkins et al., 1984).

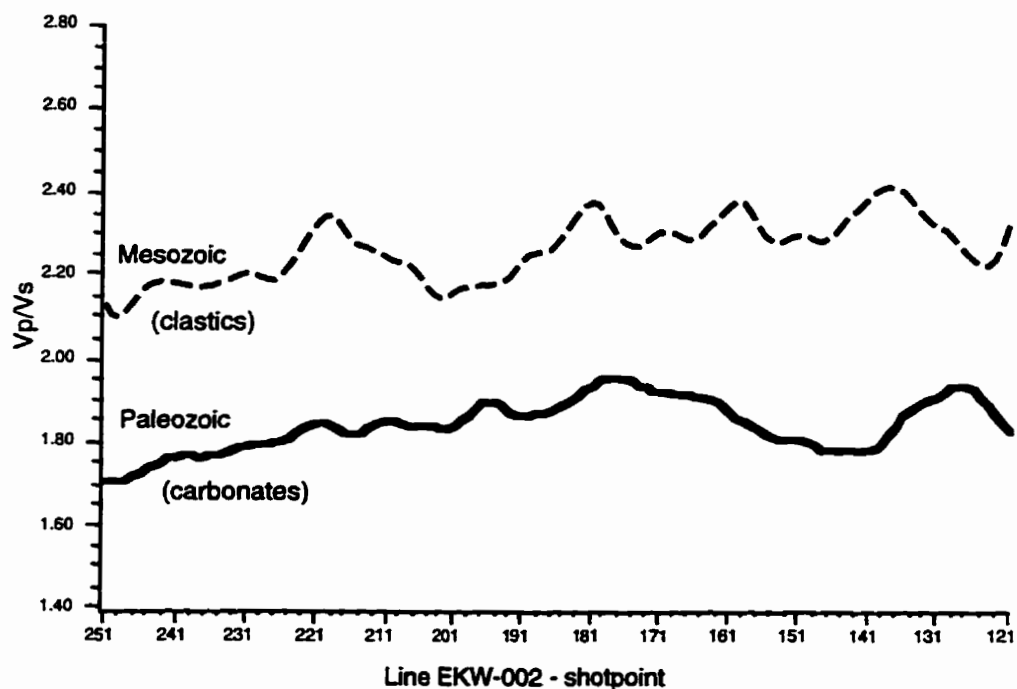


FIG. 2.18  $V_p/V_s$  values on Line EKW-002 for two intervals: Second White Specks to Mannville in the Cretaceous section of the Mesozoic and Banff to Cooking Lake in the Paleozoic. The Cretaceous interval is primarily shales and  $V_p/V_s$  averages 2.26, whereas the deeper Paleozoic section consists mainly of carbonate rocks and has an average  $V_p/V_s$  of 1.85.

The long wavelength  $V_p/V_s$  values reflect the bulk rock properties of the measured interval. However, frequently we are interested in short wavelength variations due to lateral changes in lithology or fluids within a particular formation. In this study, the objective was to use short-wavelength lateral variations in  $V_p/V_s$  to identify the transition from porous reservoir dolomite to tight basinal anhydrite within the Nisku Formation.  $V_p/V_s$  was calculated across a number of time intervals, each of which bracketed the Nisku

and could be identified on the seismic sections. The results for the Wabamun to Ireton and Banff to Ireton intervals on line EKW-002 are shown in Figure 2.19. The uncertainty bars on the curves were determined assuming an uncertainty of  $\pm 2$  ms on horizon picks and propagating that uncertainty through equation (1). For both intervals,  $V_p/V_s$  is lower at the oil wells (2-30 and 16-19) than it is along most of the line. The difference is greatest between the oil wells and the basinal anhydrite well (12-20). The anomaly is lower in magnitude for the Banff to Ireton interval ( $\sim 240$  m thick) than for the thicker Wabamun to Ireton interval ( $\sim 370$  m thick). This is due to the greater averaging effect when a longer time interval is used in the  $V_p/V_s$  analysis.

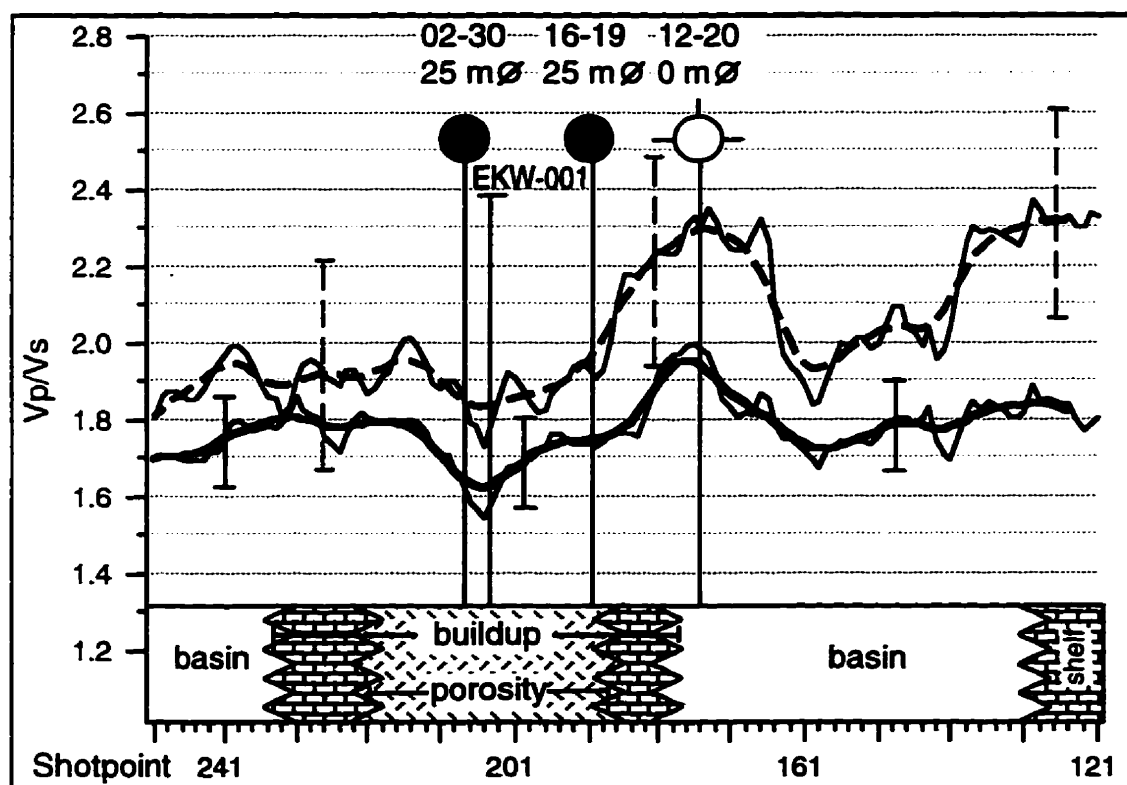


FIG. 2.19  $V_p/V_s$  values along Line EKW-002 for two intervals which bracket the Nisku reservoir: Banff to Ireton (solid) and the Wabamun to Ireton (dashed).

On line EKW-001, there is a  $V_p/V_s$  low at the 14-19 well location (Figure 2.20). This is a gas well with 17 m of porosity within the Nisku. Note that  $V_p/V_s$  is lower still at the intersection with line EKW-002, which occurs between the 2-30 and 16-19 wells, and thus is expected to have about 25 m of porosity at this location.

The results from this technique indicate an decrease in  $V_p/V_s$  associated with the transition from tight basinal rocks to porous reservoir dolomites. Low values of  $V_p/V_s$  correlate well to porosity within the reservoir, but the transition between tight carbonate and anhydrite is more difficult to define. The divisions between buildup, basin and shelf shown on the graphs are based on sparse well control, so the locations of the buildup and shelf edges are not known precisely. Based on this analysis, multicomponent seismic data can be used effectively to map porosity within the Nisku reservoir.

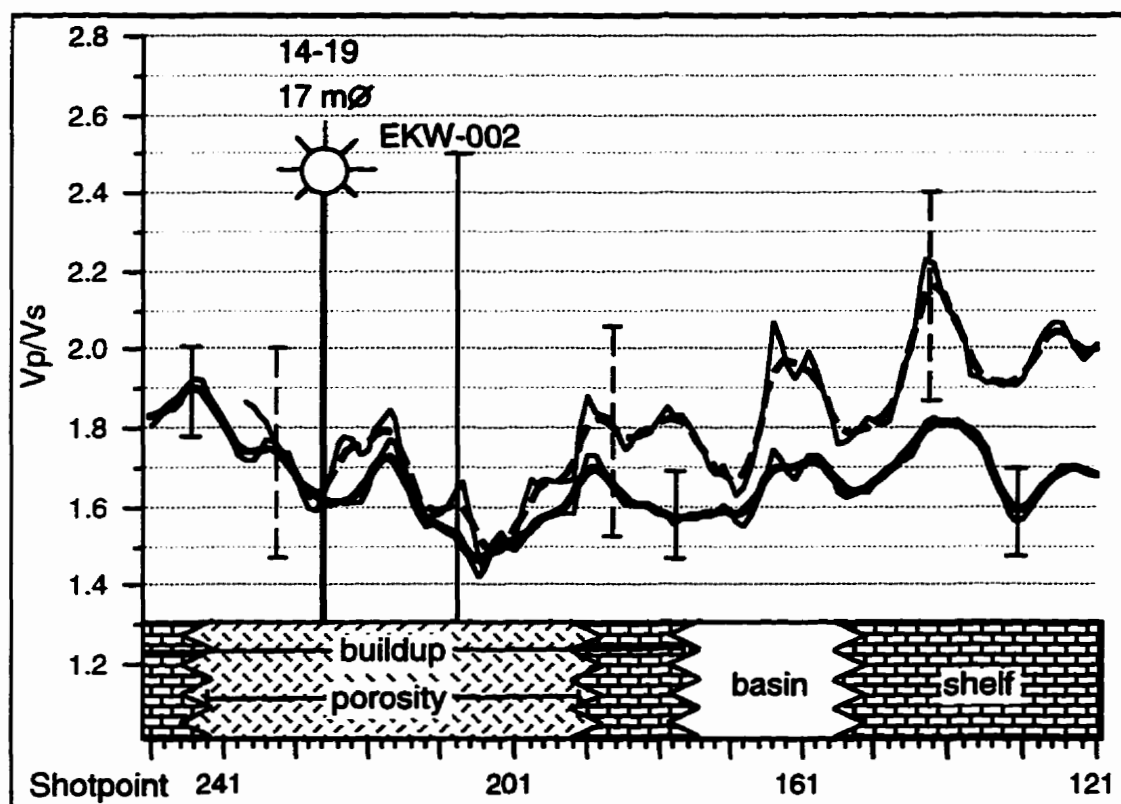


FIG. 2.20  $V_p/V_s$  values along Line EKW-001 for the same intervals shown in Figure 12. There is a relative  $V_p/V_s$  low at the 14-19 well, which has 17 m of porosity within the Nisku.  $V_p/V_s$  is lowest near the intersection with Line EKW-002, where about 25 m of porosity is expected.



## 2.4 Numerical seismic modelling

Modelling studies were performed to assist data interpretation, particularly for the Nisku interval. There were two specific objectives for the modelling studies. In the first part, well logs were edited to simulate different conditions in the zone of interest in order to predict the  $P$ - $P$  and  $P$ - $S$  seismic response. These models were also used to test  $V_p/V_s$  analysis over various isochron intervals and determine the ability of this technique to resolve lithology variations in the reservoir zone. The second part describes forward modelling from well logs to determine the effect of intrabed multiples and local conversions. These models support the hypothesis that the mis-ties described in section 2.3.1 are due to multiple interference. The  $P$ - $S$  models are less damaged by multiples at the zone of interest and thus illustrate a further benefit of multicomponent recording

### 2.4.1 Forward $P$ - $P$ and $P$ - $S$ Modelling

Well log curves were modified to simulate a variety of geologic conditions in the Nisku formation. The initial  $P$ -wave sonic curve was from the 12-20-36-24W4 well which is on line EKW-002 (SP 175) and tied the  $P$ -wave seismic data quite well. The 12-20 well is in the basin with anhydrite at the Nisku level. This well only penetrated to the Ireton Formation, and so a composite curve was made using the 16-19-36-24W5 sonic log from the Ireton to the base at the Beaverhill Lake Formation. Since there was no density log available, the density log from 8-20-36-24W5 was edited to match the 12-20 depths. The  $S$ -wave log was derived from the  $P$ -wave log and interval  $V_p/V_s$  values appropriate for particular lithologies. The values in Table 2 were used in the Nisku Formation to simulate anhydrite, tight limestone, tight dolomite, and dolomite with 10% porosity, both oil-filled and gas-filled. The values were obtained from well logs from the Lousana field, the Mobil Davey well at 3-13-34-29W4, literature values (Schlumberger, 1989), and petrophysical relationships such as the time average equation (Wyllie et al., 1956). The Nisku porosity is primarily vuggy, so the Kuster-Toksöz (1974) models of Robertson (1987) for rounded pores in dolomite were used to estimate the variation in  $V_p/V_s$  with porosity and pore fluid. The logs, shown in Figure 2.21 and 2.22, are identical outside the Nisku Formation.

Table 2.2 Rock property values used for numerical models.

	$\Delta t_p$ [ $\mu\text{s}/\text{m}$ ]	$\Delta t_s$ [ $\mu\text{s}/\text{m}$ ]	$V_p/V_s$	density [ $\text{kg}/\text{m}^3$ ]
Anhydrite	164	328	2.00	2960
Tight limestone	154	295	1.90	2700
Tight dolomite	141	253	1.80	2850
Dolomite: 10% porosity - oil filled	187	328	1.75	2650
Dolomite: 10% porosity - gas filled	213	328	1.55	2560

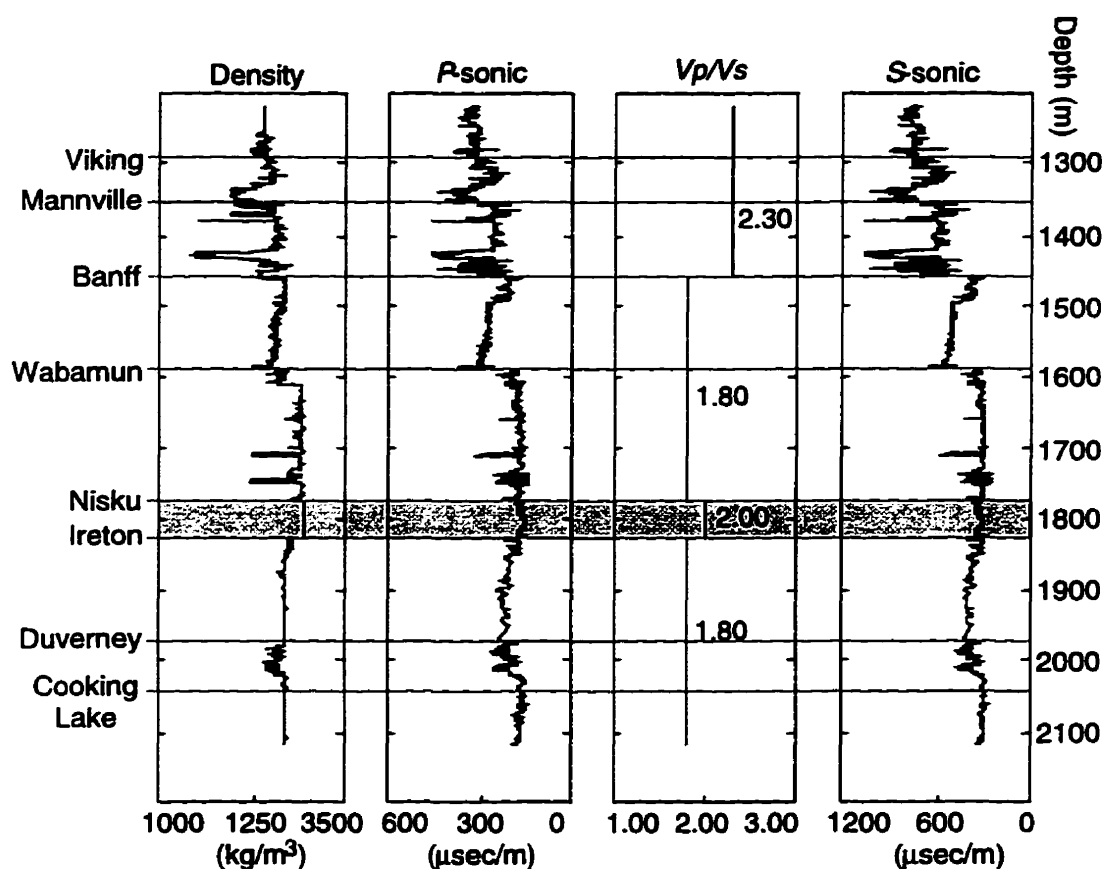


FIG. 2.21 Well log curves used to model  $P$ - $P$  and  $P$ - $S$  response of the anhydrite basin. Interval  $V_p/V_s$  curves are based on literature values for the known lithologies and used, together with the  $P$ -sonic curve, to generate the  $S$ -sonic curves. The curves are identical outside the Nisku Formation.

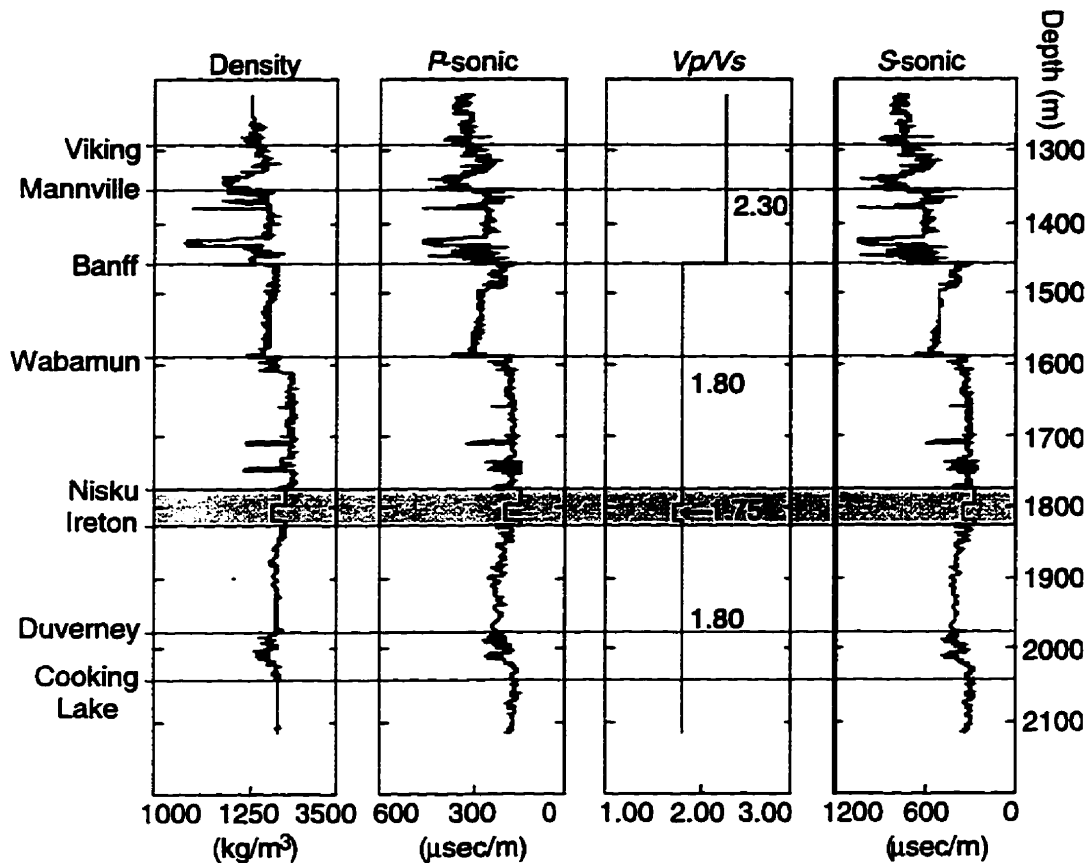


FIG. 2.22 Well log curves used to model  $P$ - $P$  and  $P$ - $S$  response of the dolomite buildup.

The Nisku interval is 50 m thick, from 1776-1826 m below the kelly bushing. Two porosity thicknesses were simulated: 23 m from 1798-1821 m, the thickness found in the 16-19 well, and 38 m from 1783-1821 m. All the logs are identical outside of the Nisku Formation.

The  $P$ - $P$  model consisted of 25 receivers with 66 m spacing, with a far offset of 1584 m. Because of phase changes at far offsets due to critical incidence for some models, the spread length was reduced for the  $P$ - $SV$  model to 22 receivers at 66 m spacing for a far offset of 1386 m. A 40 Hz zero-phase Ricker wavelet was used for the  $P$ - $P$  model and a 25 Hz zero-phase Ricker for the  $P$ - $S$  model, matching dominant frequencies and bandwidths determined from the processed multicomponent data. Only primary events are included in the models. The offset synthetic stacks are shown for the  $P$ - $P$  case in Figure 2.23 and the  $P$ - $S$  case in Figure 2.24. Both components exhibit changes at the Nisku level with changes in lithology, porosity, and pore fluid. When porosity is introduced, a trough followed by a peak develops below the peak at the top of the Nisku, indicating porosity and

the base of porosity respectively. The amplitude of this lower peak brightens either by thickening the porosity from 23 m to 38 m or by the replacement of oil with gas. The modelled  $P$ - $P$  response is similar for anhydrite and tight limestone: a tight doublet. A slight difference in the character of the doublet is evident on the  $P$ - $SV$  model. In tight dolomite a single broad peak/trough pair is evident on both models.

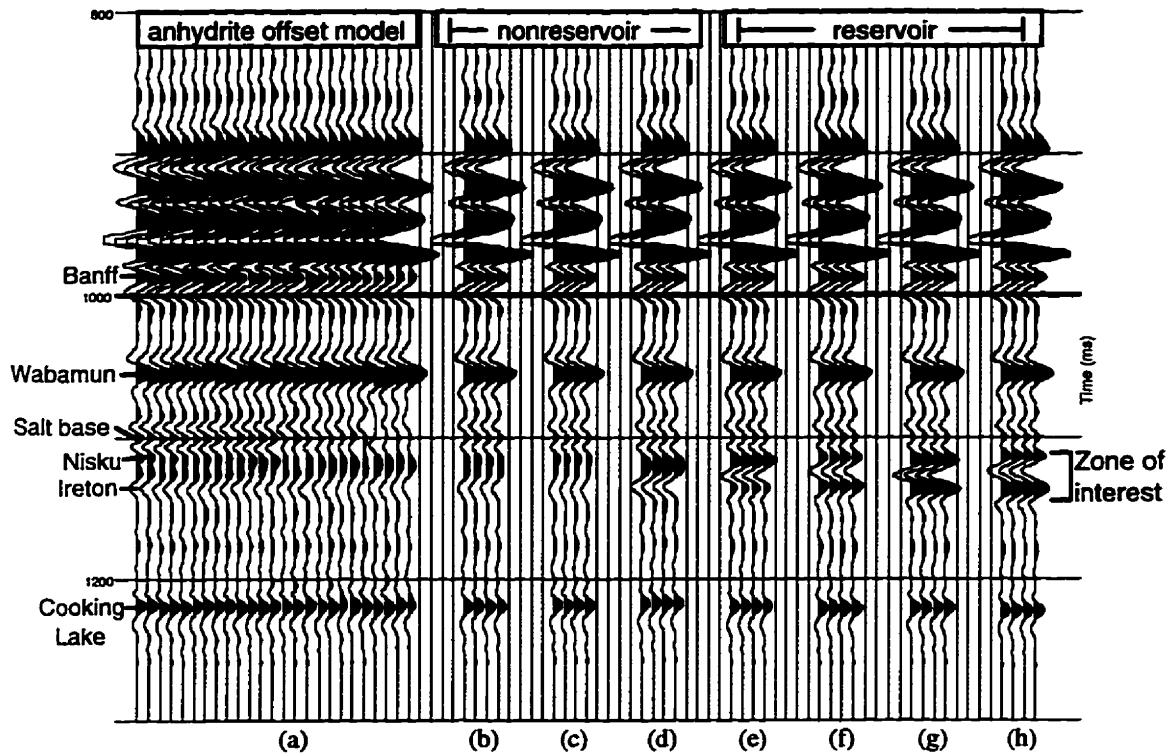


FIG. 2.23  $P$ - $P$  model results showing (a) offset synthetic seismogram for anhydrite, and offset synthetic stacks for (b) anhydrite; (c) tight limestone; (d) tight dolomite; (e) 23 m oil-filled porous dolomite; (f) 38 m oil-filled porous dolomite; (g) 23 m gas-filled porous dolomite; (h) 38 m gas-filled porous dolomite.

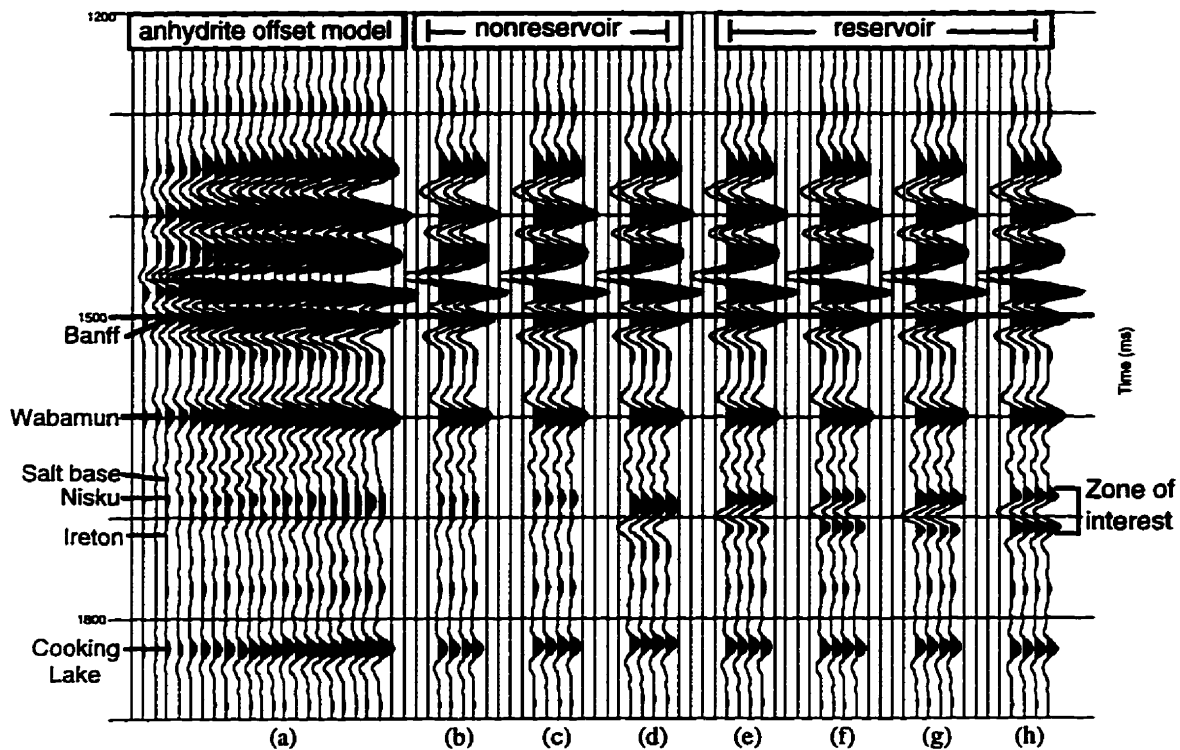


FIG. 2.24  $P$ - $S$  model results showing (a) offset synthetic seismogram for anhydrite, and offset synthetic stacks for (b) anhydrite; (c) tight limestone; (d) tight dolomite; (e) 23 m oil-filled porous dolomite; (f) 38 m oil-filled porous dolomite; (g) 23 m gas-filled porous dolomite; (h) 38 m gas-filled porous dolomite.

Horizons were identified on  $P$ - $P$  and  $P$ - $SV$  synthetic seismograms by picking maximum amplitudes, and  $P$ - $P$  and  $P$ - $SV$  isochrons were used to calculate  $V_p/V_s$  across several time intervals for each stack, using equation (1). Horizons were chosen which bracketed the Nisku and which could be readily identified on the processed field data. The logs are identical outside of the Nisku Formation, so variations in  $V_p/V_s$  are due solely to changes within the Nisku. Figure 2.25 shows  $V_p/V_s$  variations across six intervals with the following thicknesses:

Banff - Cooking Lake:	581 m
Wabamun - Cooking Lake:	452 m
Wabamun salt marker - Cooking Lake:	328 m
Banff - Ireton trough:	366 m
Wabamun - Ireton trough:	237 m
Wabamun salt marker - Ireton trough:	113 m

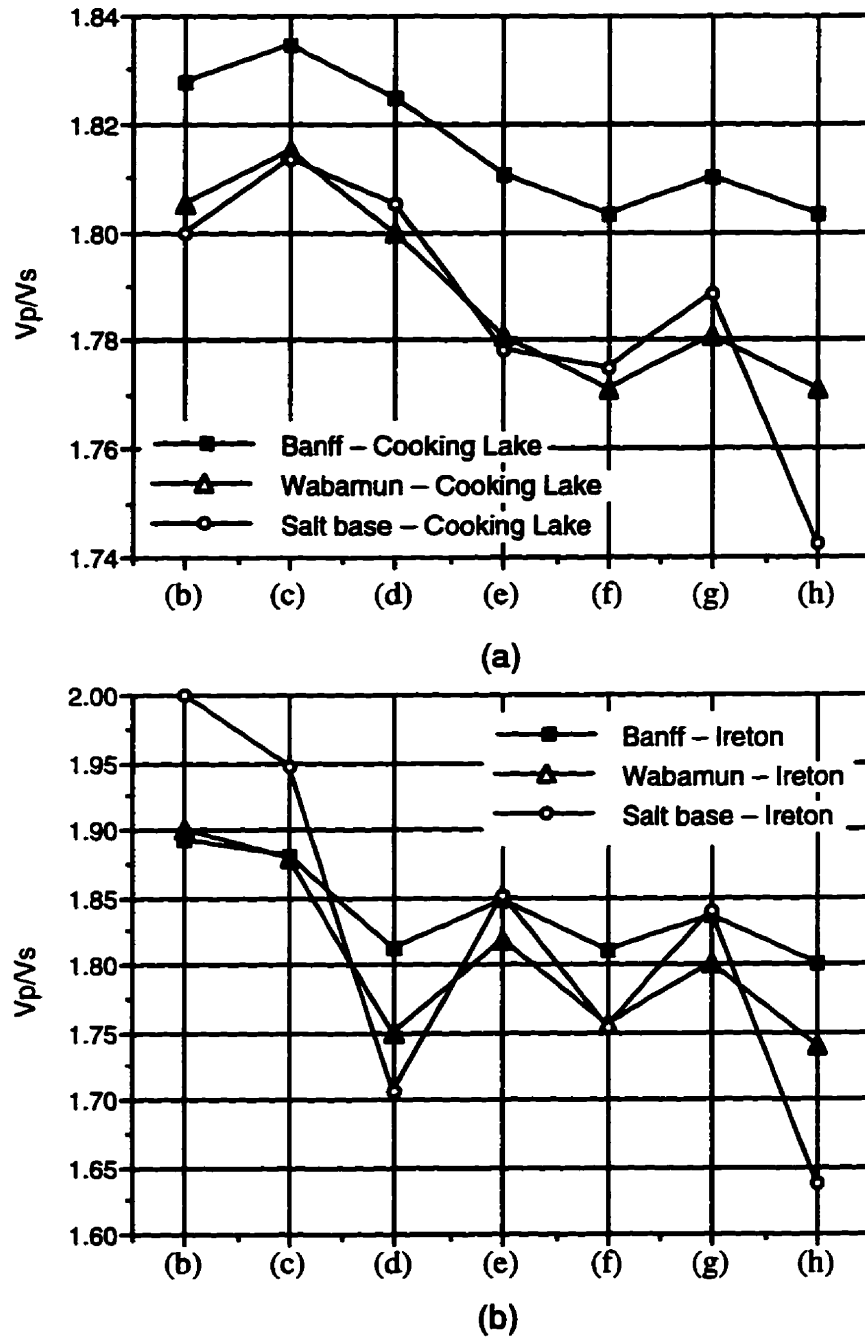


FIG. 2.25 Plot of  $V_p/V_s$  measured across intervals on the model data in Figures 2.23 & 2.24 with (a) Cooking Lake as the lower horizon and (b) the Ireton as the lower horizon. The upper horizons are the Banff, Wabamun, and Wabamun salt marker (Salt). The Nisku simulates (b) anhydrite; (c) tight limestone; (d) tight dolomite; (e) 23 m oil-filled porous dolomite; (f) 38 m oil-filled porous dolomite; (g) 23 m gas-filled porous dolomite; (h) 38 m gas-filled porous dolomite.

There are several observations to note from Figure 2.25.  $V_p/V_s$  varies with lithology, porosity, and pore fluid, with the degree of variation diminishing as the

thickness of the interval increases. The general trend is for  $V_p/V_s$  to decrease from (b) to (h) as the model changes from nonreservoir rocks to reservoir rocks. Thickening the porous zone from 23 m to 38 m decreases  $V_p/V_s$  more than when oil is replaced by gas. If one of the bounding horizons is too close to the zone of interest, wavelet interference from that zone may affect the picks and cause erroneous results. This is probably the case for the sharp decrease in  $V_p/V_s$  which occurs for tight dolomite when the lower horizon is the top Ireton pick, which underlies the Nisku. This may also be the cause of the increase in  $V_p/V_s$  across the Wabamun salt to Cooking Lake interval when gas replaces oil, with a 23 m porous interval. Using this salt as the top marker and the Ireton as the base marker produces the thinnest interval and thus the largest variations in  $V_p/V_s$ . However, in this case, the values may be in error due to wavelet interference.

Interpretation experience suggests that changes of  $\pm 0.05$  in interval  $V_p/V_s$  can be detected through careful visual inspection of synthetic seismograms and stacked seismic sections. The intervals which use the Ireton as the lower bounding horizon show at least this much change between the anhydrite and 23 m of porous dolomite (as occurs in the oil wells). This suggests that the difference may be detectable, although possible wavelet interference from the Nisku event must be considered. The greatest contrast for all intervals occurs between tight anhydrite or limestone and the 38 m thick gas-filled porous dolomite. This effect might be observable in an oil reservoir if the gas-to-oil ratio is high enough, as gas saturation as low as 5-10% will result in a sharp decrease in  $V_p/V_s$  (Gregory, 1977).

$V_p/V_s$  is significantly lower for both intervals when the zone of interest is porous dolomite than when it is tight anhydrite (Figure 2.25). The difference in  $V_p/V_s$  between anhydrite and 23 m of porous dolomite is 0.05 for the Banff to Ireton interval and 0.08 for the Wabamun to Ireton interval. In the computation,  $V_p/V_s$  is calculated over the entire interval, so that the contrast in  $V_p/V_s$  is greater when the Nisku comprises a greater proportion of the interval. The Banff to Ireton interval (366 m) is 1.54 times thicker than the Wabamun to Ireton interval (237 m). The  $V_p/V_s$  contrast (between dolomite and anhydrite) is 1.60 times greater for the smaller Wabamun to Ireton interval. The modelling results indicate that  $V_p/V_s$  analysis is applicable in carbonate settings, even when the reservoir intervals are relatively thin (23 m) and comprise only 15-20% of the total measured interval.

The modelling trend is in agreement with the analyses of the processed field data. In each case,  $V_p/V_s$  is lower across intervals which contain dolomite reservoir in the Nisku

than intervals where the Nisku is tight anhydrite.  $V_p/V_s$  curves from the data are not identical to those from the model, possibly due to lateral geological variations within the measured intervals but outside the target zone.

## 2.4.2 Models with multiples and local conversions

As previously noted, the  $P$ -wave seismic data ties the  $P$ -wave synthetic seismogram very well down to the top of the Banff (Figure 2.13). However, there are mis-ties later than this at the Wabamun, Nisku, and Cooking Lake events. The mis-ties occur in the zone of interest and have complicated the travel-time analysis of the Lousana data, including the  $V_p/V_s$  analysis. Thus far, these mis-ties have been assumed to be due to interference from intrabed multiples, most likely originating within the Mannville coals. To confirm this hypothesis, the data have been modelled using an offset modelling algorithm which can include intrabed multiples, intrabed conversions, or both.  $P$ - $S$  models were also run to compare the predicted effect of intrabed multiples between the different propagation modes.

The modelling package used is based on an algorithm which is a hybrid of ray-trace methods and wave reflectivity theory (C. Frasier, pers. comm., 1995). The algorithm can calculate all intrabed multiples and intrabed conversions within a target zone which is user specified. For both wells a target zone was chosen which started above the Mannville coals and ended in the Ireton Formation: 1285 -1840 m for 16-19 and 1290 -1860 m for 12-20. The geometry used was 25 receivers from 0 to 1524 m for a receiver spacing of about 60 m. As currently implemented, this program will zero any traces which contains reflections which exceed critical incidence. A 40 Hz Ricker wavelet was used for the  $P$ - $P$  models and a 25 Hz Ricker wavelet for the  $P$ - $S$  models. All the models have been corrected for normal moveout.

### 2.4.2.1 $P$ - $P$ models with multiples and local conversions

The input data were blocked  $P$ -sonic and density logs from the 16-19 and 12-20 wells, which are both situated on line EKW-002. The primaries-only  $P$ - $P$  offset model from 16-19 is shown in Figure 2.26(a). The same model was then run with primaries plus all intrabed multiples (Figure 2.26(b)), primaries plus all conversions (Figure 2.26(c)), and primaries plus all intrabed multiples and conversions (Figure 2.26(d)).



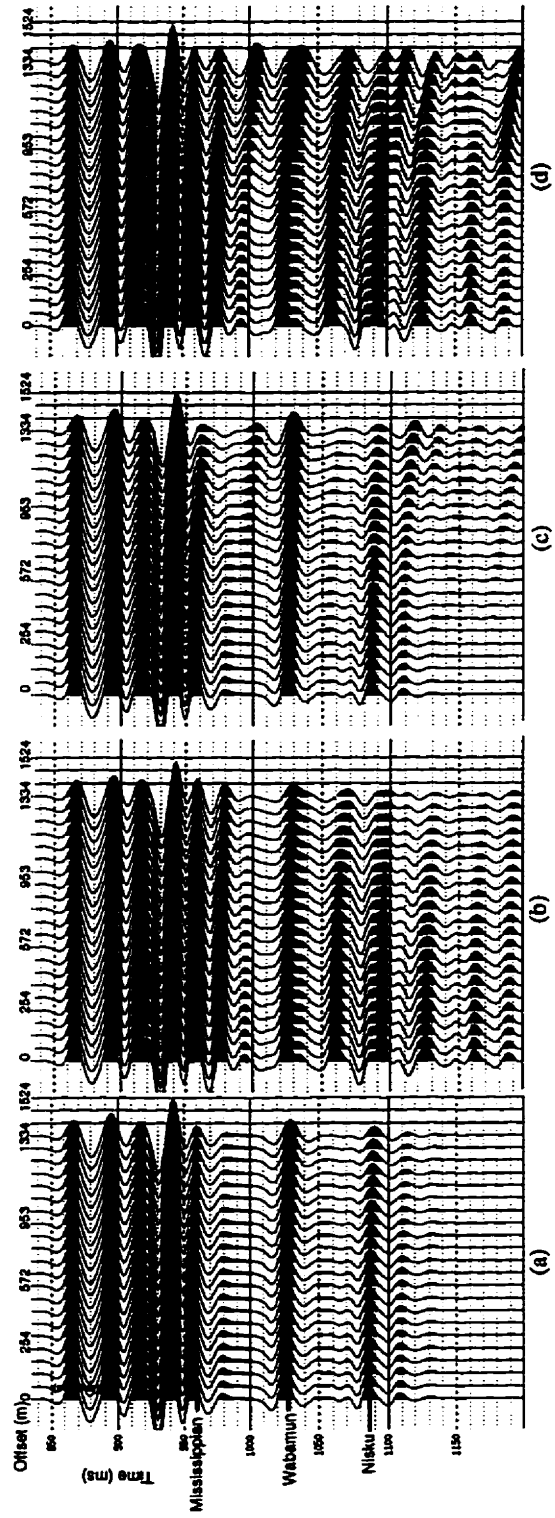


Fig. 2.26. The  $P$ - $P$  offset model from the 16-19  $P$ -sonic and density logs with (a) primaries-only, (b) primaries plus all intrabed multiples, (c) primaries plus all conversions, and (d) primaries plus all intrabed multiples and conversions.

The effects of including all intrabed multiples, primarily evident after the Banff event, include:

- the subtle peak immediately after the Banff event (980 ms) shows a significant increase in amplitude,
- the character of the Wabamun event changes; it is more difficult to pick the top,
- additional events appear at 995 and 1060 ms (zero-offset time),
- the trough before the Nisku event is much higher amplitude,
- the Nisku event changes character; it becomes a double peak and the porosity trough and base of porosity lower peak are no longer easily discernible (1100 and 1110 ms on the primaries-only model), and,
- the Nisku event is delayed.

The principal effect of including local conversions in the calculations is the residual moveout on events with increasing offset; it is especially evident on the Nisku event. Undercorrected mode-converted events also occur later in the record. The far offset traces will degrade the stack and cause smearing of events. When all intrabed multiples and local conversions are included in the model, all these effects are superposed and result in a record (Figure 2.26(d)) which is considerably different in character and event timing than the primaries-only record (Figure 2.26(a)).

In order to better understand the source of the intrabed multiple interference, the target zone was progressively thinned from the top. The output seismograms suggested that the primary source of multiple interference is from the low-velocity coal beds in the Upper Mannville.

A comparison of Ormsby, Ricker, statistically extracted and sonic log extracted wavelets demonstrated that the statistically-extracted wavelet and the 40 Hz Ricker are very similar and best match the seismic section. The stacked seismogram with the 40 Hz Ricker wavelet is spliced onto the *P-P* seismic line at the 16-19 well location in Figure 2.27. This seismogram contains intrabed multiples and local conversions. As mentioned in section 2.3.1, the input well log was not stretched below the Banff event. Thus there is still a residual time mis-tie, but it has been reduced from 10 ms to 5 ms for the Banff to Nisku interval (the synthetic seismogram in Figure 2.27 has been aligned to match at the Nisku). The high amplitude peak just after the Banff event on the seismogram also appears in the data. The Wabamun has less reverberation on the seismogram than on the data, but there is a good character match at the central event; the character match is also good at the Nisku.

This seismogram, containing intrabed multiples and local conversions, matches the data better than the primaries-only seismogram shown in Figure 2.11. This supports the hypothesis that mis-ties between synthetic models and the  $P$ - $P$  seismic data are due to short-path multiple interference.

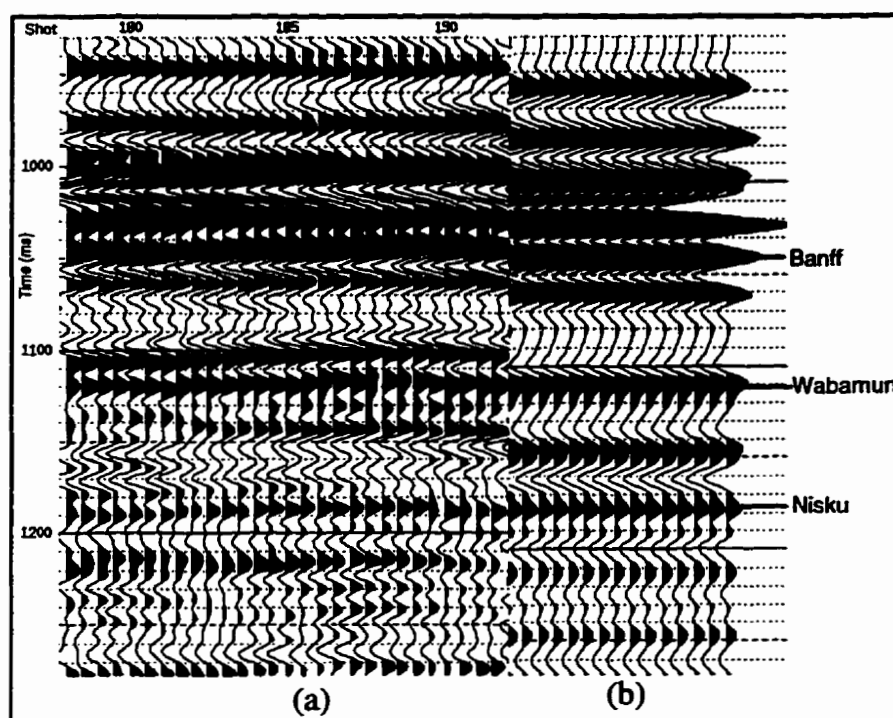


Fig. 2.27 The  $P$ - $P$  offset synthetic stack with all intrabed multiples and conversions is spliced onto the  $P$ - $P$  seismic line at the 16-19 well location.

#### 2.4.2.2 Comparison of models from 16-19 and 12-20 wells

The full-elastic wave modelling results have important implications for  $V_p/V_s$  analysis. This procedure incorporates  $P$ - $P$  isochrons, which will be altered if multiple interference is causing events to have an apparent time delay. Since the goal of this analysis is primarily to detect lateral variations in  $V_p/V_s$ , the modelling was repeated at the 12-20 well to see if a comparable delay was observed on seismic events. Figure 2.28a shows the 16-19 stacked synthetic seismogram with primaries only on the left, and all intrabed multiples and conversions included on the right. The top line shows the correct Nisku pick from the primaries-only model, and the lower line is the pick made on the model with multiples and conversions. The inclusion of multiples and conversions delays the pick by 10 ms. In Figure 2.28b, the 12-20 well is modelled without intrabed multiples and

conversions (left) and including them (right). The Nisku pick on the left uses the well log top and is correct, whereas the pick on the right is the peak amplitude of the Nisku event. Again, there is a 10 ms delay between the two. This suggests that multiple interference may introduce a systematic error to the  $V_p/V_s$  analysis. Although this will affect absolute values, lateral variations in  $V_p/V_s$  will remain intact, provided that the delay on the picked horizon is laterally constant.

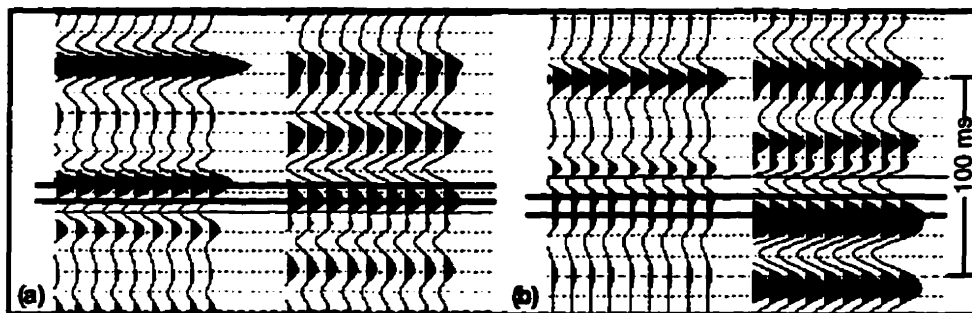


Fig. 2.28 (a) The 16-19 stacked synthetic seismogram with primaries only on the left, and all intrabed multiples and conversions included on the right. (b) The 12-20 stacked synthetic seismogram with primaries only on the left, and all intrabed multiples and conversions included on the right. The bold lines indicate the Nisku picks, which have been delayed by multiple interference by about 10 ms for both wells.

#### 2.4.2.3 *P-S* models with multiples

The input data for the *P-S* models were the *S*-sonic log and density log from the 16-19 well. The *S*-sonic log was created using the *P*-sonic log and a  $V_p/V_s$  of 2.25 above the Mississippian unconformity and 1.80 below, which are reasonable average values from  $V_p/V_s$  analysis. The data are from the horizontal component of the receiver. The stack of the primaries-only model with all conversions is shown in Figure 2.29. The ties at the Banff and Nisku are quite good, with a slight mis-tie at the Wabamun. The seismic data shows an event just above the Wabamun at 1775 ms which does not match the synthetic seismogram.

The stack of the *P-S* model with primaries and all intrabed multiples is shown in Figure 2.30. The ties at the Banff and the Nisku horizons are still good; the Nisku event has not been delayed by multiple interference. The Wabamun tie is slightly improved, and the event at 1775 ms on the data is now evident on the synthetic seismogram. Based on the modelling results, intrabed multiples have less effect on the Nisku arrival on the *P-S* data than on the *P-P* data.

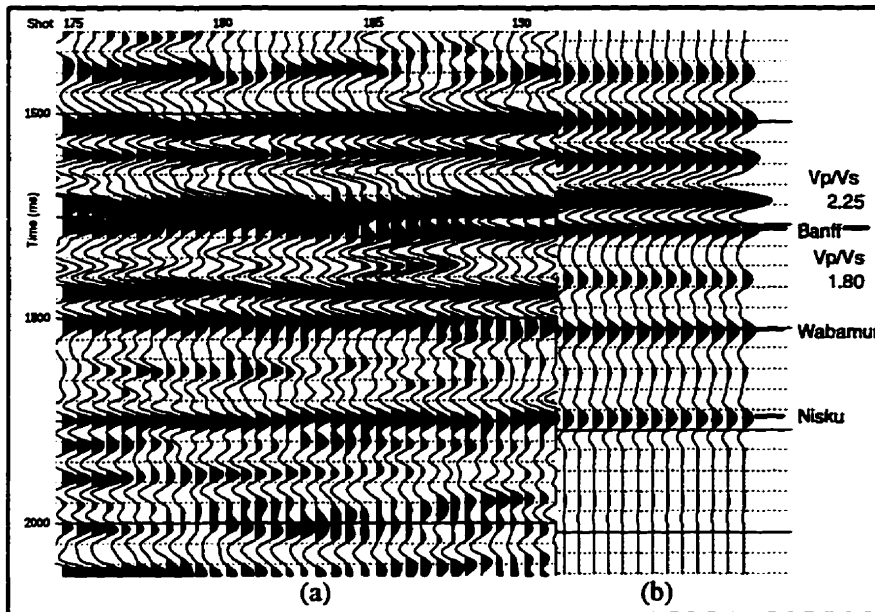


FIG. 2.29 (a) The *P-S* seismic data from line EKW-002 is tied to (b) the *P-S* offset synthetic stack, with primaries only, from 16-19 at the well location. The ties at the Banff and Nisku are quite good, with a slight mis-tie at the Wabamun.

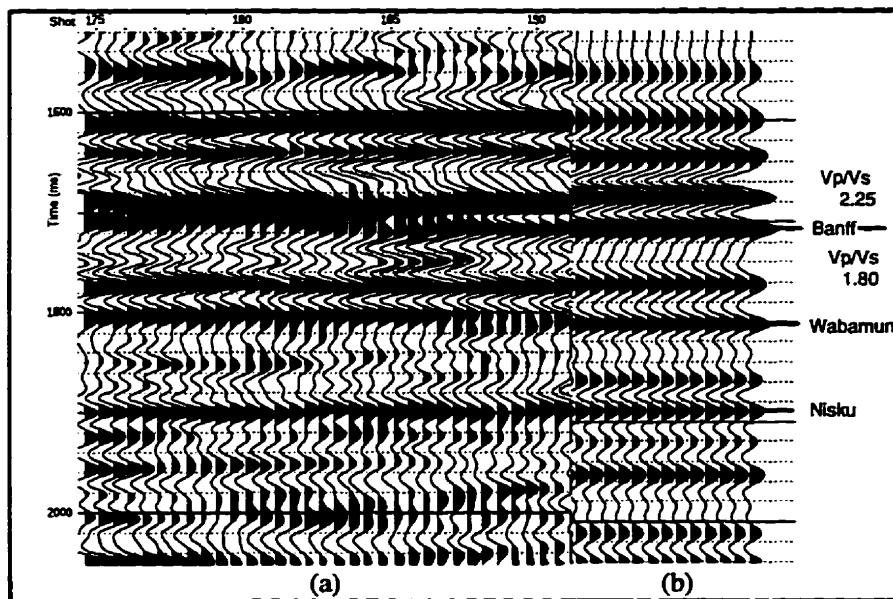


FIG. 2.30 (a) The *P-S* seismic data from line EKW-002 is tied to (b) the *P-S* offset synthetic stack, with primaries and all intrabed multiples, from 16-19 at the well location. The ties at the Banff and Nisku are still good, and the tie at the Wabamun is improved.

## 2.5 Discussion

The Lousana multicomponent data are of overall good quality and the *P-P* and *P-S* seismic sections were correlated with a high degree of confidence. Iterative matching of *P-S* synthetic seismograms to *P-S* seismic data is a useful technique for extracting interval  $V_p/V_s$  values at the well location in areas where full-waveform sonic logs are unavailable. Carrying out this procedure at both an oil well and a dry hole demonstrated that  $V_p/V_s$  is lower across an interval containing porous dolomite buildup than one containing anhydrite.

The carbonate reservoir at Lousana is difficult to detect using conventional seismic techniques. Through multicomponent analysis,  $V_p/V_s$  profiles were derived which showed a correlation between a decrease in  $V_p/V_s$  and oil well locations. Numerical modelling supports the observation that  $V_p/V_s$  is lower in porous dolomite than tight anhydrite, and that this difference is detectable on seismic data. Thus, the application of multicomponent seismic methods in this area provides a useful means of delineating prospects. This dataset was also used to illustrate how long wavelength  $V_p/V_s$  values can be used to identify bulk rock properties. The average  $V_p/V_s$  for Mesozoic was 22% higher than that of Paleozoic carbonates.

The results from numerical modelling of intrabed multiples support the hypothesis that multiple interference is degrading the seismic data from this area. In the case of the *P-P* data, one of the effects of the multiple reflections is the delay of the Nisku event. The *P-S* synthetic models do not show this delay, thus the Nisku event on the *P-S* seismic data appears to be less contaminated by intrabed multiple interference than the *P-P* seismic data. This suggests that the *P-S* seismic section is more robust, and that  $V_p/V_s$  values derived from well data and the *P-S* section, as described in section 2.3.2, may be more reliable than those derived from the isochron analysis described in section 2.3.3. However, it should be noted that no *S*-sonic well logs were available, and the multiple models were run using *S*-sonic logs derived from simplified average interval  $V_p/V_s$  values.

Since  $V_p/V_s$  isochron analysis uses the horizon picks from both the *P-P* and the *P-S* seismic sections, the absolute values of  $V_p/V_s$  obtained from this method will be inaccurate if either of the isochrons is incorrect. In this case, multiple interference appears to delay the Nisku (and thus subsequent) events on the *P-P* section. This will result in  $V_p/V_s$  values which are lower than in the multiple-free case. Modelling of both the 16-19 and the 12-20 wells shows an equal time delay, suggesting that the effect is laterally

consistent. Thus, although absolute  $V_p/V_s$  values may be too low, the lateral variations in  $V_p/V_s$  may still be indicative of lateral geological changes.

In summary, the seismic interpretation and the numerical modelling results support the use of multicomponent seismic for this type of play because firstly, relative  $V_p/V_s$  lows correlate with porous dolomitic locations, and, secondly, multiple contamination in the zone of interest is less severe on the  $P$ - $S$  seismic data.

## **Chapter 3 – Blackfoot Case History**

### **3.1 Geology of the Blackfoot Field**

A simplified chart of the stratigraphy of the study area is shown in Figure 3.1. The target rocks are incised valley-fill sediments within the Glauconitic Formation, a member of the Upper Mannville Group of Early Cretaceous (Albian) age. Numerous Glauconitic incised valleys are present in southern Alberta, generally trending in a northwesterly direction. These range from major valley systems, which can be correlated regionally, to small valleys and channel systems which were influenced by local fluctuations in relative sea-level. These incised valleys cut to varying depths through the underlying strata and thus the bases may be found directly over or within any one of the Ostracod, Sunburst, or Detrital Formations. Within the study area, the Mannville Group unconformably overlies the Mississippian carbonates of the Shunda Formation. The Paleozoic erosional surface has an irregular topography and, as the Shunda is shalier up-section, cuts into varying lithologies. The role of the antecedent Mississippian topography in influencing the location of Glauconitic valleys is uncertain. In general, the topographic relief of the unconformity surface seems to have been compensated by the time of deposition of the Glauconitic sediments (A. Politylo, pers.comm., 1995).

Fluvial and estuarine Glauconitic sediments were deposited during the maximum transgression of the boreal Moosebar/Clearwater Sea from the north and during the early stages of the subsequent regression. The Glauconitic Member consists of very fine to medium grained quartz sandstone in the eastern part of Alberta, and glauconite is commonly present northwards of central Alberta. In southern Alberta, the Glauconitic progradational deltaic sequence caps the brackish bay sediments of the Ostracod Formation. The Ostracod beds underlying the Glauconitic are made up of brackish water shales, argillaceous, fossiliferous limestones and thin quartz sandstones and siltstones (Layer et al., 1949). The thin, low velocity Bantry Shale Member underlies the Ostracod but is not laterally persistent (Coveney, 1960). The Sunburst Member contains ribbon and sheet sandstones made up of sub-litharenites and quartzarenites. The Detrital Beds make up the basal part of the Mannville Group. This formation has a highly heterogeneous lithology containing chert pebbles, lithic sandstone, siltstone and abundant shale. Its distribution and thickness is largely controlled by the topography of the pre-Cretaceous erosional surface and is thus highly variable over short distances (Badgley, 1952).



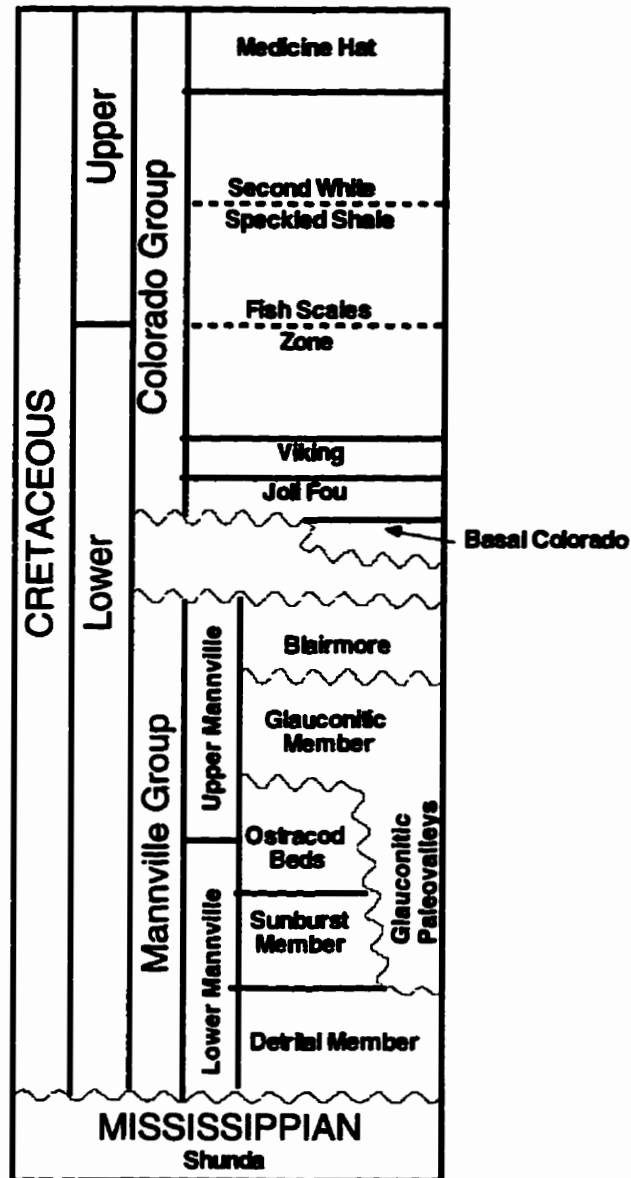


Figure 3.1 Stratigraphic sequence near the zone of interest. (Modified from Leckie et al., 1994, and Wood and Hopkins, 1992).

The Blackfoot Field is located about 15 km southeast of the town of Strathmore, Alberta, in Township 23, Range 23, West of the 4th Meridian. In this area, the Glauconitic sandstone is encountered at a depth of approximately 1550 m and the valley-fill sediments vary from 0 m to over 35 m in thickness (Layer et al., 1949). According to A. Politylo (pers. comm., 1995), the Glauconitic Member is subdivided into three units corresponding to three phases of valley incision; all three cuts may not be present everywhere. The lower and upper members are made up of quartz sandstones with an average porosity of approximately 18%, while the middle member is a tight lithic sandstone. The individual

members range in thickness from 5-20 m. Hydrocarbon reservoirs are found in structural and stratigraphic traps where porous channel sands pinch out against non-reservoir regional strata or low-porosity channel sediments. The primary hydrocarbon at the Blackfoot Field is oil, although gas may also be present in the upper member.

## 3.2 Objectives

A 3C-2D seismic line over the Blackfoot Field was acquired by the CREWES Project in 1995. It crosses Glauconitic incised valley fills as shown in Figure 3.2. This map is an isopach of sediment thickness based on known well control at the time of survey acquisition as well as the interpretation of a conventional 3-D seismic survey; it indicates gross thickness of the channel fills but no lithologic distinctions (A. Politylo, pers. comm., 1995). The channel shales out in some locations, such as at the 12-16 well.

The exploration challenge in this area is to distinguish between sandstone and shale facies. Low-velocity shales have a similar acoustic impedance to low-velocity porous sandstones. Thus it is difficult to distinguish between the two lithologies on conventional *P-P* seismic data. Because of the well-documented association between increasing  $V_p/V_s$  and increasing shale within siliclastics (described in Chapter 1.1), a 3-C survey was undertaken. The two primary objectives of this work were to use the analysis of the 3-C seismic data to: 1) distinguish channel from regional facies, and, 2) determine sand/shale ratios within the valley system.

The main emphasis of this work is on the interpretation and modelling of the Blackfoot multicomponent data set. The field design, acquisition, and processing of the 3C-2D seismic line are discussed by Gallant et al. (1995) and Gorek et al. (1995). The data were processed by Sensor Geophysical Ltd. of Calgary. Well data, including digits, tickets, and tops, were obtained from PanCanadian Petroleum Ltd.

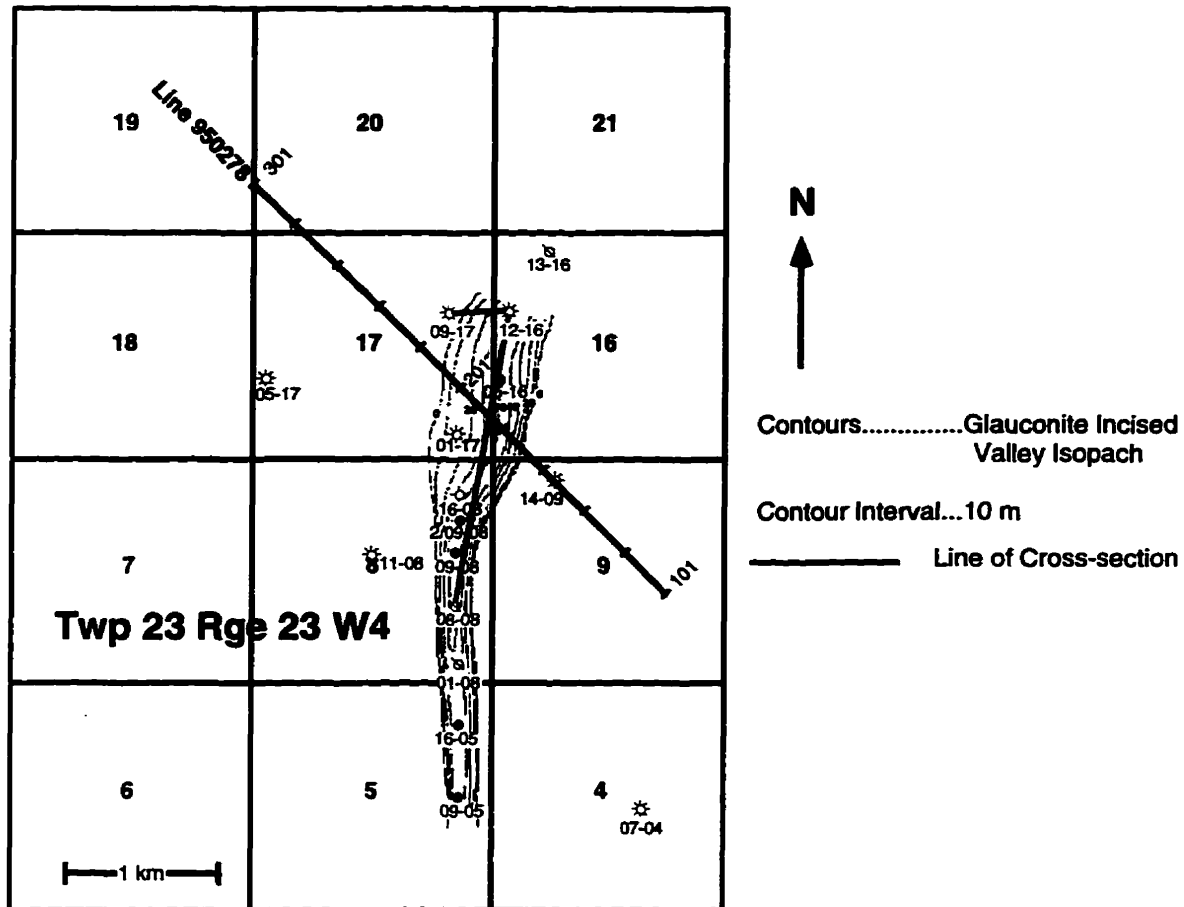


Figure 3.2 Location map of 3C-3D seismic line 950278, well control, and cross section. Contours denote incised valley fill isopach. (Isopach map from Politylo, 1995)

### 3.3 Seismic data acquisition

The Blackfoot Field is located in Township 23, Range 23, West of the 4th Meridian, in south-central Alberta. A 3C-2D broad-band seismic line was acquired by the CREWES Project over the Blackfoot Field in the summer of 1995. The line is 4 km long and trends SE to NW (Figure 3.2); the field acquisition parameters are summarized in Table 3.1. The energy source was 6 kg of dynamite at 12 – 18 m depth. There were 200 stations, with a station spacing of 20 m, and a shot spacing of 20 m at every half station for a maximum fold of 100. The spread was a fixed split-spread layout and all 200 receiver stations were live for each shot. To maximize recording dynamic range, the data were recorded on the ARAM-24 system manufactured by Geo-X Systems Ltd. The data examined in this thesis were recorded by Litton Resources Systems 10 Hz 3-C geophones,

which were deployed in holes 30 cm deep, but not covered over. Individual cables were used to record vertical, radial, and transverse components, for a total of 600 live channels for each shot.

Table 3.1 Field acquisition and recording parameters for the Blackfoot survey

Energy source	dynamite
Source pattern	single hole, 6 kg @ 12 – 18 m
Amplifier type	ARAM-24
Number of channels	848 + 813 (master/slave) total 200 channels per geophone component
Sample rate	1 ms
Record length	6.0 seconds
Recording filter	out-240 Hz, Notch out
Geophones (used for this analysis)	Litton Resources Systems LRS-1033: 10 Hz 3-component, single geophone per station
Number of geophones recorded	200
Receiver interval	20 m
Source interval	20 m
Nominal fold	100
Spread	fixed

The data quality is very good; vertical- and radial-component shot records are shown in Figure 3.3. Ground-roll contamination is quite severe, particularly on the radial component. At the zone of interest, noise due to ground roll is present on offsets out to 400 m on the vertical component and 900 m on the radial component. There is also significant converted-wave refraction energy on the radial component record. Transverse-component records and stacks of the 10 Hz transverse components showed little signal and therefore only the vertical and radial components were fully processed and interpreted.

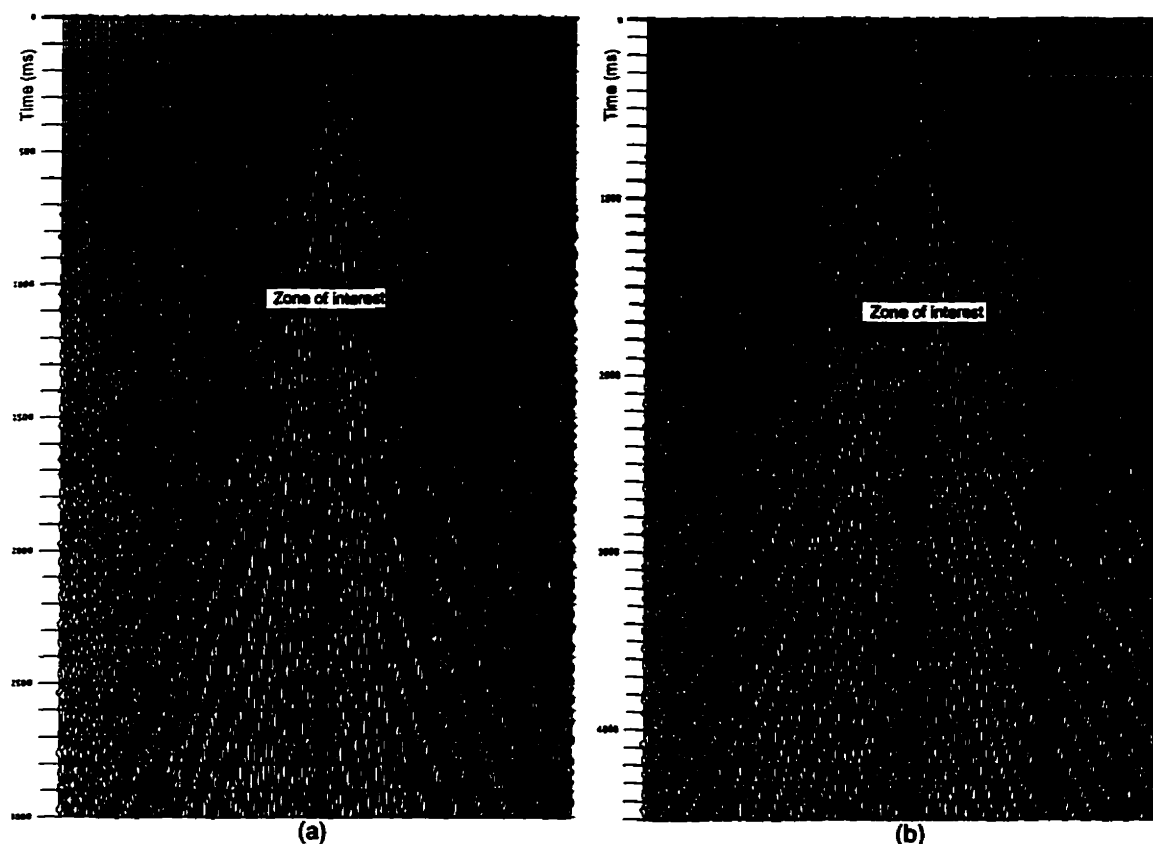


FIG. 3.3 Examples of (a) vertical- and (b) radial-component shot records from the Blackfoot 3C-2D survey.

### 3.4 Data processing

The vertical channel ( $P$ - $P$ ) data were processed by Sensor Geophysical Ltd. using a conventional flow as shown in Figure 3.4 (Gorek et al., 1995). Iterative velocity analysis and residual statics were applied to shot records to obtain the input to the  $f$ - $k$  filter subflow. The  $f$ - $k$  filter was applied to NMO and static-corrected shot records to attenuate the severe low-frequency surface-wave contamination. The filtered records had an improved spectrum for subsequent deconvolution. Prestack surface-consistent deconvolution and time-variant spectral whitening, plus poststack time-variant spectral whitening and  $f$ - $x$  deconvolution were applied to produce a final stacked section with broad bandwidth. The data used in the interpretation had post-stack phase-shift migration applied. The resulting migrated section is shown in Figure 3.5.

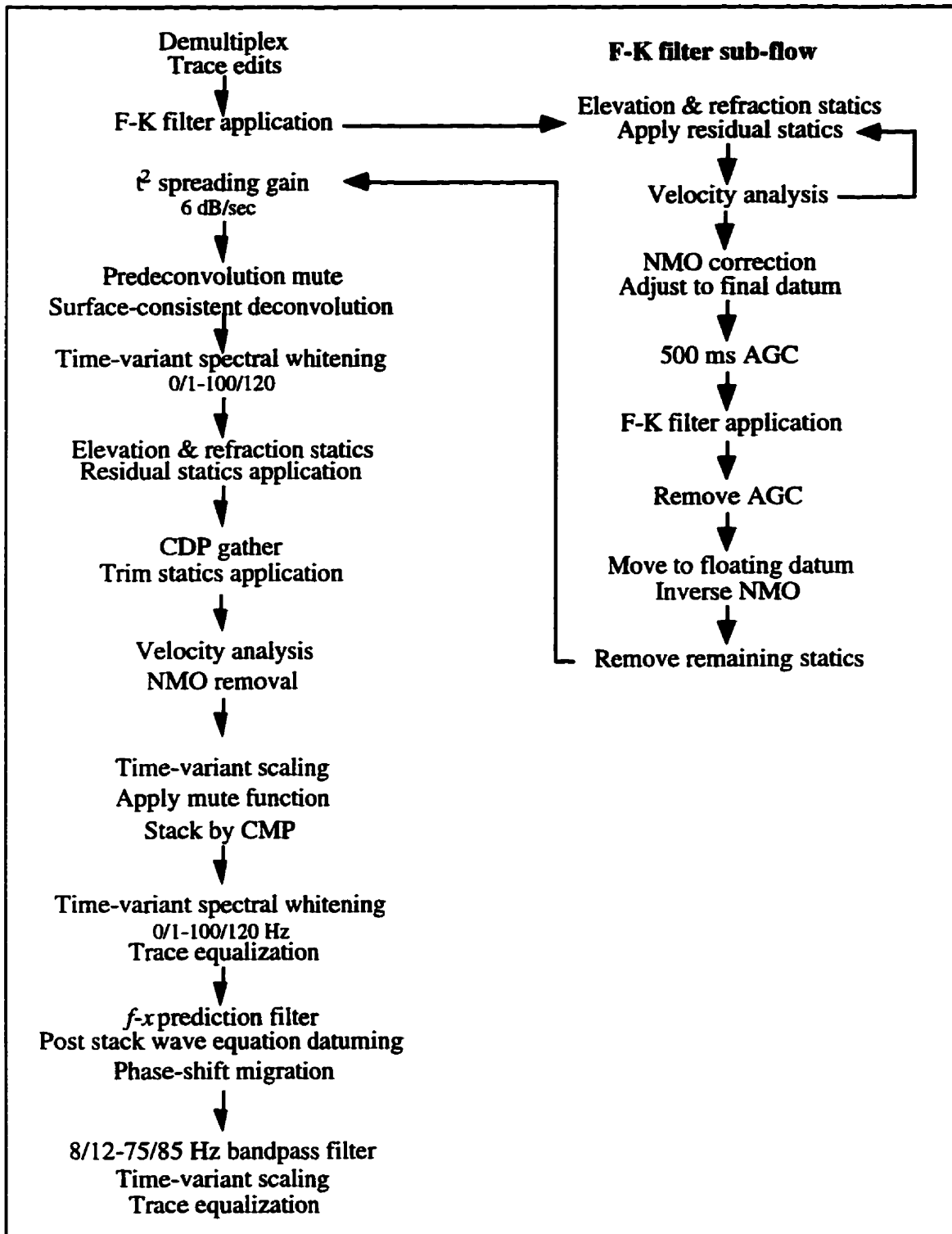


FIG. 3.4. Processing flow for vertical-component seismic data.

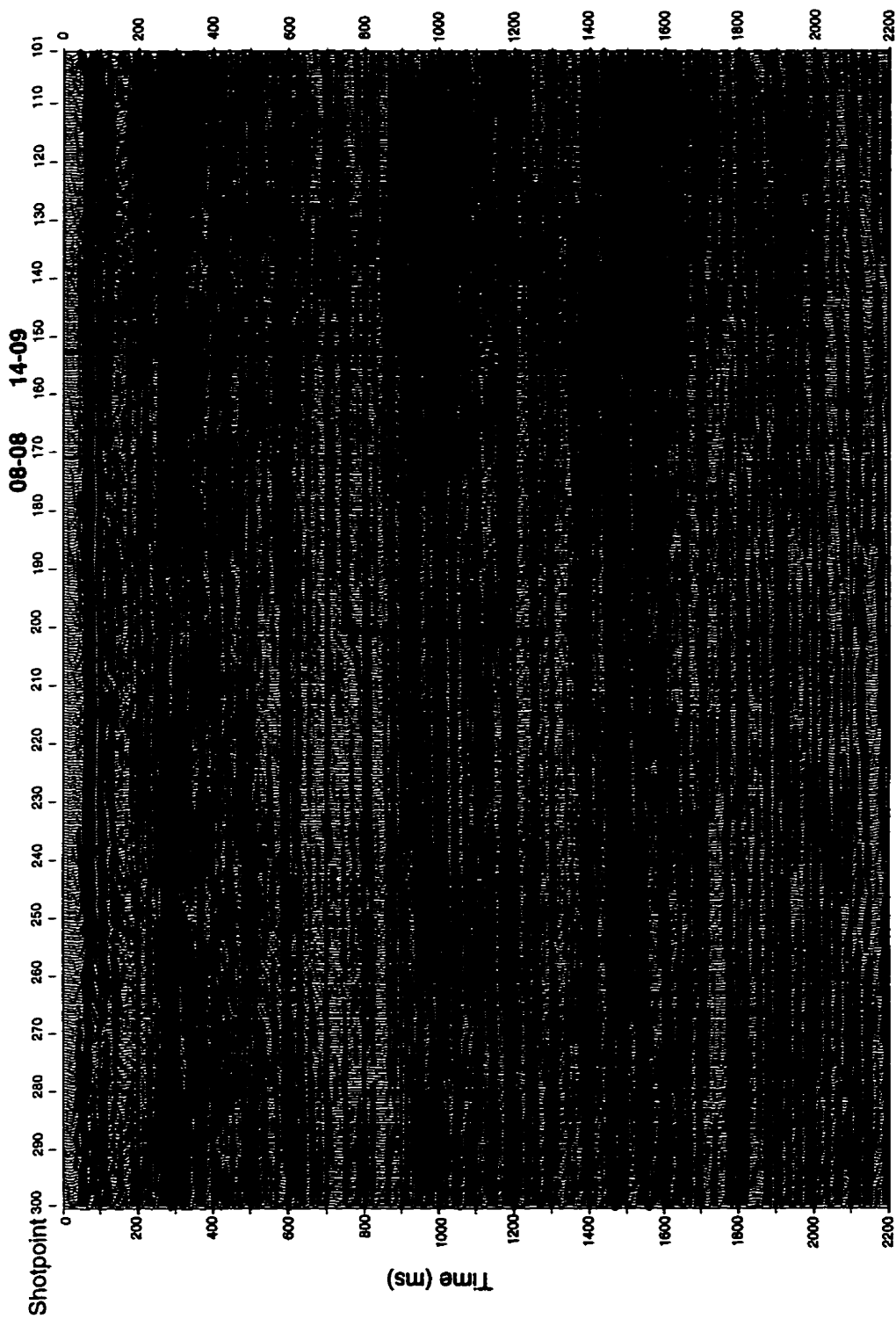


FIG. 3.5. P-P migrated seismic section of line 950278 (full 4 km shown). Outlined area is shown in Figure 3.8.

The radial component data were processed, also by Sensor Geophysical Ltd., using the flow outlined in Figure 3.6. The flow was based on converted-wave processing methods documented in part by Eaton et al. (1990), Harrison (1992), and Harrison and Stewart (1993). The *P-S* data were initially stacked using asymptotic conversion-point binning and an approximate value for  $V_p/V_s$ . Interval  $V_p/V_s$  values were then determined from correlation of the *P-P* and *P-S* sections at the 14-09 well location. The *P*-wave stacking velocity field was then modified using the  $V_p/V_s$  information for subsequent depth-variant binning and also to provide an initial function for converted-wave velocity analysis. The *P*-wave migration interval velocity function was also converted to the *P-S* migration interval velocity function using depth-variant  $V_p/V_s$ . The data used in the interpretation had post-stack phase-shift migration applied. The resulting migrated section is shown in Figure 3.7.



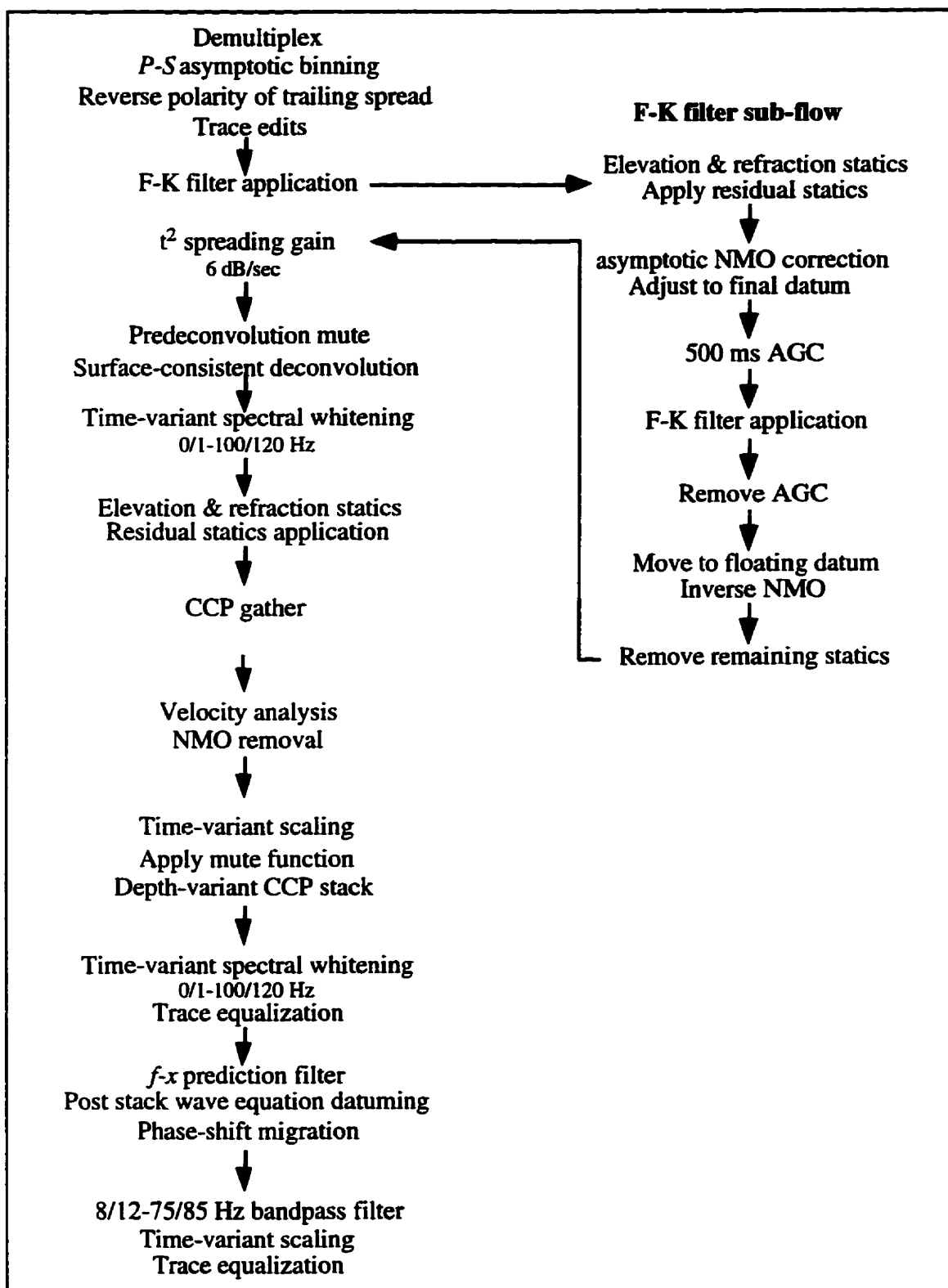


FIG. 3.6. Processing flow for radial-component seismic data.

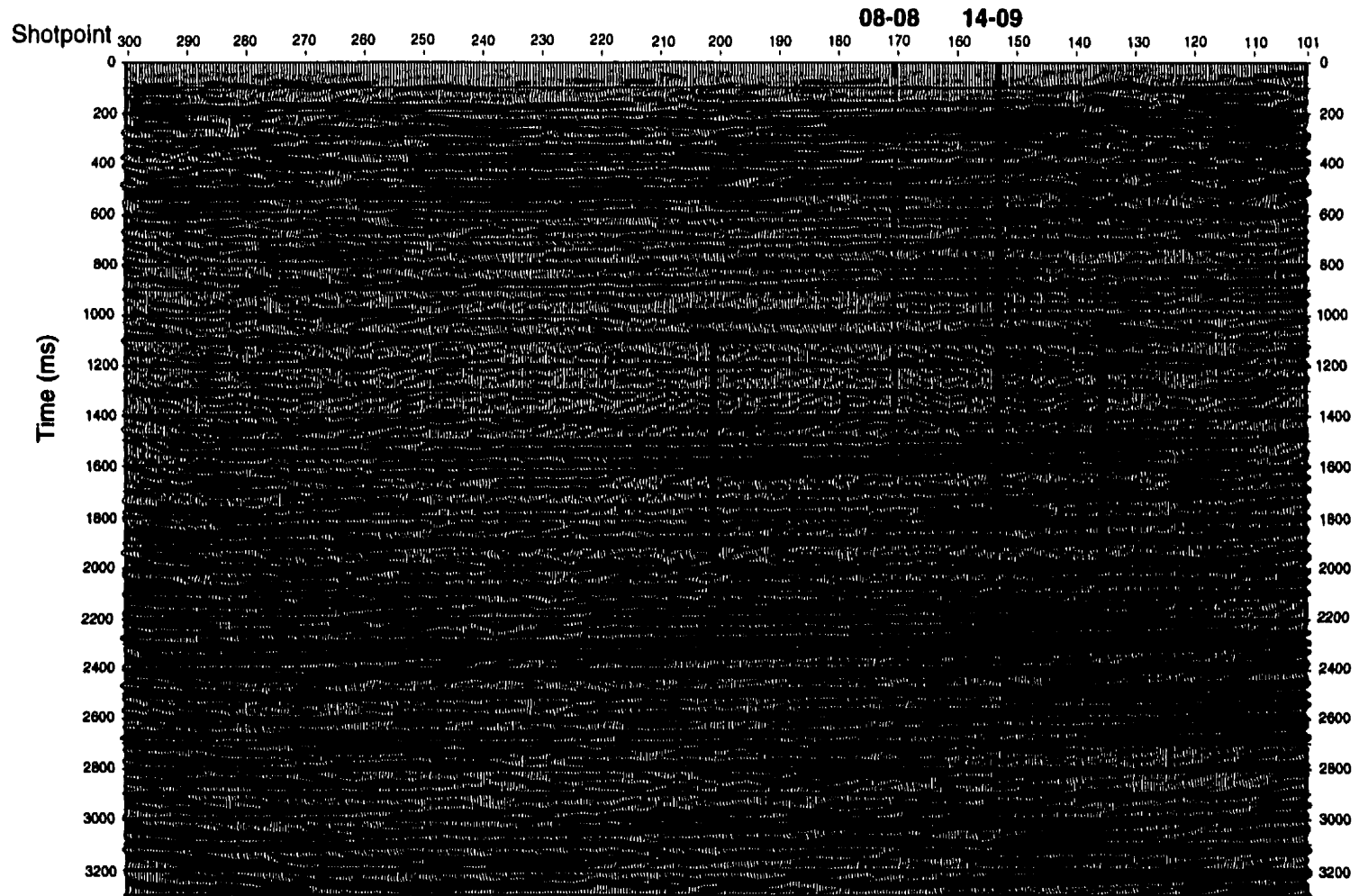


FIG. 3.7. *P-S* migrated seismic section of line 950278 (full 4 km shown). Outlined area is shown in Figure 3.9.

### 3.5 Correlation of *P-P* and *P-S* seismic data

The first step in the interpretation of the Blackfoot multicomponent seismic line, critical to all subsequent analysis, was the correlation between the *P-P* and *P-S* seismic sections. For the Blackfoot survey, this procedure was assisted by existing dipole sonic logs in the area, although no wells with dipole logs are on the line. Through the correlation procedure, the principal horizons on both components were identified.

The identification of seismic events on the *P-P* section is shown in Figure 3.8. Two *P-P* synthetic seismograms are spliced into the section of *P-P* seismic data outlined in Figure 3.5. The synthetic seismograms are from 14-09, which is on the line at SP 156, and 08-08, which has been projected 1.4 km north onto the line at SP 171. Both zero-offset synthetic seismograms were created using GMA LogM software and an Ormsby wavelet with frequencies 8-12-75-85. The seismograms are not check-shot corrected, but a good tie between both synthetic seismograms and the data is evident.

To correlate the *P-P* and *P-S* seismic sections, offset synthetic seismograms were generated from the 08-08 well, as there is no *S*-wave sonic log at the 14-09 well. Using the *P*-wave sonic curve, *S*-wave sonic curve, and density curves as input, offset synthetic seismograms were generated using a ray-tracing procedure documented by Lawton and Howell (1992). Only primary events are included in this procedure. Source-receiver offsets used were from 0 to 1500 m with a receiver spacing of 100 m. This geometry was based on the offset range which was used at the zone of interest for the processed seismic sections. Processing parameters were also used to determine bandpass wavelet frequencies of 8-12-75-85 Hz for the *P-P* synthetic seismogram and 5-10-35-45 Hz for the *P-S* synthetic seismogram. These parameters gave a good match to the data. Polarity convention is that a peak on both the *P-P* and the *P-S* data represents an event from an interface across which there is an increase in elastic impedance.

The *P-S* synthetic seismogram from the 08-08 well is spliced into the *P-S* seismic section in Figure 3.9. The section of *P-S* seismic data shown is outlined in Figure 3.7. The *S*-sonic log was recorded for only 260 m over the zone of interest, but the events tie well. This seismogram is also used to identify the Blairmore, coal, channel, and Shunda events. The two peaks between the Blairmore and the Shunda are quite strong on the

synthetic seismogram but are lower in amplitude and discontinuous on the processed seismic section.

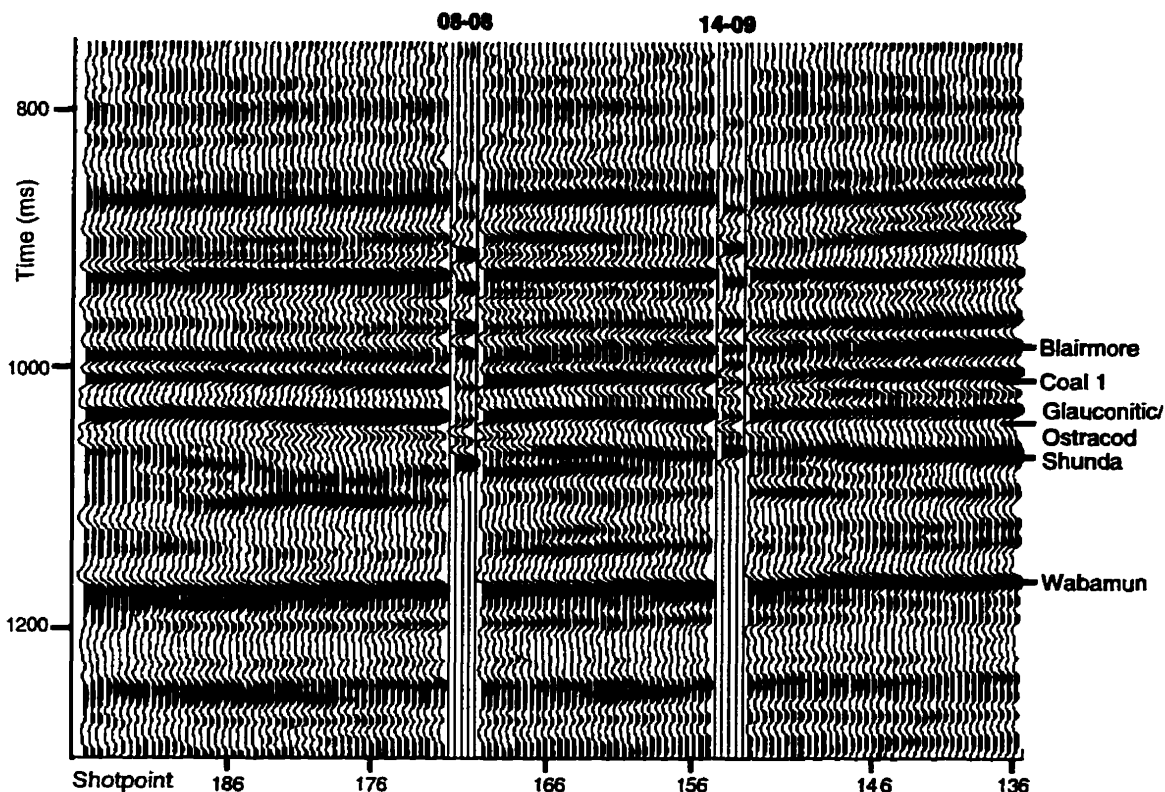


FIG. 3.8. Blow-up of the migrated  $P$ - $P$  section in the zone of interest showing the tie to the 08-08 and 14-09  $P$ - $P$  synthetic seismograms. The seismic data is from the outlined area in Figure 3.5.

The correlation of the  $P$ - $P$  and  $P$ - $S$  synthetic seismograms is shown in Figure 3.10. The  $P$ - $S$  data have been plotted at  $2/3$  the scale of the  $P$ - $P$  data to assist in visual correlation. The sections are correlated from the Blairmore to the Shunda using the offset synthetic seismograms from the 08-08 well as described above. Although there is greater detail on the  $P$ - $P$  seismogram (Figure 3.10a) because of the higher frequency content, the major events correlate well. The three cuts of the channel are resolved on the  $P$ - $P$  seismogram, with two troughs corresponding to porous channel members and the low-amplitude central peak corresponding to the tight lithic member. Conversely, on the  $P$ - $S$  seismogram (Figure 3.10b), the three members are not resolved individually, and the presence of the channel is indicated by a single broad trough. Due to the different bandwidths and consequent difference in tuning effects, the top of the Glauconic channel is very close to a trough on the  $P$ - $P$  seismogram, but occurs at the zero crossing above the corresponding trough on the  $P$ - $S$  data.

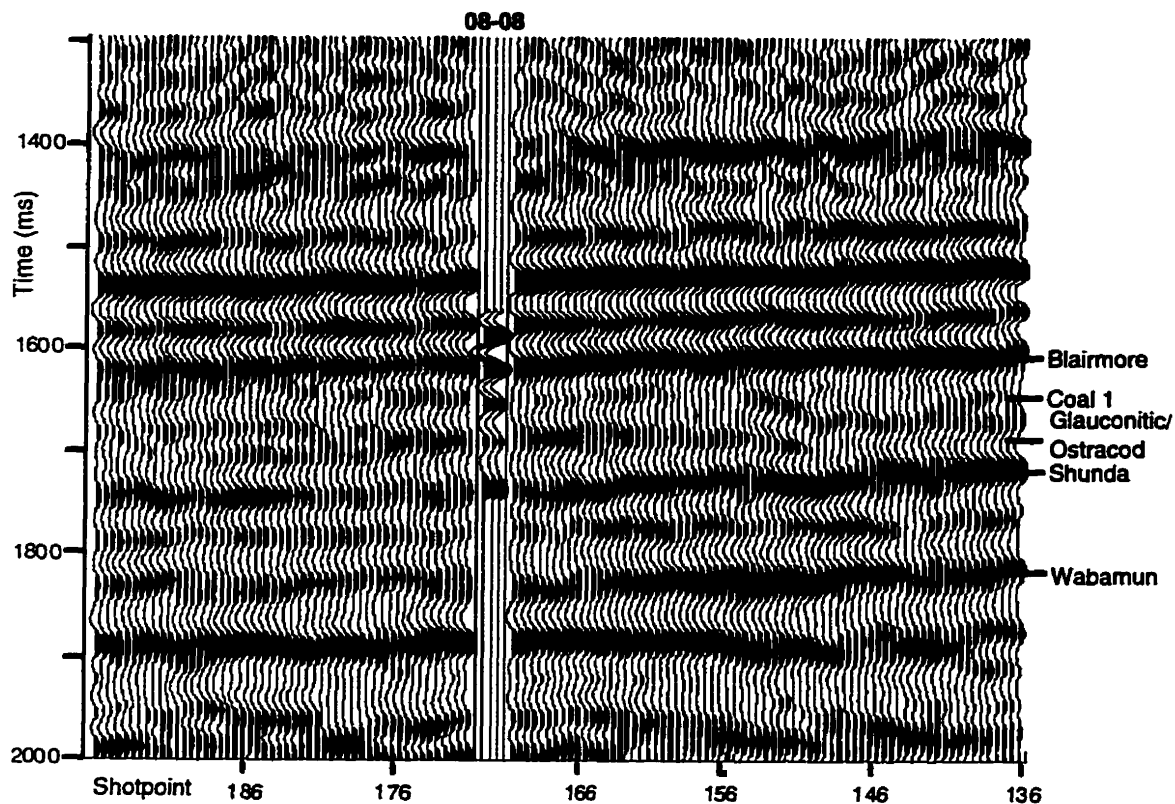


FIG. 3.9. Blow-up of the migrated  $P$ - $S$  section in the zone of interest showing the tie to the 08-08  $P$ - $S$  synthetic seismogram. The seismic data is from the outlined area in Figure 3.7.

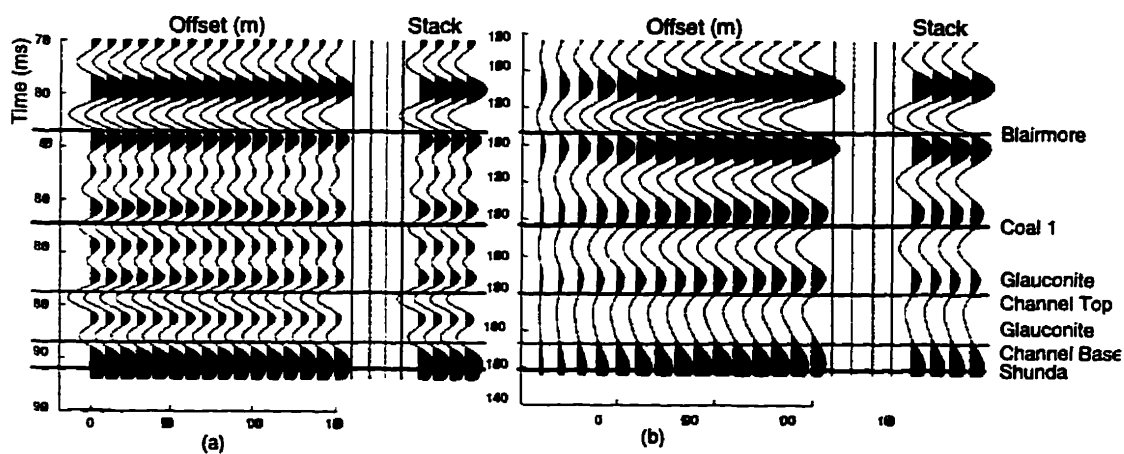


FIG. 3.10. Correlation of (a)  $P$ - $P$  and (b)  $P$ - $S$  offset synthetic seismograms from 08-08. Time scale of  $P$ - $S$  seismogram is  $2/3$  that of the  $P$ - $P$ .

The comparison of the  $P$ - $P$  and  $P$ - $S$  seismic sections is shown in Figure 3.11. The sections are correlated from the Blairmore to the Shunda events using the seismograms from the 08-08 well as described above. Events above this were identified on the  $P$ - $P$  section using the 14-09 well, and can be identified on the  $P$ - $S$  section from the correlation of the seismic sections, as shown in Figure 3.10.

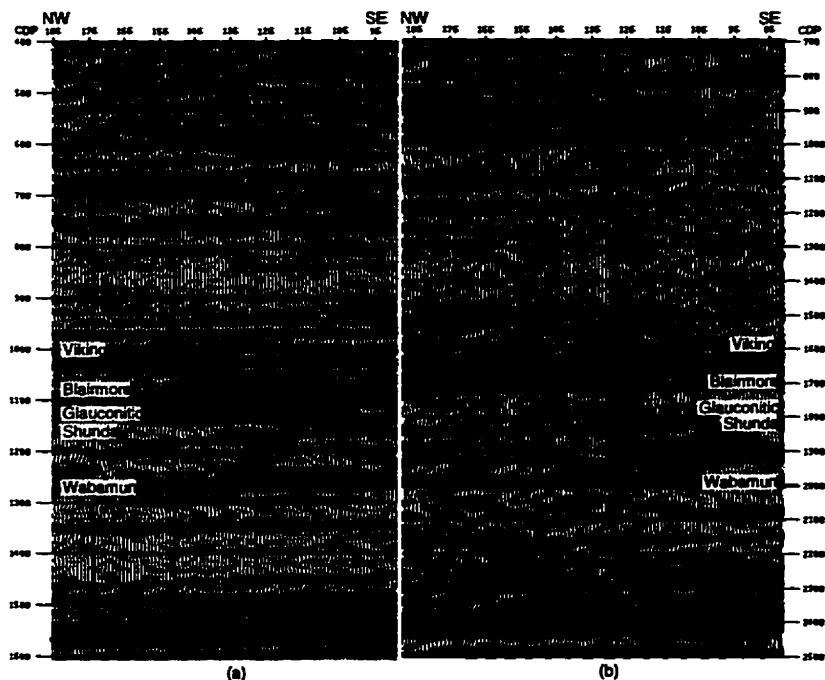


FIG. 3.11. Comparison of (a)  $P$ - $P$  and (b)  $P$ - $S$  seismic sections. Time scale of  $P$ - $S$  seismogram is  $2/3$  that of the  $P$ - $P$ .

### 3.6 Numerical seismic modelling

The reflections above and below the channel can be easily identified and correlated on both  $P$ - $P$  and  $P$ - $S$  sections, but the channel facies interpretation is not straight forward. In order to guide the interpretation process, structural cross-section models were created using the three wells with dipole sonic logs: 08-08, 12-16, and 09-17. These wells represent each of the sand-filled channel, shale-filled channel, and regional facies respectively, and thus were used to predict the corresponding  $P$ - $P$  and  $P$ - $S$  seismic responses. These models were also used to calculate interval  $V_p/V_s$  from  $P$ - $P$  and  $P$ - $S$  isochrons and thus establish the usefulness of this technique for these data.

### 3.6.1 Seismic cross-section models

The models were created from the synthetic cross-section program described by Margrave and Foltinek (1995). To create the well log cross section, synthetic well logs are interpolated between the well locations for the *P*-sonic, *S*-sonic and density logs. The interpolated log cross sections for the *P*- and *S*-sonic logs are shown in Figure 3.12; slowness increases to the right in these log cross sections. For the synthetic seismic cross-section, a stacked offset synthetic seismogram was generated at each log location using the interpolated *P*-wave sonic, *S*-wave sonic, and density logs. The offset synthetic seismograms were generated using the same parameters described in chapter 3.5. The *P-P* synthetic seismic, section with horizon tops identified, is shown in Figure 3.13. The early part of the section is reasonably constant, although tuning affects the character of some events. The zone of primary interest begins beneath the Mannville coals at about 820 ms. The far right of the model, at 9-17, represents the regional section. The Bantry Shale event of the Lower Mannville Group has a very low velocity, marked by a trough, and thus may be mistaken for low-velocity porous sandstone channel-fill. Following this trough there is a broad, low amplitude peak at the top of the Sunburst and Detrital Formations. The model terminates in the Shunda Formation at the Mississippian unconformity, which is represented by a strong peak. Moving left toward the 12-16 well, the model encompasses the channel which has cut through the Ostracod/Bantry Shale and Sunburst Formations, so that the upper trough now marks the top of the Glauconitic channel-fill. Although the 12-16 well is in the channel, it has only a 3 m sandstone unit and is shale-dominated in the Glauconitic Formation. A second trough develops near the lower part of the channel, but has only low amplitude. There is substantial topography on the unconformity, as indicated by the earlier arrival time of the Shunda peak. Between the 12-16 well and the 08-08 well, the channel thickens and the lithology changes from shale to porous sandstone. The upper trough increases in amplitude, thus defining the porous upper units of the Glauconitic channel sands. The peak which begins to develop immediately following it is caused by the tight middle unit, and the lower trough is the event from the lower porous unit. There is only 8 m of Detrital Formation in the 08-08 well, and the Mississippian unconformity surface is high relative to the regional 9-17 well. The Shunda and the following trough are lower in frequency at the 08-08 than at the other two wells, perhaps due to a tuning effect. In this *P-P* model, prospective channel-fill is characterized by the brightening of the upper trough and the development of the middle peak and lower trough.

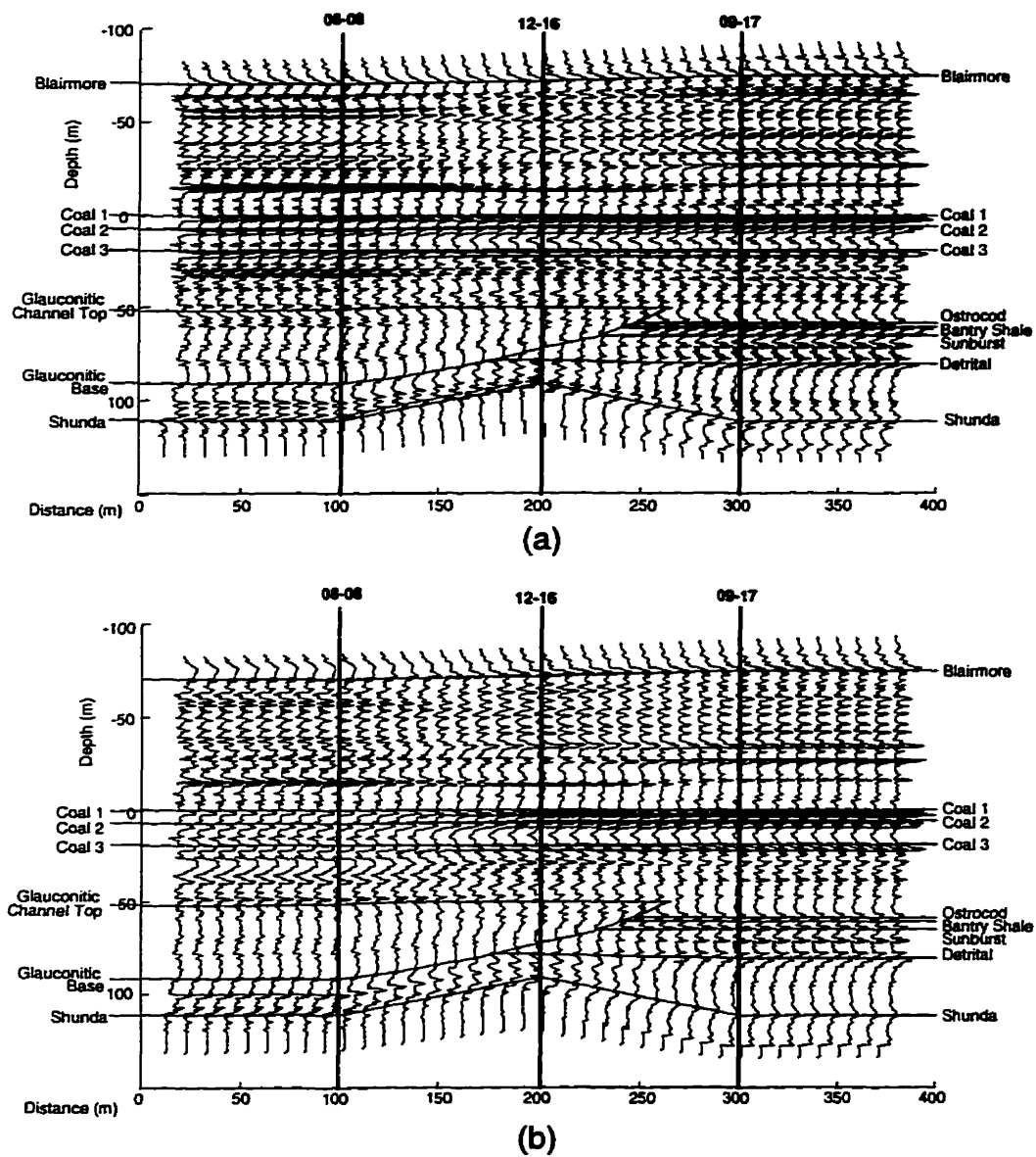


FIG. 3.12. Well log sections using (a) *P*-sonic logs and (b) *S*-sonic logs interpolated from the three wells 08-08, 12-16 and 09-17. Slowness is increasing to the right. Coal 1 has been used as the datum.



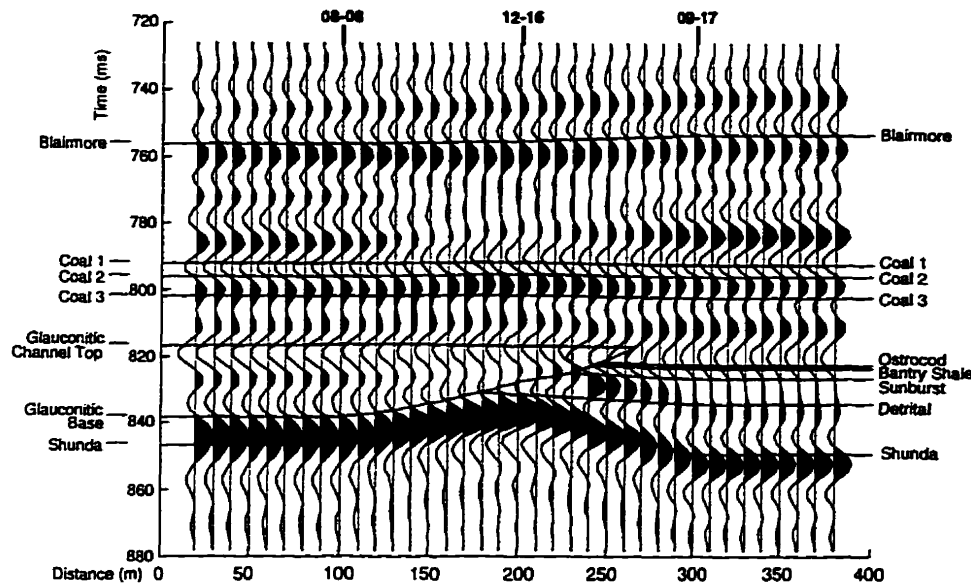


FIG. 3.13. *P-P* synthetic seismogram section generated with a 8-12-75-85 bandpass wavelet. Horizons are flattened on Coal 1.

The *P-S* cross section with horizon tops is shown in Figure 3.14. Above the zone of interest, there are three peaks which extend across the section: the peak whose zero-crossing occurs near the Blairmore top, a second peak at about 1250 ms, and a third peak which occurs just below Coal 3 and decreases in dominant frequency in the regional response at the 9-17 well. Here, there is a broad trough encompassing the Ostracod/Bantry Shale, followed by a low amplitude peak at the top of the Detrital Formation and a high-amplitude Mississippian peak. Entering the channel at the 12-16 well, the Detrital peak is no longer evident. The upper trough occurs near the Glauconitic Formation top as the channel cuts down through the Ostracod/Bantry Shale and the Sunburst Formation. This trough broadens as the channel thickens and the lithology changes from predominantly shale fill to predominantly sandstone fill. The three individual channel members are not resolved due to the limited bandwidth of the seismic data. In this *P-S* model, the edge of the channel is determined by the brightening of the Glauconitic trough and loss of the Detrital peak. The thicker sandstone portion of the channel is characterized by the broadening of the trough across the Glauconitic Formation.

As mentioned previously, development of channels is not necessarily directly related to the antecedent Mississippian topography (A. Politylo, pers.comm., 1995). Therefore, although these wells are examples from the three stratigraphic environments of interest, they are not necessarily representative of the seismic signature for each of these

environments. That may vary depending on the topography of the Mississippian surface, the thickness of the Detrital sediments beneath the Glauconitic Formation, and the thickness of the valley-fill sediments. All three valley-fill units may be present, as in the 08-08 well, or the middle and/or lower units may be absent. It should also be noted that this cross section does not represent an actual geological cross section across the channel. As shown in Figure 3.2, the wells are not on the seismic line, nor does their line of section cross the channel.

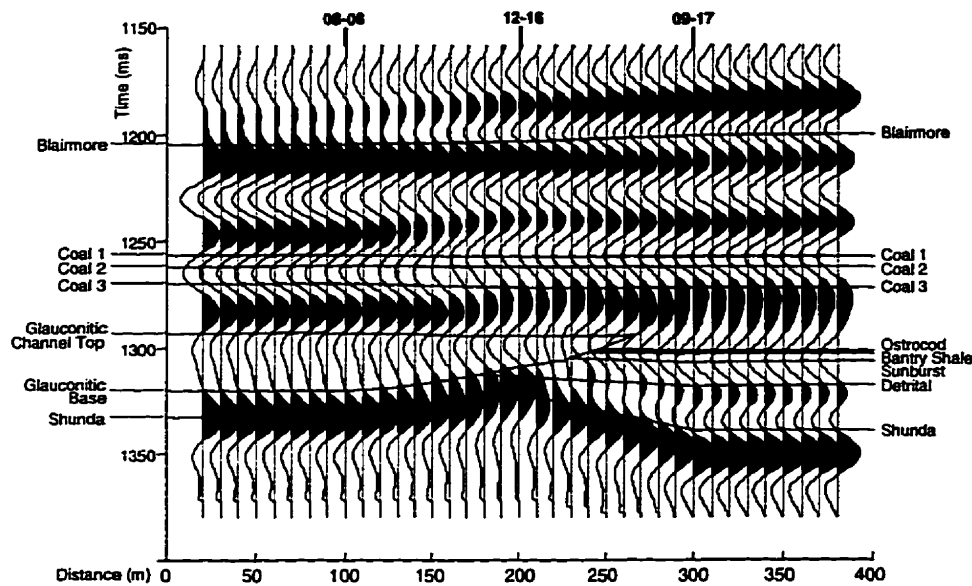


FIG. 3.14.  $P$ - $S$  synthetic seismogram section generated with a 5-10-35-45 bandpass wavelet. Horizons are flattened on Coal 1.

### 3.6.2 $V_p/V_s$ analysis of the seismic model

Interval  $V_p/V_s$  values were calculated across the zone of interest on synthetic seismic models to assess the feasibility of using this method of analysis on the processed field data. The interval over which  $V_p/V_s$  was calculated extends from the peak which occurs immediately below the Blairmore top to the Shunda peak at the base of the model. The correct tops are known from the wells and are plotted on the model. In some cases, the nearest seismic event may be tuned and thus not occur exactly at the horizon top. However, when picking seismic data, the interpreter does not have a priori information and must pick on a seismic event which is closest to the geological top. In order to most closely replicate the seismic data analysis, maximum amplitude peaks were picked on the models using automated picking on the workstation.

The results of this analysis are plotted in Figure 3.15. The dotted line shows the exact values, with a smoothed solid line overlay.  $V_p/V_s$  is significantly lower across the sand channel, about 1.85, than across either the shale-filled channel or the regional section, where it averages about 1.93. Both seismic models were created from the same depth model, therefore such lateral variations in  $V_p/V_s$  may be due to velocity changes, which in turn are a result of changing facies in the zone of interest. This result is in agreement with the literature, which suggests that  $V_p/V_s$  will increase in clastics as shale or clay content increases (e.g. Miller and Stewart, 1990; Eberhart-Phillips et al., 1989; Han et al., 1986; Castagna et al., 1985).

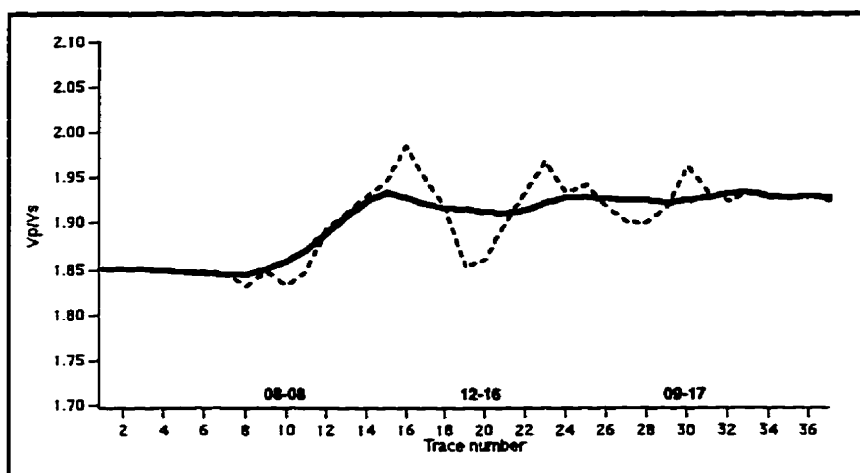


FIG. 3.15.  $V_p/V_s$  values from the cross-section model for the interval from the Blairmore peak to the Shunda peak. The dotted line shows the actual picks and the solid line the smoothed version. Traces numbers are equal to the distance divided by 10 on the models.

### 3.7 Seismic interpretation

Using the results of the correlation (Chapter 3.5) and the numerical modelling (Chapter 3.6), the  $P$ - $P$  and  $P$ - $S$  migrated sections were interpreted on a workstation. The  $P$ - $P$  and  $P$ - $S$  components were examined concurrently in order to maintain a consistent interpretation. Amplitude and character changes were important considerations for the detailed interpretation of the channel facies. Equivalent  $P$ - $P$  and  $P$ - $S$  horizon isochrons were used to calculate interval  $V_p/V_s$  values from the data. The edges of the incised valley and the valley-fill were interpreted from the multicomponent seismic data and the interval  $V_p/V_s$  profile.

### 3.7.1 *P-P* and *P-S* seismic data interpretation

The *P-P* interpretation for part of the line over the zone of interest is shown in Figure 3.16. The eastern edge of the Glauconitic channel is interpreted to cut through the Ostracod and Bantry Shale members and into the Detrital at about SP 161. The Detrital peak just above the Shunda is replaced by a trough, which increases in amplitude westward. The central peak, indicative of the tight central member, also begins to develop at this point and increases in amplitude westward. The trough-peak-trough pattern closely matches the seismic model in the sandstone channel (Figure 3.13). Coincident with the channel development, is a Mississippian low from shotpoint 166 to 191. The Detrital then thickens sufficiently for the top of Detrital peak to appear above the Shunda. The Detrital horizon overlay is not shown where the Detrital peak tunes with the Shunda peak. The Shunda is high at the 08-08 well and the Detrital is relatively thin, so the *P-P* seismic model matches the data best at about SP 171, where the Shunda is shallower.

The western edge of the channel is harder to define, but may extend as far as SP 211. The lower trough of the Glauconitic sandstone loses amplitude at about SP 186, where the Shunda time structure appears shallower. The change in seismic character suggests that the valley fill may become shalier towards the west. The 12-16 well, which is shale at the Glauconitic, ties best when projected onto the seismic line at about SP 195. The upper trough is quite strong, and the central peak detectable, but the lower trough is poorly defined. The 9-17 regional well should tie the line anywhere west of S.P 211. However, the tie is poor, both across the zone of interest and also above the coals, where the isochron between the first two peaks in the Mannville is much thicker on the seismogram than on the data. This well ties the data best on the easternmost part of this line, near SP 101.

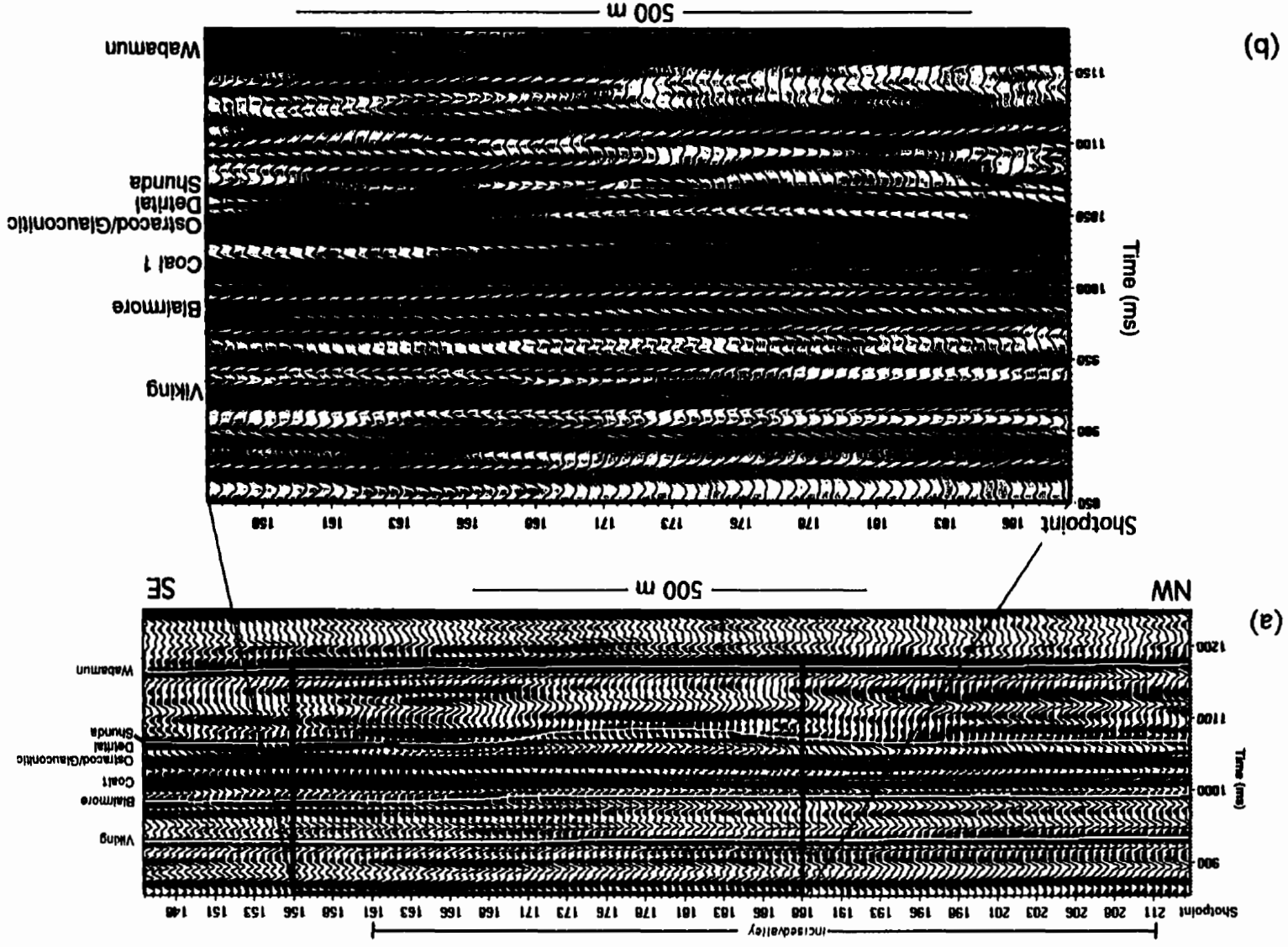


FIG. 3.16. Interpretation of the *P-P* seismic data showing (a) the lateral extent of the incised valley and (b) a blowup of the eastern and central portion of the valley.

The *P-S* interpretation of the same portion of the line for the same interval is shown in Figure 3.17. The Blairmore event is clearly identifiable, as is the Shunda event, although there are some amplitude variations on the latter. Peak events between the Blairmore and the Ostracod/Glauconitic events tend to be discontinuous and difficult to pick. There is less time structure on the Shunda event from shotpoints 166 to 191 than on the *P-P* section. Also of note is the dimming of the Shunda event between shotpoints 167 and 183.

As with the *P-P* data, the channel portion of the *P-S* seismic model ties the *P-S* data best at about SP 171, where the broad trough is characteristic of thick channel sands. The Glauconitic/Ostracod trough brightens at SP 162 at the interpreted eastern edge of the channel, broadens in the centre of the channel, and brightens again out to about SP 188, where the channel may be becoming shalier. This brightening of the Ostracod/Glauconitic trough is similar to the *P-S* model response at 12-16, where the channel is thinning and shaling out. The 12-16 well ties the data quite closely at shotpoint 195 and shows the narrowing of the Glauconitic trough as the channel thins. The 09-17 ties well down to the base of the coals, but the tie at the Shunda is poor.

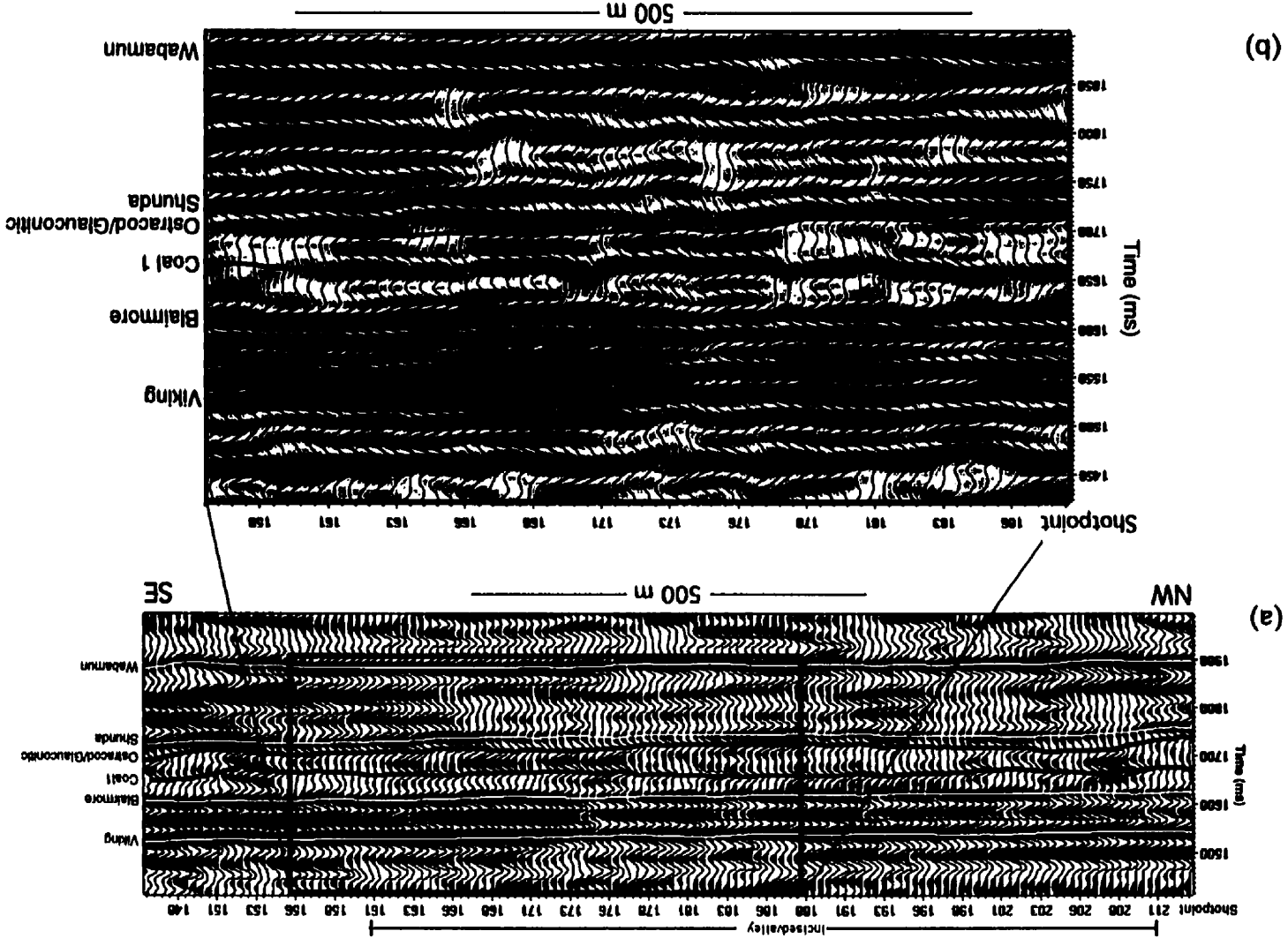


FIG. 3.17. Interpretation of the *P-S* seismic data showing (a) the lateral extent of the incised valley and (b) a blowup of the eastern and central portion of the valley.

### 3.7.2 $V_p/V_s$ analysis of the seismic data

The horizons used for  $V_p/V_s$  analysis must bracket the zone of interest and be correlatable and interpretable on both  $P-P$  and  $P-S$  sections. Error is introduced into the results from tuning effects if the interval used is too narrow, yet variations within the zone of interest will be averaged out if the interval is too large. For these data, the Viking to Shunda interval best fit these criteria. It was preferred to the Blairmore to Shunda interval as the  $V_p/V_s$  profile showed the same trends but was less noisy.  $P-P$  and  $P-S$  isochrons for the Viking to Shunda are shown in Figure 3.18. There is a time-structural low with a relief of 25 ms on the  $P-P$  Shunda event between shotpoints 167 and 191, causing an increase in the  $P-P$  Viking to Shunda isochron. There is only 10 ms of time structure on the  $P-S$  Shunda event and the isochron increases only slightly. Using equation (1) from Garotta (1987), the  $V_p/V_s$  profile for this interval was calculated (Figure 3.19). There is a  $V_p/V_s$  anomaly from shotpoints 167 to 191, which also coincides with the time-structural low on the  $P-P$  Shunda event. The anomaly does not extend westward as far as the isopach map in Figure 3.3 indicates.

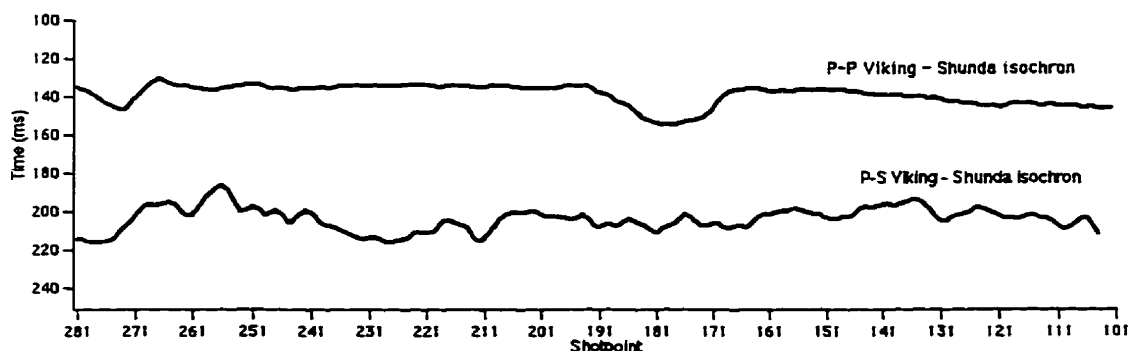


FIG. 3.18.  $P-P$  and  $P-S$  isochrons measured from the line 950278 for the Viking to Shunda interval. The time structure anomaly from shotpoints 165 to 191 on the  $P-P$  isochron is not evident on the  $P-S$  isochron.

According to the modelling results, the decrease in  $V_p/V_s$  determined from of the seismic data is caused by a transition from a shaly to a sandstone facies within the channel. The lateral extent of the low  $V_p/V_s$  value is thus interpreted to reflect the lateral extent of sandstone-fill within the channel. Those portions of the incised valley where  $V_p/V_s$  is higher (greater than 2.0) are interpreted to indicate shale fill within the incised valley.



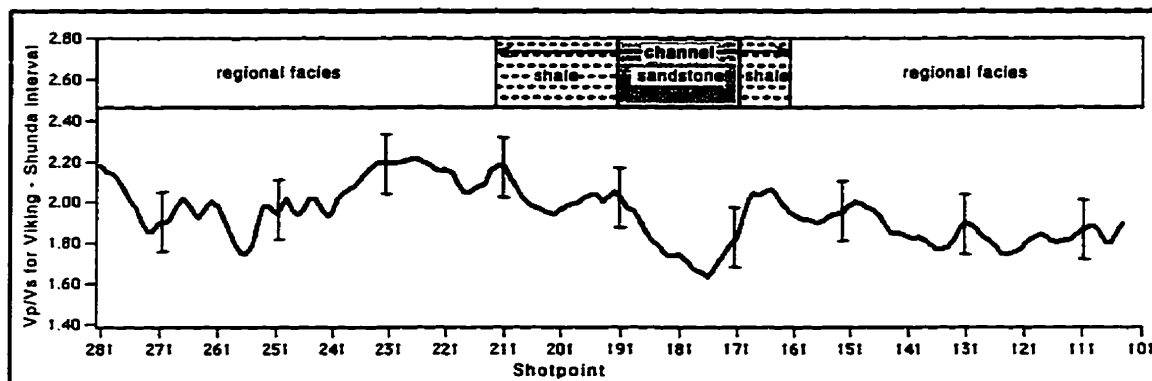


FIG. 3.19.  $V_p/V_s$  values calculated for line 950278 for the Viking to Shunda interval. There is a  $V_p/V_s$  low from shotpoints 167 to 191, interpreted to indicate sandstone facies within the incised valley. Uncertainty bars based on  $\pm 2$  ms uncertainty in horizon picking.

### 3.8 Well log analysis

$V_p/V_s$  analysis of the seismic data and of the seismic model both demonstrate a decrease in  $V_p/V_s$  across the sandstone reservoir. However, this technique cannot establish whether the  $V_p/V_s$  variation is due to changes in  $V_p$ ,  $V_s$ , or both. The dipole sonic log data were analyzed in order to ascertain the cause of the  $V_p/V_s$  response. The data are  $P$ -wave and  $S$ -wave transit times from the 08-08 and 12-16 dipole sonic logs from the Glauconitic Formation. This formation is largely sandstone in the 08-08 well and primarily shale, with a 3 m layer of sandstone, within the 12-16 well. Transit times were converted to velocity and the gamma logs from the same zone were used for shale estimates.

Figure 3.20 is a plot of  $V_p/V_s$  versus gamma log values for the 08-08 and 12-16 wells in the Glauconitic formation. The data are very scattered, although there is a general trend for  $V_p/V_s$  to increase with increasing gamma log values, which in turn reflect increasing shale content. The majority of the data points from the 08-08 well have API values less than 90 and there is a dense cluster of points with values of less than 40 API. Most points from this well have  $V_p/V_s$  values ranging from 1.55 to 1.75; values indicative of sandstone lithologies (e.g. Miller and Stewart, 1990; Eberhart-Phillips et al., 1989; Han et al., 1986; Castagna et al., 1985). In contrast, most of the 12-16 data points have gamma ray values above 80 API and have  $V_p/V_s$  values from 1.80 to 1.95. The exception are the data points from the thin layer of sandstone within the Glauconitic Formation. These have low gamma readings, generally less than 40 API, and also low  $V_p/V_s$  values, mostly from

1.60 to 1.70. The data points from the sandstone layer plot in a distinctly different region of the graph than the 12-16 data points from the shale section. These results are in agreement with the work of Vernik and Nur (1991), Han et al. (1986), and Castagna et al. (1985), which show that  $V_p/V_s$  will increase as shale content increases.

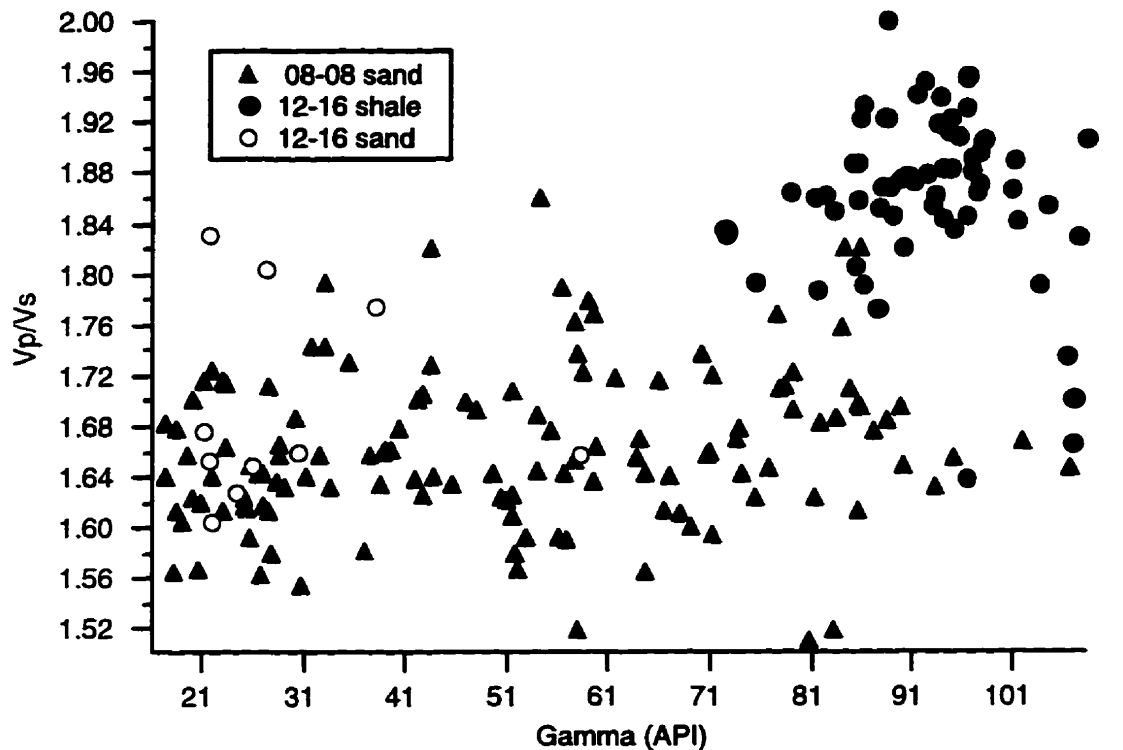


FIG. 3.20.  $V_p/V_s$  versus gamma values in the Glauconitic Formation for the 08-08 and 12-16 wells.

The cause of the increase in  $V_p/V_s$  with increasing shale content is illustrated by the graph of  $V_s$  versus  $V_p$  shown in Figure 3.21. Using the  $P$ -wave velocity alone, sandstone from the 08-08 well cannot be distinguished from shale from the 12-16 well. However,  $S$ -wave velocities are significantly greater in the 08-08 sandstone section than the 12-16 shale section. Again, the cluster of points from the thin 12-16 sandstone layer also have a relatively higher  $S$ -wave velocity and plot in the same region as the 08-08 data. This plot indicates that the increase in  $V_p/V_s$  with increasing shaliness is due to  $V_s$  decreasing while  $V_p$  remains relatively constant. The relationships between  $V_p$  and  $V_s$  shown in Figure 3.21 are quasi-linear, with different gradients for the two wells. The relationship between these gradients and lithology, especially shale content, is a subject for further investigation.

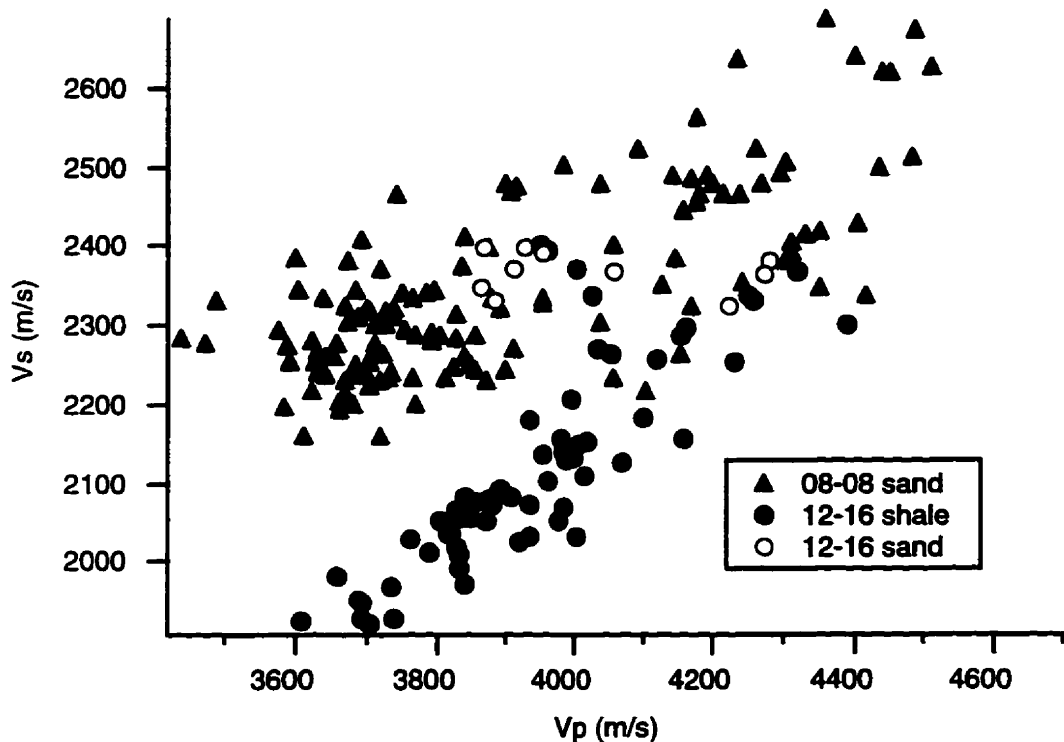


FIG. 3.21.  $V_s$  versus  $V_p$  in the Glauconitic Formation for the 08-08 and 12-16 wells.

### 3.9 Channel interpretation and discussion

The interpretation of the incised valley fill stratigraphy and lithofacies is developed from the combined results of the numerical modelling, seismic interpretation, and well log analysis. The incised valley fill is interpreted to extend from shotpoint 161 in the southeast to shotpoint 191 in the northwest. This is based on the character and amplitude changes observed on both the seismic cross-section models (chapter 3.6) and the  $P-P$  and the  $P-S$  seismic sections (chapter 3.7). A decrease in  $V_p/V_s$  is observed for the Viking to Shunda interval from shotpoints 167 to 191. Both the seismic cross-section model (chapter 3.6) and the well log analyses (chapter 3.8) support the explanation that this anomaly is due to the presence of sandstone-fill within the channel. Higher  $V_p/V_s$  values on the western portion of the channel, from shotpoints 191 to 211, indicate a transition to a shalier facies within the incised valley. This interpretation is supported by changes in seismic character and amplitude on both  $P-P$  and  $P-S$  seismic sections at the Glauconitic level over this portion of the line. On the  $P-P$  and  $P-S$  seismic cross-section models, similar character and amplitude changes occur at the 12-16 well, where the incised valley is thinning and becoming shalier.

Well log evidence suggests that the decrease in  $V_p/V_s$  across the sand-filled portion of the channel is caused by an increase in  $V_s$  accompanied by minimal change in  $V_p$ . This conclusion is supported by the  $P$ - and  $S$ -wave velocity inversions of this seismic line by Ferguson et al. (1996). These workers showed a 200 m/s increase in  $S$ -wave velocity in the Glauconitic channel between shotpoints 172 and 191. In contrast, the  $P$ -wave velocity was fairly constant in this zone.

The underlying assumption of  $V_p/V_s$  analysis is that geological structure will affect both components equally and thus not affect the  $V_p/V_s$  ratio. On the  $P$ - $P$  data, the Shunda event is an ambiguous pick which creates uncertainty in the  $V_p/V_s$  result. The relative time structure on the Shunda event is greater on the  $P$ - $P$  section than on the  $P$ - $S$  section. If the  $P$ - $P$  Shunda time structure reflects real topography, why is it not as apparent on the  $P$ - $S$  data? It may be that the  $S$ -wave velocity of the sediments within the low is higher than in the surrounding sediments, causing pullup on the  $P$ - $S$  Shunda event and less time structure. However, there is no evidence of pullup on the underlying Wabamun event to support this hypothesis. Another possibility is that, because the peak frequency of the  $P$ - $S$  data is only about half that of  $P$ - $P$  data, it has a longer wavelength and lower vertical and horizontal resolution. This smoothes the  $P$ - $S$  horizons vertically and laterally, so that the Shunda event is more continuous on the  $P$ - $S$  section and easier to pick. However, it may also be smoothing out some real topography because of the larger Fresnel zone. Finally, as noted in chapter 3.7, the Shunda event dims from shotpoints 167 to 183 on the  $P$ - $S$  data, which corresponds to the time-structure low observed on the  $P$ - $P$  data. The dimming on the  $P$ - $S$  data may thus be the result of destructive wavelet interference in a Shunda topographic low thick Detrital sediments. In contrast, the Detrital and Shunda events may tune constructively where the Detrital is thinner.

The magnitude of the  $V_p/V_s$  anomaly on line 950278 is larger than the anomaly predicted by the cross-section models, even though the interval used is larger. This may be due to: 1) a thicker sandstone section at the anomaly than in the 08-08 well, 2) the presence of gas within the incised valley, 3) changes occurring within the  $V_p/V_s$  interval but outside the zone of interest, or 4) uncertainties in the horizon picks.

## Chapter 4 – Discussion and Conclusions

### 4.1 Discussion

This thesis discusses the application of multicomponent seismic technology to two case studies; however, the methods developed are generic and applicable to the interpretation of multicomponent seismic data elsewhere. Whenever multicomponent data are acquired, the interpreter has the advantage of working with at least two seismic datasets. It is useful to refer to both components while picking horizons, especially in noisy zones where an event on one section locally may be stronger than on the other. Horizons may be better imaged on one or the other of the sections because differences in travel path, wavelength, and reflectivity result in different multiple paths and wavelet interference effects. The calculated  $V_p/V_s$  values also serve as a quality control check on the horizon interpretations.  $V_p/V_s$  values which are outside the reasonable range appropriate for the local geology indicate mispicks and the need to revisit the interpretation.

$V_p/V_s$  analysis, demonstrated in both case studies, is a fundamental method in multicomponent seismic analysis. The time interval over which  $V_p/V_s$  is measured is critical for this technique. If the interval is much larger than the zone of interest, changes within the target zone may not be detectable. Also, the possibility that observed changes in  $V_p/V_s$  are due to geological variations occurring outside the zone of interest increases. Conversely, if the bounding horizons are too close to the zone of interest, there may be wavelet interference effects which introduce picking errors. A limitation of the technique is that there may not be a suitable interval over which to perform the analysis. An underlying assumption of  $V_p/V_s$  analysis is that geological structure will affect both components equally and thus not affect  $V_p/V_s$ . This requires that the same geological event is being picked on both components. On real data, it may not be possible to do this exactly due to differences in bandwidth between the components. However, this interpretative procedure is still an effective tool because the emphasis is on detecting lateral  $V_p/V_s$  variations rather than determining absolute  $V_p/V_s$  values.

Conventional  $P$ - $P$  seismic data had been previously acquired at both Blackfoot and Lousana, but had limited value in detecting the targets. The objective of both 3-C seismic surveys was to add value by distinguishing reservoir from nonreservoir lithofacies. The two case histories differ in that the Lousana target is an isolated carbonate buildup, whereas

the Blackfoot target is an incised valley infilled with siliclastic sediments. At Lousana, the distinction is between dolomite and anhydrite, and at Blackfoot it is between sandstone and shale. At Blackfoot there is the advantage that the  $V_p/V_s$  contrast is greater between sandstone and shale than between dolomite and anhydrite. At Lousana, higher fractional porosity within the dolomite increased the  $V_p/V_s$  contrast between it and anhydrite. Thus the zones of lowest  $V_p/V_s$  are unambiguously the most prospective. At Blackfoot, the role of porosity is unclear. In sandstones, porosity detection is complicated by the tendency for  $V_p/V_s$  to increase with porosity as well as with shale content.

Multiples contaminated the Lousana data at the zone of interest, particularly on the  $P-P$  data. This resulted in mis-ties between  $P-P$  synthetic seismograms and seismic data, and introduced uncertainty into the  $V_p/V_s$  analysis. At Blackfoot, uncertainty arises from the difficulty in picking the Shunda event, especially on the  $P-P$  seismic data. For both datasets, the choice of intervals used in  $V_p/V_s$  analysis was limited by data quality on one or both components.

The database differed between the two datasets. There are two orthogonal lines at Lousana, adding greater areal coverage to the survey than is available for Blackfoot. However, the well logs from Lousana are older and of overall poor quality. Sonic and density logs are not available for a number of wells in the area, and there are no dipole sonic logs for  $S$ -wave velocity control. Therefore, assumed  $V_p/V_s$  values had to be incorporated into the  $P-S$  models at Lousana. However, there are four wells located on the seismic lines, which corroborated the conclusion that  $V_p/V_s$  can be used to map porosity within the Nisku reservoir. At Blackfoot, dipole-sonic logs facilitated  $P-P$  to  $P-S$  seismic data correlation and provided input to  $P-P$  and  $P-S$  seismic models. The models were valuable for seismic characterization of each of the sand channel, shale channel, and regional environments and provided objective measurements of  $V_p/V_s$ .

## 4.2 Conclusions

The following conclusions were drawn from this study:

### 4.2.1 Lousana Field

1. A confident correlation between *P-P* and *P-S* seismic sections was obtained from *P-P* and *P-S* offset synthetic seismograms generated from a *P*-wave sonic log and a constant  $V_p/V_s$ .
2. Although there were no *S*-wave sonic logs available for this area, interval  $V_p/V_s$  values were extracted successfully at two wells by iteratively matching *P-S* seismograms to *P-S* stacked data. The  $V_p/V_s$  values thus derived from an interval which contained the zone of interest are lower at a producing oil well (1.75) than a basinal anhydritic well (2.10).
3. Long wavelength vertical variations in interval  $V_p/V_s$  correlate with changes in age, depth of burial, and gross lithology. The Mesozoic section which is shallower, younger, and is comprised primarily of siliclastic rocks with a high shale content has a higher average  $V_p/V_s$  (2.26) than a deeper, older Paleozoic section with a predominance of carbonate rocks (average  $V_p/V_s = 1.85$ ).
4. Within the Nisku target zone, short wavelength lateral variations in  $V_p/V_s$  correlate to porosity changes. On line EKW-002,  $V_p/V_s$  is lower at two oil well locations, where there is 25 m of porous dolomite at the Nisku level, than at a third well location, where the Nisku is tight anhydrite. On line EKW-001, there is a  $V_p/V_s$  low at the 14-19 well location, which has 17 m of Nisku porosity.
5. Forward log-based seismic models of various reservoir and basinal environments predicted that  $V_p/V_s$  is lower across intervals containing porous reservoir rocks than for the same intervals containing basinal anhydrite or tight limestone. The contrast in  $V_p/V_s$  is proportionately greater for a smaller interval.
6. The inclusion of intrabed multiples and in the *P-P* offset synthetic seismograms resulted in a better tie to the data. Short-path multiple interference delays the Nisku event on the *P*-

*P* seismic data, but this delay is laterally consistent. Intrabed multiples have less effect on the Nisku arrival on the *P-S* data than on the *P-P* data.

7. The trend of  $V_p/V_s$  lows at oil well locations is consistent with the *P-S* synthetic seismogram matching analyses at the 16-19 and 12-20 wells, as well as the forward modelling study of various geologic environments. Hence,  $V_p/V_s$  analysis can be used to map the lateral extent of the porosity within the Nisku dolomitic buildup.

#### **4.2.2 Blackfoot Field**

1. A confident correlation between *P-P* and *P-S* seismic sections was obtained using *P-P* and *P-S* offset synthetic seismograms generated from dipole sonic logs.

2. *P-P* and *P-S* seismic cross-section models indicate that the incised valley fill can be defined on both the *P-P* and *P-S* seismic sections.  $V_p/V_s$  analysis of the models showed that the average interval  $V_p/V_s$  is lower at the sand channel (1.85) than at either a shale-plugged channel or the regional section (1.93).

3. Both the *P-P* and *P-S* sections show seismic character and amplitude changes which are consistent with the model. These were used to define the lateral extent of the incised valley fill from shotpoints 161 to 211.

4. The interval from the Viking to the Shunda shows a  $V_p/V_s$  low from shotpoints 167 to 191, which is interpreted to indicate a thick sandstone facies within the incised valley. Higher  $V_p/V_s$  on the northwest side of the incised valley fill are interpreted to correspond to an increase in shaliness.

5. Analysis of well log data from the 08-08 and 12-16 wells indicates that the  $V_p/V_s$  decrease in sandstone facies is due to an increase in  $V_s$  and somewhat constant  $V_p$ .



## References

- Andrichuk, J.M. and Wonfor, J.S., 1954, Late Devonian geologic history in Stettler area, Alberta, Canada: AAPG Bull., 38, 2500-2536.
- Anno, P.D., 1985, Exploration of the Hunton Group, Anadarko Basin, using shear waves: Presented at the 53rd Ann. Internat. Mtg., Soc. Expl. Geophys.
- Badgley, P.C., 1952, Detrital (Deville) Beds (Mannville Group) *in* Glass, D.J., Ed., Lexicon of Canadian Stratigraphy, Vol. 4, Western Canada, Including Eastern British Columbia, Alberta, Saskatchewan, and Southern Manitoba, CSPG, 1990.
- Bell, J.S., Price, P.R., and McLellan, P.J., 1994, In-situ stress in the Western Canadian Sedimentary Basin, *in* Geological Atlas of the Western Canadian Sedimentary Basin, Mossop, G.D. and Shetsen, I., (Comps.), Calgary, CSPG and Alberta Research Council, pp. 439-446.
- Castagna, J.P., Batzle, M.L., and Eastwood, R.L., 1985, Relationships between compressional-wave and shear-wave velocities in clastic silicate rocks: Geophysics, 50, 571-581.
- Coveney, J.W., 1960, Bantry Shale Member (Lower Mannville Formation), *in* Glass, D.J., Ed., Lexicon of Canadian Stratigraphy, Vol. 4, Western Canada, Including Eastern British Columbia, Alberta, Saskatchewan, and Southern Manitoba, CSPG, 1990.
- Dixon, R.J., Stoakes, F.A., and Campbell, C.V., 1991, Exploration for Nisku Formation isolate reefs of the Wood River area: a stratigraphic play-type in a structural world: Canadian Society of Petroleum Geologists Conference Program and Abstracts, p. 55.
- Domenico, S.N., 1984, Rock lithology and porosity determination from shear and compressional wave velocity: Geophysics, 49, 1188-1195.
- Eastwood, R.L. and Castagna, J.P., 1983, Basis for interpretation of  $V_p/V_s$  ratios in complex lithologies: Soc. Prof. Well Log Analysts 24th Annual Logging Symp.

- Eaton, D. W. S., Slotboom, R. T., Stewart, R. R., and Lawton, D. C., 1990, Depth-variant converted-wave stacking: Presented at the 60th Ann. Internat. Mtg., Soc. Expl. Geophys.
- Eberhart-Phillips, D., Han, D.H. and Zoback, M.D., 1989, Empirical relationships among seismic velocity, effective pressure, porosity, and clay content in sandstone: *Geophysics*, 54, 82-89.
- Ensley, R.A., 1984, Comparison of *P*- and *S*-wave seismic data: a new method for detecting gas reservoirs: *Geophysics*, 49, 1420-1431.
- Ensley, R.A., 1985, Evaluation of direct hydrocarbon indicators through comparison of compressional- and shear-wave seismic data: a case study of the Myram gas field, Alberta: *Geophysics*, 50, 37-48.
- Ferguson, R.J. and Stewart, R.R., 1996, Characterization of a sand channel reservoir using 2.0, 4.5 and 10 Hz 3-C seismic data: Blackfoot, Alberta: Presented at the 1996 Can. Soc. Expl. Geophys. Nat. Conv.
- Gallant, E.V., Stewart, R.R., Bertram, M.B., and Lawton, D.C., 1995, Acquisition of the Blackfoot broad-band seismic survey: CREWES Research Report 7, ch. 36.
- Garotta, R., 1987, Two-component acquisition as a routine procedure, in Danbom, S.H., and Domenico, S.N., Eds., *Shear-wave exploration: Soc. Expl. Geophys., Geophysical development series 1*, 122-136.
- Garotta, R., Marechal, P., and Megesan, M., 1985, Two-component acquisition as a routine procedure for recording *P*-waves and converted waves: *Journal of the Canadian Society of Exploration Geophysicists*, 21, 40-53.
- Geological Staff, Imperial Oil, 1950, Nisku Formation (Winterburn Group), in Glass, D.J., Ed., *Lexicon of Canadian Stratigraphy, Vol. 4, Western Canada, Including Eastern British Columbia, Alberta, Saskatchewan, and Southern Manitoba*, CSPG, 1990.

- Geological Staff, Imperial Oil, 1950, Ireton Formation (Woodbend Group), *in* Glass, D.J., Ed., *Lexicon of Canadian Stratigraphy, Vol. 4, Western Canada, Including Eastern British Columbia, Alberta, Saskatchewan, and Southern Manitoba*, CSPG, 1990.
- Georgi, D.T., Heavysege, R.G., Chen, S.T., and Eriksen, E.A., 1989, Application of shear and compressional transit-time data to cased hole carbonate reservoir evaluation: Presented at Can. Well Logging Soc. 12th Formation Evaluation Symp.
- Goldberg, D. and Gant, W.T., 1988, Shear-wave processing of sonic log waveforms in a limestone reservoir: *Geophysics*, 53, 668-676.
- Gorek, S.J., Stewart, R.R., and Harrison, M.P., 1995, Processing the Blackfoot broadband 3-C seismic data: *CREWES Research Report 7*, ch. 37.
- Gregory, A.R., 1977, Aspects of rock physics from laboratory and log data that are important to seismic interpretation, *in* *Seismic Stratigraphy - Applications to Hydrocarbon Exploration*: AAPG Memoir 26, 15-45.
- Han, D.H., Nur, A. and Morgan, D., 1986, Effects of porosity and clay content on wave velocities in sandstones: *Geophysics*, 51, 2093-2107.
- Harrison, M.P., 1992, Processing of P-SV surface seismic data: Anisotropy analysis, dip moveout, and migration: Ph.D. dissertation, Univ. of Calgary.
- Harrison, M. P., and Stewart, R. R., 1993, Poststack migration of P-SV seismic data: *Geophysics*, v 58, 1127-1135.
- King, M.S., Stauffer, M.R., Yang, H.J.P., and Hajnal, Z., 1988, Elastic-wave and related properties of clastic rocks from the Athabasca Basin, Western Canada: *Can. J. Expl. Geophys.*, 24, 110-116.
- Kithas, B.A., 1976, Lithology, gas detection, and rock properties from acoustic logging systems: Soc. Prof. Well Log Analysts 17th Annual Symp.

- Kohrs, B.M. and Norman, D.K., 1988, Stratigraphic Correlation Chart, *in* Hills, L.V. and Cederwall, D.A., Eds., The CSEG/CSPG Western Canadian Atlas of Hydrocarbon Pools, VIII.
- Kuster, G.T. and Toksöz, M.N., 1974, Velocity and attenuation of seismic waves in two-phase media: Part 1. Theoretical formulations: *Geophysics*, 39, 587-606.
- Lawton, D.C. and Howell, C.E., 1992, P-S and P-P synthetic stacks: Presented at the 62th Ann. Internat. Mtg., Soc. Expl. Geophys.
- Layer, D.B. and Members of Staff, Imperial Oil Ltd., 1949, Leduc oil field, Alberta, a Devonian coral reef discovery: *Bulletin of the American Association of Petroleum Geologists*, 33, 575-602.
- Leckie, D.A., Bhattacharya, J.P., Bloch, J., Gilboy, C.F, Norris, B., 1994, Cretaceous Colorado/Alberta Group of the Western Canada Sedimentary Basin. In: *Geological Atlas of the Western Canada Sedimentary Basin*. G.D. Mossop and I. Shetsen (Comps.). Calgary, Canadian Society of Petroleum Geologists and Alberta Research Council, p. 335-352.
- Margrave, G.F. and Foltinek, D.S., 1995, Synthetic *P-P* and *P-SV* cross sections: CREWES Research Report 1995, Ch 5.
- McCormack, M.D., Dunbar, J.A. and Sharp, W.W., 1984, A case study of stratigraphic interpretation using shear and compressional seismic data: *Geophysics*, 49, 509-520.
- McCormack, M.D., Dunbar, J.A. and Sharp, W.W., 1985, A stratigraphic interpretation of shear and compressional wave seismic data for the Pennsylvanian Morrow formation of southeastern New Mexico, *in* *Seismic Stratigraphy II: AAPG Memoir* 39, 225-239.
- Miller, S.L.M. and Stewart, R.R., 1990, Effects of lithology, porosity and shaliness on P- and S-wave velocities from sonic logs: *Can. J. Expl. Geophys.*, 26, 94-103.
- Miller, S.L.M., Harrison, M.P., Szata, K.J., and Stewart, R.R., 1993, Processing and preliminary interpretation of multicomponent seismic data from Lousana, Alberta: CREWES Research Report 5, ch. .

- Miller, S.L.M., Harrison, M.P., Lawton, D.C., Stewart, R.R., and Szata, K.J., 1994, Analysis of *P-P* and *P-S* seismic data from Lousana, Alberta: CREWES Research Report 6.
- Minear, J.W., 1982, Clay models and acoustic velocities: Soc. Petr. Eng. of AIME 57th Annual Tech. Conf. & Exhib.
- Nations, J.F., 1974, Lithology and porosity from acoustic shear and compressional wave transit time relationships: Presented at Soc. Prof. Well Log Analysts 15th Annual Symp.
- Pardus, Y.C., Conner, J., Schuler, N.R., and Tatham, R.H., 1990,  $V_p/V_s$  and lithology in carbonate rocks: A case study in the Scipio trend in southern Michigan: Presented at Presented at the 60th Ann. Internat. Mtg., Soc. Expl. Geophys.
- Pickett, G.R., 1963, Acoustic character logs and their applications in formation evaluation: J. Petr.Tech., June, 659-667.
- Rafavich, F., Kendall, C.H.St.C., and Todd, T.P., 1984, The relationship between acoustic properties and the petrographic character of carbonate rocks: Geophysics, 49, 1622-1636.
- Raymer, L.L., Hunt, E.R., and Gardner, J.S., 1980, An improved sonic transit time-to-porosity transform: Soc. Prof. Well Log Analysts 21st Annual Symp.
- Rennie, W., Leyland, W., and Skuce, A., 1989, Winterburn (Nisku) Reservoirs in Anderson, N.L., Hills, L.V., and Cederwall, D.A., Eds. The CSEG/CSPG Geophysical Atlas of Western Canadian Hydrocarbon Pools, 133-154.
- Robertson, J.D., 1987, Carbonate porosity from S/P traveltimes ratios: Geophysics, 52, 1346-1354.
- Schlumberger, 1989, Log Interpretation Principles/Applications: Schlumberger Educational Services.
- Slotboom, R.T., 1990, Converted wave (*P-Sv*) moveout estimation: 60th Annual Internat. Mtg. Soc. Expl. Geophys., Expanded Abstracts, 90, 1104-1106.

- Stoakes, F.A., 1979, Sea level control of carbonate-shale deposition during progradational basin-filling: the Upper Devonian Duvernay and Ireton Formations of Alberta, Canada: Ph.D. dissertation, Univ. of Calgary.
- Stoakes, F.A., 1992, Winterburn megasequence *in* Wendte, J., Stoakes, F.A., Campbell, C.V., Devonian-Early Mississippian carbonates of the Western Canada sedimentary basin; a sequence stratigraphic framework: SEPM short course No. 28, 207-224.
- Switzer, S.B., Holland, W.G., Christie, D.S., Graf, G.C., Hedinger, A.S., McAuley, R.J., Wierzbicki, R.A., and Packard, J.J., 1994, Devonian Woodbend-Winterburn Strata of the Western Canadian Sedimentary Basin, in Geological Atlas of the Western Canadian Sedimentary Basin, Mossop, G.D. and Shetsen, I., Comps., Calgary, CSPG and Alberta Research Council, pp. 165-202.
- Tatham, R.H., 1982, Vp/Vs and lithology: Geophysics, 47, 336-344.
- Tatham, R.H. and McCormack, M.D., 1991, Multicomponent Seismology in Petroleum Exploration: Soc. Expl. Geophys., Investigations in geophysics no. 6.
- Toksöz, M.N., Cheng, C.H., and Timur, A., 1976, Velocities of seismic waves in porous rocks: Geophysics, 41, 621-645.
- Tosaya, C. and Nur, A., 1982, Effects of diagenesis and clays on compressional velocities in rocks: Geophys. Res. Lett., 84, 3532-3536.
- Vernik, L. and Nur, A., 1991, Lithology prediction in clastic sedimentary rocks using seismic velocities: Presented at the 1991 SEG Summer Research Workshop, St. Louis, Missouri.
- Wilkens, R., Simmons, G., and Caruso, L., 1984, The ratio Vp/Vs as a discriminant of composition for siliceous limestones: Geophysics, 49, 1850-1860.
- Wood, J.M., and Hopkins, J.C., 1992, Traps associated with paleovalleys and interfluves in an unconformity bounded sequence: Lower Cretaceous Glauconitic Member, Southern Alberta, Canada: The American Association of Petroleum Geologists Bulletin, 76(6), 904-926.

Wyllie, M.R.J., Gregory, A.R., and Gardner, L.W., 1956, Elastic wave velocities in heterogeneous and porous media: *Geophysics*, 21, 41-70.